

**CONTROL OF TRAPPED-ION MOTION FOR  
MOLECULAR SPECTROSCOPY AND QUANTUM  
INFORMATION PROCESSING**

**DING SHIQIAN**  
(B.Sc., Lanzhou University, 2010)

**A THESIS SUBMITTED FOR  
THE DEGREE OF DOCTOR OF PHILOSOPHY  
CENTRE FOR QUANTUM TECHNOLOGIES  
NATIONAL UNIVERSITY OF SINGAPORE**

**2016**

## DECLARATION

I hereby declare that this thesis is my original work and it has been written by me in its entirety. I have duly acknowledged all the sources of information which have been used in the thesis.

This thesis has also not been submitted for any degree in any university previously.

---

Shiqian Ding

January, 2016

To my parents.

# Contents

Contents	iii
List of Tables	viii
List of Figures	ix
<b>1 Introduction</b>	<b>1</b>
1.1 Molecular ions . . . . .	2
1.2 Microwave control of trapped-ion motion . . . . .	5
1.3 Nonlinear interaction between motional modes . . . . .	6
1.4 Outline of the thesis . . . . .	7
<b>2 Control of trapped-ion motion</b>	<b>9</b>
2.1 Introduction to the ion trapping . . . . .	9
2.1.1 Theory . . . . .	9
2.1.2 Experimental apparatus . . . . .	14
2.2 Loading of $\text{Yb}^+$ . . . . .	15
2.2.1 Isotope-selective loading with Yb oven . . . . .	17
2.2.2 Loading with neutral Yb from laser ablation . . . . .	17
2.2.3 Loading with $\text{Yb}^+$ ions from laser ablation . . . . .	21

2.3	Doppler cooling of the ion . . . . .	22
2.3.1	Theory . . . . .	22
2.3.2	Experimental Doppler cooling of $^{171}\text{Yb}^+$ . . . . .	25
2.3.3	Compensation of micromotion . . . . .	29
2.4	Cooling to the motional ground state . . . . .	30
2.4.1	Theory . . . . .	30
2.4.2	Experimental realization of ground state cooling . . . . .	39
<b>3</b>	<b>Quantum logic for the control and manipulation of molecular ions using a frequency comb</b>	<b>45</b>
3.1	Model . . . . .	46
3.2	Possible implementation . . . . .	51
<b>4</b>	<b>Zeeman-splitting-assisted quantum-logic spectroscopy of trapped ions</b>	<b>55</b>
4.1	Model . . . . .	56
4.2	Proof-of-principle experiment . . . . .	59
4.3	Sideband cooling of $\text{SiO}^+$ to the motional ground state . . . . .	64
4.3.1	Mass spectroscopy of the molecular ion . . . . .	65
4.3.2	Loading and sympathetic cooling of the $\text{SiO}^+$ ions . . . . .	71
4.3.3	Cooling of a single $\text{SiO}^+$ ion to motional ground state . . . . .	76
4.4	Conclusion and outlook . . . . .	77
<b>5</b>	<b>Microwave control of trapped-ion motion assisted by a running optical lattice</b>	<b>80</b>
5.1	Experimental setup . . . . .	82
5.2	Measurement of the Stark shift . . . . .	83

5.3	Theory . . . . .	86
5.4	Experimental characterization of the Hamiltonian . . . . .	88
5.5	Sideband cooling . . . . .	91
5.6	Conclusion and outlook . . . . .	97
<b>6</b>	<b>Phonon down-conversion in a linear ion trap</b>	<b>98</b>
6.1	Introduction . . . . .	98
6.2	Theory . . . . .	99
6.3	Experimental setup . . . . .	102
6.4	Phonon evolution at resonance . . . . .	108
6.4.1	Phonon up and down conversion . . . . .	109
6.5	Adiabatic sweep . . . . .	112
6.5.1	Adiabatic state evolution . . . . .	112
6.5.2	Cooling of optically inaccessible mode (OIM) . . . . .	116
6.5.3	Wigner function measurement . . . . .	122
6.6	Conclusion and outlook . . . . .	129
	<b>Bibliography</b>	<b>130</b>

# Abstract

Control and manipulation of trapped ion motion are basic building blocks for quantum information processing and precision measurements with trapped ions. In this thesis, I present several techniques aimed at the nondestructive state detection of molecular ions and quantum information processing.

First of all, I present a proposal to prepare, detect and manipulate the state of a molecular ion. In our proposed quantum logic scheme, the internal states of molecular ions are coupled to the internal states of a co-trapped atomic ion through their common modes of motion. I describe the experimental validation of this scheme in a proof-of-principle experiment with two different isotopes of Yb. I also present our experimental progress towards implementation of this scheme with molecular ions, and in particular sympathetic cooling of  $\text{SiO}^+$  molecular ion to the ground state of motion.

I also describe our experiment to control the motion of a trapped atomic ion using microwave radiation assisted by a running optical lattice. The spin-motional coupling is exploited to demonstrate sideband cooling of a  $^{171}\text{Yb}^+$  ion to the ground state of motion. This method can be easily applied to the molecular ions due to strong microwave transitions between rotational states of the molecules.

Finally, I discuss the coupling between two normal modes of a two-ion crystal that is induced by the intrinsic nonlinearity of the Coulomb interaction. This

## ABSTRACT

---

process is formally analogous to the process of the optical down-conversion. It is exploited to demonstrate phonon down-conversion (up-conversion) at the single quanta level. When combined with nearly deterministic phonon preparation and readout available in the ion trap, this coupling allows us to directly measure the parity of the motional state of the ions and reconstruct the Wigner function of the ions motion.

# List of Tables

6.1	Coherence times of the radial phonons. . . . .	108
-----	--	-----

# List of Figures

2.1	Trap setup. . . . .	16
2.2	Back reflection from the resonator during one off-on cycle. . . . .	19
2.3	Energy diagram relevant to the Doppler cooling of $^{171}\text{Yb}^+$ . . . . .	26
2.4	Schemes for state initialization and detection. . . . .	27
2.5	Single-photon transition and Raman transition. . . . .	31
2.6	Raman coupling with a picosecond mode-locked pulsed laser. . . . .	40
2.7	Raman coupling between the clock states of $^{171}\text{Yb}^+$ . . . . .	42
3.1	The proposed experimental setup. . . . .	46
3.2	Cooling of molecular rotational states. . . . .	49
3.3	Optical pumping scheme for $\text{SiO}^+$ molecule. . . . .	52
4.1	Schematic of Zeeman-splitting quantum logic spectroscopy. . . . .	56
4.2	Zeeman-splitting quantum logic spectroscopy. . . . .	61
4.3	Internal state evolution after the quantum logic pulses. . . . .	62
4.4	Optical pumping of $^{174}\text{Yb}^+$ into the $^2D_{3/2}$ state. . . . .	63
4.5	Two ions with different masses. . . . .	66
4.6	Calculations with $^{171}\text{Yb}^+$ - $\text{SiO}^+$ crystal. . . . .	73
4.7	Sideband cooling of a single $\text{SiO}^+$ . . . . .	78

## LIST OF FIGURES

---

5.1	Schematic of the experimental setup. . . . .	81
5.2	Microwave frequency scans with a running optical lattice. . . . .	84
5.3	Bessel function of the first kind. . . . .	86
5.4	Resolved motional sidebands. . . . .	89
5.5	Rabi frequencies vs microwave detuning. . . . .	92
5.6	R1 and B1 sidebands before and after sideband cooling. . . . .	93
5.7	Internal-state evolution before and after sideband cooling. . . . .	94
5.8	R2 and B2 sidebands before and after sideband cooling. . . . .	95
5.9	Evolution (B2) before and after sideband cooling. . . . .	96
6.1	Experimental setup. . . . .	103
6.2	Schematic of the stabilization of the radial trapping frequencies. . . . .	105
6.3	The coherence times of the radial phonons. . . . .	106
6.4	The energy diagram without considering the coupling term. . . . .	109
6.5	Phonon state evolution. . . . .	111
6.6	Avoided crossing (theory) for different manifolds of states. . . . .	113
6.7	Avoided crossing (experiment) for the 2nd manifolds of states. . . . .	114
6.8	Adiabatic evolution of phonon states. . . . .	115
6.9	Swap of motional excitation. . . . .	119
6.10	Cooling of optically inaccessible mode (radial). . . . .	122
6.11	Cooling of optically inaccessible mode (axial). . . . .	124
6.12	Wigner functions of the coherent states. . . . .	126
6.13	Wigner functions of the cat states. . . . .	127
6.14	Wigner functions of the Fock states. . . . .	127

# Chapter 1

## Introduction

More than 60 years ago, Schrödinger described the progress in experimental physics at that time in the following way [129]: “This is the obvious way of registering the fact, that we never experiment with just one electron or atom or (small) molecule. In thought-experiments we sometimes assume that we do; this invariably entails ridiculous consequence. . . it is fair to state that we are not experimenting with single particles, any more than we can raise Ichthyosauria in the zoo.”

Sixty years later, progress made in experimental physics, e.g. the invention of the Paul trap for charged particles [112] and laser cooling of atoms [103; 154], allows the measuring and manipulation of individual quantum systems [44; 152]. These technological advances paved the way for rapid progress in traditional areas of research like precision measurements, and new research fields such as quantum information processing. Experimental groups around the world can now demonstrate simple quantum algorithms by controlling simple quantum systems to a high precision. One example of such a well-controlled physical system is the trapped ion, which is employed to demonstrate one of the most precise atomic

clocks [18].

At the basis of these applications of trapped ions lies the capability to control the trapped-ion motion in the quantum mechanical regime and couple the motional states coherently to the internal states of the ions. It enables the cooling of the ions to the quantum mechanical ground state of motion, and allows the preparation and detection of single motional quanta, or phonon, and engineering of complicated nonclassical motional states of ions such as Schrödinger cat states [73].

The control of motional states and isolation from environment achieved in experiments on atomic ions can be extended to more complicated quantum systems such as single molecular ions. In this thesis, I present a series of experiments and theoretical proposals that are aimed at developing methods to prepare, detect and manipulate the quantum state of the molecular ions.

## 1.1 Molecular ions

Due to their rich level structure, molecules are well-suited for probing the time variation of fundamental constants [16; 17; 27; 55; 133; 161], precisely measuring parity violation [26; 40] and time-reversal non-invariance effects [56; 139], studying quantum mechanical aspects of chemical reactions [150], and implementing scalable quantum information processing architectures [1]. Molecular ions are particularly attractive for these applications. Due to their near-perfect isolation from the environment they have long storage and coherence times which is required to achieve high measurement precision and reduce systematic errors.

However, the control of molecular quantum states still remains a challenge. Ideally, state detection of the ion proceeds in a nondestructive manner such that

the experiment may be repeated multiple times to achieve the required precision. One such example is state-dependent fluorescence, where the ion appears “bright” by scattering light only when it is in a given state; otherwise, the ion is “dark” [12; 24]. For fluorescence to be a sensitive state detection method, the ion species must have a fast cycling transition, which is hard to find in case of molecular ions. This limits the applicability of this standard fluorescence detection method in molecular spectroscopy. Other detection methods such as resonance-enhanced multiphoton dissociation [67; 142] are destructive in nature.

To circumvent the constraint of state detection, a method of quantum logic spectroscopy (QLS) [126] for molecular ions was proposed [125]. QLS was initially developed in a system of atomic ions by utilizing the coherent coupling between the internal states of ions and their motions. The spectroscopy ion (molecular ion) is co-trapped with a logic ion (atomic ion). Only the latter needs to possess a closed cycling transition. The internal state of the spectroscopy ion can then be transferred onto the shared motion of the two-ion system, which is in turn mapped onto the internal state of the logic ion. In the initial demonstration of QLS [126] for atomic ions, the ions were initially prepared in the ground state, and the excitation of ion crystal motion was achieved by driving motional sidebands of a narrow spectroscopic transition between long-lived states. Several variations of QLS have since been demonstrated. For instance, the trapped ions’ motion can be driven by a laser resonant with the spectroscopy transition. The resulting photon recoil of the ions can be detected by looking at Doppler recooling times [19], Doppler velocimetry [85] or phonon excitations [147]. These methods require the spectroscopy ion to have a partially closed cycling transition, which is not present in many molecular ions. Instead of multi-photon scattering, single-photon scattering can be employed to map the single-photon recoil of the spectroscopy

ion onto a geometric phase [49].

An additional complication arises from the large number of energy levels available in molecular ions, which complicates the preparation of molecular ions in a single quantum state. While the translational motion of molecular ions can be sympathetically cooled to milikelvin temperatures, the rotational and vibrational degrees of freedom will still be in equilibrium with the environment. Since typical spacings between the rotational levels of a molecule are on the order of 10-100 GHz which is much lower than the thermal energy  $kT/h \simeq 6$  THz at room temperature, several molecular states are populated in equilibrium with the environment. Due to the interaction of a molecule with black body radiation, internal degrees of freedom reach equilibrium on the timescale of the order of minutes [127; 137; 144].

Several methods of preparing molecular ions in a single quantum state have recently been demonstrated, including optical pumping assisted by black body radiation [127; 137], sympathetic cooling of translational degrees of freedom for molecular ions prepared in a particular rovibrational state [141], sympathetic cooling of molecular ions in a cloud of ultracold neutral atoms [54; 116], and optical pumping using broadband light [82; 83; 104; 143]. Other promising techniques such as cavity cooling [79; 101] have been proposed and is currently under active experimental investigation.

Some proposals [70; 102; 125; 134; 144; 145] also consider QLS as a way of preparing molecular states. However, the coupling between internal and motional states is typically [70; 125; 144; 145] achieved using pulses produced by continuous-wave (cw) lasers or microwave source [134]. These approaches may be difficult to implement experimentally given the number of molecular states that one needs to address.

In this thesis, I propose several possible approaches to detect and manipulate

of the internal states of the molecular ion through control of the collective motion of the molecular ion and the co-trapped atomic ion confined in the same trap [32; 88]. I also present a proof-of-principle experiment with different species of atomic ions that validates one of the proposed schemes [88].

## 1.2 Microwave control of trapped-ion motion

We see from the previous analysis that the states of the collective motion may assist the state preparation and detection of the molecular ions. Moreover, the trapped ion in the quantum regime is essentially a quantum harmonic oscillator and such a simple quantum mechanical system is an interesting subject of research on its own [73]. Being coupled to the internal states, the motional states of the ions have been engineered to show diverse quantum phenomena [87; 95] similar to the ones observed in quantum optics.

Traditionally, coupling between internal and motional states is achieved by illuminating the ions with laser light, either continuous wave [73] or from a mode-locked pulse laser [47]. The lasers in this case perform two functions. They resonantly couple quantum states of the ions, for example, via two-photon stimulated Raman transitions. They also produce state-dependent potentials that change on a scale comparable to the laser wavelength, giving rise to a spin-dependent force. As a result, a change of the internal state of an ion is accompanied by a change of its motional state.

Alternatively to optical lasers, microwave radiation can be used to drive transitions between hyperfine states and shift the ions' energy levels. However, due to its long wavelength, the microwave state-dependent potential changes over a significantly larger distance and the spin-dependent force is therefore usually weak.

The gradient of the microwave field can however be significantly enhanced in the near-field regime, where microwaves are applied directly to the electrodes of a microfabricated ion trap, leading to spin-motion coupling [110; 111].

The shift of the energy levels and the transition between them can also arise from two separate physical processes, and these combinations already provide benefits for several applications. For example, a state-dependent potential can be derived from the gradient of a static magnetic field, whereas transitions can be driven by on-resonant microwave radiation, offering a new approach for quantum information processing with trapped ions [62; 64; 96]. Spin-motion coupling was also demonstrated for neutral atoms trapped in a spin-dependent optical lattice potential and irradiated by a spatially uniform microwave field, leading to a simple scheme for the sideband cooling of atoms to the ground state of motion [38; 81]. However, in the case of trapped ions, interferometric stability between the optical lattice and the ion position is required. Achieving this is a technically challenging task that usually requires active stabilization of the beam path [58] or integrating the ion trap with an optical cavity [36; 42; 63; 86].

In this thesis, I describe a method to control the motion of the ions using microwave radiation, assisted by a running optical lattice [31]. The latter removes the requirement for the interferometric stability. This method can be easily applied to the molecular ions due to strong microwave transitions between rotational states of the molecules.

### 1.3 Nonlinear interaction between motional modes

In the previous description, the motions of the trapped ions are always represented by a set of independent normal modes because the trapping potential the

ions see in a Paul trap is harmonic to a high degree. However, the Coulomb potential between ions may induce some mode coupling. The linear coupling of this kind was previously demonstrated in the quantum regime [13; 43] when the ions were trapped in independent potential wells. Besides the lowest-order linear coupling, the Coulomb interaction between ions also provides anharmonicity [93; 106], which in turn leads, for example, to Kerr-type nonlinear couplings between motional modes and shifts of normal mode frequencies [119]. Such nonlinear interaction between normal modes has been demonstrated between two internal degrees of freedom of a superconducting artificial atom [71].

A system of harmonic oscillators coupled via nonlinear interactions that we can simulate with trapped ions is a fundamental model in solid state physics [2], electronics [89] and quantum optics [92]. It helps to explain a diverse range of physical phenomena, from the thermal conductivity of solids [2], to the generation of entangled photon pairs [68] and squeezed states of light [158]. This kind of nonlinear coupling in trapped ions can be applied to quantum information processing protocols [69], preparation of nonclassical states [158], and studies of quantum thermodynamics [22; 80].

## 1.4 Outline of the thesis

This thesis is organized as follows.

Chapter 2 gives an overview on how the ions are trapped and cooled to the ground state of motion. It starts with the basic physical model necessary to describe the linear Paul trap and it also presents our experimental apparatus. The methods of loading the ions are detailed, along with the theoretical treatment and experimental realization of Doppler cooling of ions ( $^{171}\text{Yb}^+$ ). It ends with

explanation of motional ground state cooling.

Chapter 3 describes a proposal of the experimental schemes to prepare, manipulate and detect the internal states of a trapped molecular ion based on the quantum logic techniques using a frequency comb.

Chapter 4 begins with the proposal for the state detection of molecular ions with a Zeeman-splitting-assisted quantum logic scheme. We experimentally demonstrate this protocol using a proof-of-principle experiment with atomic ions. It is followed by our progress towards the implementation of this scheme with molecular ions ( $\text{SiO}^+$ ).

Chapter 5 presents the experimental demonstration of the coupling between the motional states and internal states of a single ion with microwave radiation when the ion is placed in a running spin-dependent optical lattice.

Chapter 6 discusses a nonlinear coupling between different modes of a two-ion crystal induced by the Coulomb interaction. We experimentally demonstrate phonon down-conversion (up-conversion) at the single quanta level. This coupling is exploited to directly measure the parity of the quantum (motional) states and their Wigner functions.

# Chapter 2

## Control of trapped-ion motion

### 2.1 Introduction to the ion trapping

#### 2.1.1 Theory

It is not possible to trap an ion in free space by a static electric field. When we say “trap”, we mean that a small displacement in any direction from the equilibrium position will generate a restoring force that returns the ion back to the equilibrium. It requires all the electric field vectors in the vicinity of the ion to point towards the ion. The latter requirement violates Gauss’s law for the electric field. Indeed, Gauss’s law requires the divergence of electric field and the electric field flux through a closed surface to be zero. It suggests that the electric field potential can not have any local minima, only saddle points, and the ion is always in an unstable equilibrium at least for one direction. The situation is different if we can vary the electric field in time. If the unstable direction is changed dynamically, the motion of the ion becomes stable under some conditions. This forms the basis for the Paul trap, which is commonly used for confining charged

particles.

The standard radio frequency (rf) linear Paul trap [112] consists of four rods, two diagonal ones of which are connected to oscillating rf voltages and the other two connected to constant voltages, and two needles as endcaps that carry DC voltages (see Fig. 2.1). We assume a hyperbolic electrode configuration for simplicity. The potential in the trap region due to the voltages applied to the rods is [60; 151]

$$\phi_{rod} = \frac{U + \tilde{U} \cos(\Omega t)}{2} \left( \frac{x^2 - y^2}{R^2} + 1 \right), \quad (2.1)$$

where  $U$ ,  $\tilde{U}$  and  $\Omega$  are the rf voltage offset, amplitude and frequency, respectively. Without any loss of generality, we set the initial phase to be 0.  $R$  is the distance between the center of the trap and the rods.

A charged particle with charge  $e$  experiences the force

$$F = e(-\nabla\phi_{rod}) = -e(U + \tilde{U} \cos(\Omega t)) \frac{x\hat{x} - y\hat{y}}{R^2}, \quad (2.2)$$

and obeys the equations of motion

$$\begin{cases} \ddot{x} + \frac{e}{mR^2} (U + \tilde{U} \cos(\Omega t)) x = 0 \\ \ddot{y} - \frac{e}{mR^2} (U + \tilde{U} \cos(\Omega t)) y = 0, \end{cases} \quad (2.3)$$

where  $m$  is the mass of the particle. Intuitively, one may expect that the oscillating term will cancel out after averaging over time. This is true for a homogeneous electric field. However, it is not true if the field is inhomogeneous. The particle sees an effective potential, or pseudopotential, that results in a small average force that is always pointing in the direction of lower average field [23].

The motion along  $x$  and  $y$  directions is decoupled according to Eqn. 2.3.

Introducing the dimensionless parameters:

$$a_x = \frac{4eU}{mR^2\Omega^2} , \quad (2.4)$$

$$q_x = \frac{2e\tilde{U}}{mR^2\Omega^2} , \quad (2.5)$$

$$\tau = \frac{\Omega t}{2} , \quad (2.6)$$

we can write the equation of motion in the  $x$  direction as

$$\frac{d^2x}{d\tau^2} + (a_x + 2q_x \cos(2\tau)) x = 0 , \quad (2.7)$$

and similarly for the  $y$  direction. This kind of differential equation is called the Mathieu equation. It has stable solutions for certain sets of parameters. The approximate solution for values of  $a$ ,  $q \ll 1$  is [73]

$$x = C_x \cos\left(\frac{\beta_x \Omega}{2} t\right) \left(1 - \frac{q_x}{2} \cos(\Omega t)\right) , \quad (2.8)$$

where  $C_x$  is a constant used to satisfy initial conditions, and

$$\beta_x = \sqrt{a_x + q_x^2/2} . \quad (2.9)$$

The oscillation due to the term  $\cos(\beta_x \Omega t/2)$  is called the secular motion and the corresponding oscillation frequency

$$\omega_x = \frac{\beta_x \Omega}{2} \quad (2.10)$$

is called the secular frequency. Superimposed on the secular motion is a fast modulation at the driving frequency  $\Omega$ , which is called the micromotion. It can

be large if the ion is displaced from the nodal line by some stray electric field, since the driving field is proportional to the displacement from the nodal line, as shown by Eqn. 2.2<sup>1</sup>. Nevertheless, the micromotion can be compensated if some external DC electric field pushes the ion back to the zero point of the rf potential.

Similiarly we can solve the equation of motion along  $y$  direction by setting

$$a_y = -a_x , \quad (2.11)$$

$$q_y = -q_x . \quad (2.12)$$

By defining

$$\begin{aligned} \omega_p &\doteq \frac{q_x \Omega}{2\sqrt{2}} \\ &= \frac{e\tilde{U}}{\sqrt{2}mR^2\Omega} , \end{aligned} \quad (2.13)$$

we obtain the following equation for the secular frequency in  $x$  ( $y$ ) direction,

$$\omega_{x(y)} = \sqrt{\omega_p^2 + a_{x(y)}\left(\frac{\Omega}{2}\right)^2} . \quad (2.14)$$

While the confinement along the  $x$  and  $y$  directions is provided by the rf voltage, the DC voltage  $U_0$  ( $U_0 > 0$  for positive ions) applied to the endcaps provides the confinement along  $z$  direction. Near the trap center, the potential due to this DC voltage can be approximated by [4]

$$\phi_{ndl} = \frac{\epsilon U_0 (2z^2 - x^2 - y^2)}{2d^2} , \quad (2.15)$$

---

<sup>1</sup>For a full mathematical treatment of micromotion, see [6; 28].

where  $U_0$  is the voltage applied to the endcaps,  $\epsilon$  is the geometric factor and  $2d$  is the distance between two endcaps.

The equation of motion along  $z$  axis is simply

$$m\ddot{z} = -e \frac{d\phi_{ndl}}{dz} = -\frac{2e\epsilon U_0}{d^2} z . \quad (2.16)$$

It describes a harmonic oscillator with the frequency of

$$\omega_z = \sqrt{\frac{2e\epsilon U_0}{md^2}} . \quad (2.17)$$

The potential of Eqn. 2.15 also weakens the confinement along radial direction. It does not influence the rf part in front of  $x^2$  ( $y^2$ ) in Eqn. 2.1, or  $q_{x(y)}$  in Eqn. 2.7 (Eqn. 2.12). However, it changes the DC part to

$$\phi_{DC} = \frac{(U - R^2\epsilon U_0/d^2)x^2 - (U + R^2\epsilon U_0/d^2)y^2}{2R^2} . \quad (2.18)$$

Similarly, we write down the modified expressions for parameters  $a_x$  and  $a_y$  as follows:

$$a_x = \frac{4e\epsilon U_0}{md^2\Omega^2}(\alpha - 1) , \quad (2.19)$$

$$a_y = -\frac{4e\epsilon U_0}{md^2\Omega^2}(\alpha + 1) , \quad (2.20)$$

where the parameter

$$\alpha = Ud^2/(R^2\epsilon U_0) \quad (2.21)$$

is used to characterize the radial asymmetry. Eqn. 2.14 is then transformed into

$$\omega_x = \sqrt{\omega_p^2 + (\alpha - 1)\omega_z^2/2}, \quad (2.22)$$

$$\omega_y = \sqrt{\omega_p^2 - (\alpha + 1)\omega_z^2/2}, \quad (2.23)$$

from which we can derive  $\alpha = (\omega_x^2 - \omega_y^2)/\omega_z^2$ . We emphasize that  $\alpha$  is independent of the ion's mass according to Eqn. 2.21.

### 2.1.2 Experimental apparatus

Our trap configuration and dimension are shown in Fig. 2.1. The rods and needles are made of tungsten rods with a diameter of 0.5 mm. They are installed in two ceramic holders. The distance between neighboring rods is approximately 0.9 mm and the distance between the needles is 2.0 mm. These two ceramic holders are then held in place by a stainless steel holder which allows for convenient optical access (see Fig. 2.1). The whole setup is stationed in a stainless steel octagon which is maintained at pressure of around  $2 \times 10^{-11}$  Torr. The rf or DC voltages are applied to the rods or needles via two vacuum feedthroughs. One of the feedthroughs also carries the current for heating the Yb ovens (see below).

The voltage applied to the needles can be as high as 400 volts. It is generated with a homemade circuit based on a commercial high voltage power supply (Matsusada Precision, TM-0.8P). To create a harmonic pseudopotential with the desired frequency and trap depth, a high rf voltage (hundreds of volts) is desirable. This voltage is generated by a homemade helical resonator [11; 91], which is designed to be similar to that in Ref. [48; 109]. The resonant frequency in our case is 30 MHz and we obtain a loaded quality factor around 150. We obtain a few watts of rf power by amplifying the signal from a commercial function genera-

tor (Agilent Technologies, 33250A) with a commercial rf amplifier (Mini Circuits, ZHL-5W-1). The signal is then coupled to the resonator inductively. The back reflection from the resonator, which is extracted by a directional coupler, is sent to a dedicated oscilloscope for continuous monitoring. The radial trapping frequency of our trap is about 1 MHz, and axial trapping frequency around 0.8 MHz (for  $^{171}\text{Yb}^+$ ), corresponding to  $q \sim 0.1$  (Eqn. 2.13) and  $a \sim 0.001$  (Eqn. 2.19) for a  $\text{Yb}^+$  ion and  $q \sim 0.4$  and  $a \sim 0.004$  for a  $\text{SiO}^+$  ion. The resonator also allows for the application of independent bias voltages to the rods. For more details of the resonator, see Ref. [48; 109].

Six small viewports with an aperture of around 2 cm are attached to the sides of the octagon and two big viewports with an aperture of around 7 cm are mounted on the top and bottom of the octagon. They are anti-reflective coated in the range of 350 nm - 400 nm and allow for flexible optical access for the ionization beams, cooling beams, repumper beams as well as the Raman beams as shown later. The fluorescence collected by a triplet lens with  $\text{NA} \sim 0.25$ , positioned above the upper big viewport, is directed by motorized flip mirror to either a photomultiplier tube (PMT) for photon-counting or a camera (Princeton Instruments, ProEM 512) for ion imaging.

## 2.2 Loading of $\text{Yb}^+$

We load the  $\text{Yb}^+$  ions by three methods, which all rely on ionizing neutral Yb atoms.

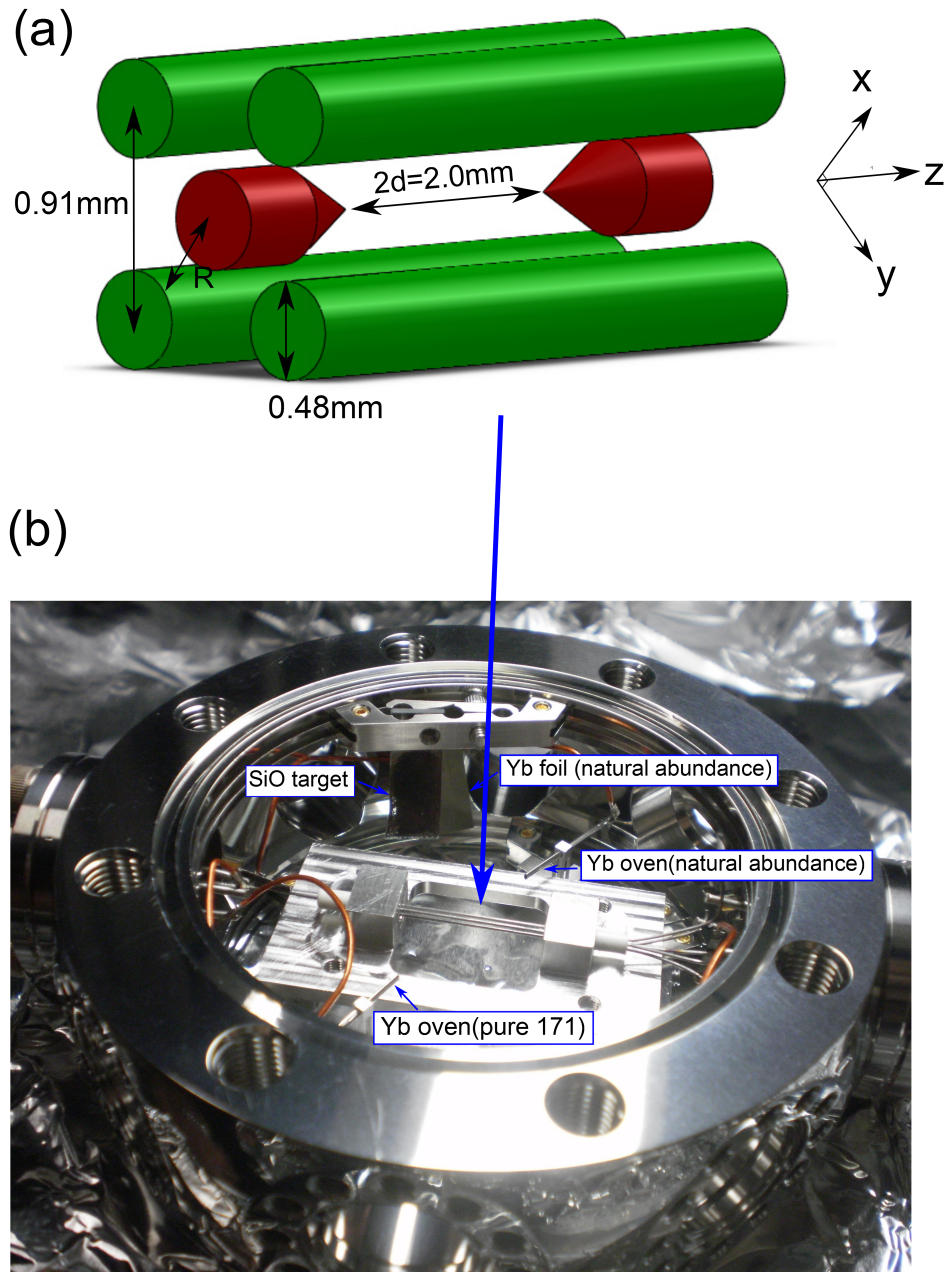


Figure 2.1: Trap setup. (a) Standard rf linear Paul trap consisting of four rods offering radial confinement and two endcaps offering axial confinement. (b) The trap is installed in a stainless steel octagon which is maintained at  $2 \times 10^{-11}$  Torr. The Yb ovens (foil) and SiO target are also shown.

### 2.2.1 Isotope-selective loading with Yb oven

A beam of neutral Yb atoms with natural isotope abundance is produced by resistively heating a stainless steel tube filled with Yb metal (called the Yb oven, see Fig. 2.1(b)). The oven is aligned such that the Yb beam goes through the trap center, where the atoms are photoionized with a resonance-enhanced two-photon process [3; 66; 108]. A continuous-wave (cw) external-cavity diode laser (Toptica DL 100 pro) with wavelength of 399.91 nm and power of 100  $\mu$ W is focused in the trap center with a diameter of 30  $\mu$ m. It is aligned to be approximately perpendicular to the Yb beam to minimize the Doppler effect such that it can isotope-selectively drive the  $6s_2 \ ^1S_0 \longrightarrow 6s6p \ ^1P_1$  transition in neutral Yb. A second laser with a wavelength of 369 nm, power of 5 mW and a diameter of 30  $\mu$ m in the trap center is aligned counterpropagating to the 399.91 nm beam. This laser can photoionize the neutral Yb from  $^1P_1$  state. By running the oven at low atomic beam flux and inspecting the fluorescence from the ion induced by the cooling laser (see following section) with the PMT or camera, we can achieve isotope-selective and nearly ion-number-deterministic loading. In addition, we also have another oven which contains isotopically enriched  $^{171}\text{Yb}$  since we normally need to trap  $^{171}\text{Yb}^+$ .

### 2.2.2 Loading with neutral Yb from laser ablation

In addition to an Yb oven, the neutral Yb may also be produced via laser ablation. A piece of Yb foil (5 mm $\times$ 15 mm, GoodFellow, YB000200/7) is mounted about 5 cm away from the trap center and faces towards the trap, as shown in Fig. 2.1. A Q-switched pulsed Nd:YAG laser (Continuum, Minilite II) can generate pulses with a pulse duration of 10 ns or so and pulse energy ranging from around 1  $\mu$ J to

8 mJ at wavelength of 355 nm. It is then focused on the Yb foil inside the vacuum chamber. The diameter of the focused ablation laser spot is around 50  $\mu\text{m}$ . The high laser intensity can create a local high temperature in a very short time such that the metal vaporizes. It causes a rapid ejection of a plume containing neutral atoms, clusters, ions and electrons [46; 75; 162]. The neutral atoms, in our case Yb, are then ionized in the trap region [50]. The ion number can be extracted from the laser fluorescence during the Doppler cooling (see following section).

We demonstrated two ways to ionize the neutral Yb from the laser ablation source. One is the same as what is used in loading the ion with Yb oven, i.e. two-photon ionization with 399.91 nm and 369 nm lasers. The other one is ionization with only 399.91 nm laser beam. One possible explanation for the latter to happen is that part of Yb atoms is in some metastable excited state after ablation, from which it can be ionized by the 399.91 nm laser. We note that ionization with both beams appears more efficient than ionization with only the 399.91 nm beam by a factor of at least ten, as indicated by the ion number loaded into the trap. This is consistent with what is reported in Ref. [3].

The number of the ions loaded into the trap can be roughly controlled by the ablation pulse energy. Loading of single  $^{174}\text{Yb}^+$  was demonstrated at a pulse energy around 2  $\mu\text{J}$ <sup>1</sup>. In our current setup, isotope-selective loading is not achieved since the foil we use contains Yb metal with natural isotope abundance and the

---

<sup>1</sup>Such low energy, which is produced when the pulsed laser is run at low energy mode (with reduced energy of pump flash lamp), is smaller than the minimum pulse energy our photodetector (Newport, 818E-03-12-L) can resolve (5  $\mu\text{J}$ ). The reported number here is an extrapolation from the established relationship between pulse energy with ( $E_L$ ) and without ( $E_H$ ) the filter (the latter one can be measured) [123]. The relationship is experimentally calibrated to be

$$E_L = \left( \frac{E_H}{423\sqrt{\mu\text{J}}} \right)^2 \quad (2.24)$$

where  $E_L$  and  $E_H$  are in unit of  $\mu\text{J}$ .

Yb plume is not collimated. Isotope selectivity should be achievable by placing some skimmers between the Yb foil and the trap such that the neutral Yb arriving the trap is perpendicular to the 399.91 nm laser beam, as demonstrated in [50] for loading  $\text{Ca}^+$  ion.

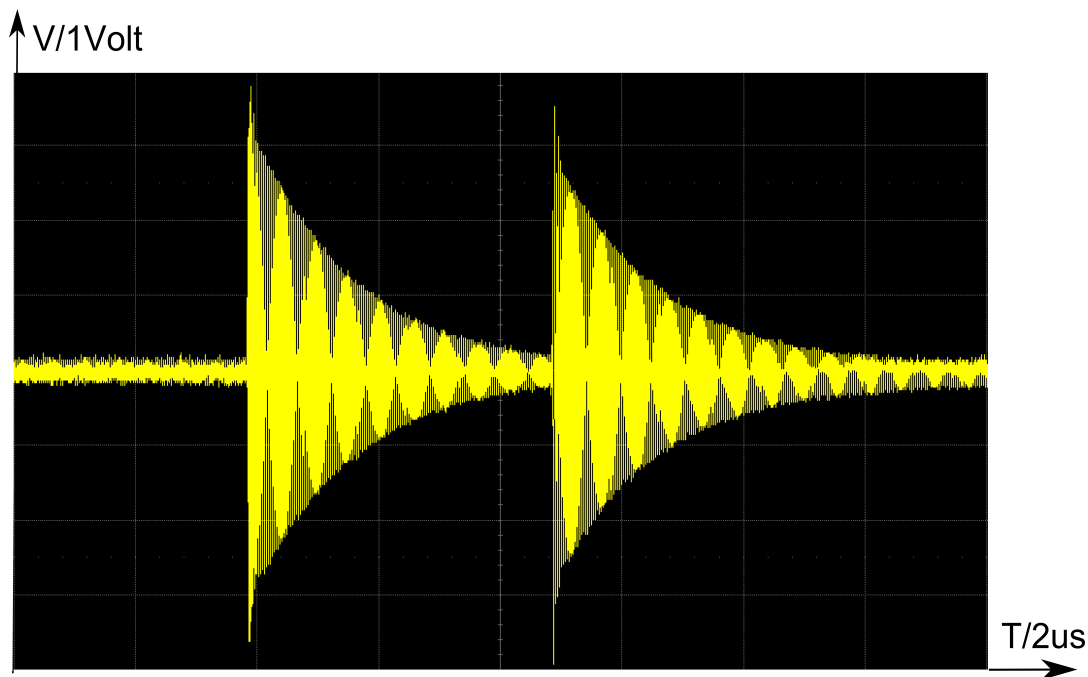


Figure 2.2: Back reflection from the resonator when the rf signal coupled into the resonator is switched off and then switched on  $5 \mu\text{s}$  later. The first packet shows the dissipation of the resonator while the second one shows the charging of the resonator.

Although the loading itself is not isotope-selective in our case, we manage to select the specific isotope starting from an ion cloud containing various isotopes. It is achieved by quickly reducing the trap depth for a few  $\mu\text{s}$  while continuously laser cooling the desired isotope. Before we proceed to the isotope purification, we would like to introduce the trap “off-on” techniques.

The trap-driving signal from the 30 MHz rf generator is sent through a rf switch that is controlled by a TTL signal (generated by a field-programmable

gate array (FPGA)). The trap depth is reduced by briefly switching this rf signal off. Fig. 2.2 shows the back reflection from the resonator after the rf signal is switched off for  $5 \mu\text{s}$  and then switched on. The time constant for the electromagnetic field decay inside the resonator is [135]  $\tau = 2Q/\Omega \sim 1.6 \mu\text{s}$ <sup>1</sup>, as shown by the first packet in Fig. 2.2. The voltage on the trap rods decreases on the same time scale as well. The trap is then switched on, as shown by the second packet in Fig. 2.2.

The trap may lose the ions during the time when the rf signal is off. It is experimentally verified that the ions have a higher probability to escape from the trap if the off-time interval is longer. It is also found that increasing the axial confinement while maintaining the radial trapping frequency<sup>2</sup> increases the ions-escape probability for a fixed off-time interval. On the other hand, increasing the radial confinement while keeping the axial confinement fixed decreases this probability. The latter one can be attributed to the increase of minimum rf power coupled to the trap at the end of the off-time, while the former one is probably because axial confinement weakens the confinement along the radial direction, and this effect is particularly prominent when the radial confinement is weak, as shown in Eqn. 2.22 and Eqn. 2.23. We tentatively conclude that the ions escape from the trap due to the change of the trap parameters  $a$  and  $q$  to the trap instability region when rf voltage is lowered. As the Mathieu equations do not always have stable solutions. Such a solution depends on the  $a$  and  $q$  parameters in Eqn. 2.7. For more details, see [73; 112].

Moreover, we find that the probability to lose the ions that are directly

<sup>1</sup>The  $Q$  and  $\Omega$  here are the resonator quality factor and the trap driving frequency, respectively.

<sup>2</sup>Since the axial confinement weakens the radial confinement, the trap rf power is increased to obtain a fixed radial trapping frequency.

Doppler cooled is lower than the ions that are not. This effect is exploited for purifying the isotope. By carefully choosing the off-time interval, we ensure that only a small fraction of the ion cloud can escape during a single off-on cycle. If we repeat the off-on cycle for many times (typically on the order of 50 times depending on the off-time interval), starting from a cloud of ions with various isotopes, we end up with an isotope-purified crystal. We then adjust the off-time interval such that the probability to lose one single ion is low for one cycle but the ion still can escape from the trap after many cycles<sup>1</sup>. By continuing the off-on cycles, the crystal containing specified number of ions can be obtained in this top-down fashion. Purified  $^{174}\text{Yb}^+$  and  $^{171}\text{Yb}^+$  crystals with different numbers of ions can be routinely obtained. Extension to other isotopes of  $\text{Yb}^+$  and other species of ions should be feasible.

This loading method is not efficient since we usually start with more ions than we really need. But the off-on techniques can be easily combined with other loading methods where undesired ions are present. In particular, it plays a significant role in obtaining a single trapped molecular ion ( $\text{SiO}^+$ ) as shown later.

### 2.2.3 Loading with $\text{Yb}^+$ ions from laser ablation

As mentioned previously, the ejected plume produced by an ablation pulse contains ions as well as neutral atoms. But normally these ions can not be loaded into the trap since the trap potential is conservative, i.e. the kinetic energies gained when the ions fly towards the trap center are enough for the ions to escape. However, if the trap depth dynamically changes when the ions travel through the

---

<sup>1</sup>It is also noted that the probability for a particular ion to escape is smaller when the cloud contains less ions. This is probably because in this case the Coulomb interaction between ions is weaker.

trap volume, some of the ions may be captured [46; 75; 162]. This effect can be exploited naturally with laser ablation, since the trap depth can be perturbed if the amount of charged particles travelling through the trap area is huge. The ions open the door of the trap for themselves. We demonstrate loading of  $\text{Yb}^+$  with this mechanism.

We find that when the single-pulse energy of the ablation laser is above 15  $\mu\text{J}$ , the ions can be loaded without any other photoionization beams (369 nm and 399.91 nm lasers). The change of the trap depth during the loading is verified by monitoring the back reflection of the resonator [46].

This method is not as “clean” as using the Yb oven to load  $\text{Yb}^+$  ions since a great amount of particles are produced during the ablation. The neutral particles from the plume may be deposited inhomogeneously on the trap rods and the charged particles may leave stray charges on the insulators near the trap. These effects induce micromotion as well as increase the heating rate of the ions.

Despite these adverse effects, a similar ablation method is applied to trap  $\text{SiO}^+$  ions as there are no better alternatives presently.

## 2.3 Doppler cooling of the ion

### 2.3.1 Theory

Trapped ion is the first physical system that was laser cooled, or more specifically, Doppler cooled [103; 154]. Since then, Doppler cooling has become an ubiquitous technique used to produce both cold ions and cold neutral atoms.

For the discussion of Doppler cooling, we consider a simple model of a two-level ion characterized by a resonant transition frequency  $\omega_a$  and radiative linewidth

$\Gamma$  ( $\Gamma = 1/\tau$ , where  $\tau$  is the lifetime of excited state). Imagine a single ion oscillating inside a one-dimension harmonic trap with trapping frequency  $\omega_t$ , and interacting with a co-propagating laser beam with wavelength of  $\lambda$  and frequency close to  $\omega_a$ . Suppose  $\Gamma \gg \omega_t$ , i.e. the period of ion oscillation is much larger than the lifetime of ion's excited state. In this case, we can treat the photon absorptions and emissions as occurring instantly [155] (such that the ion is essentially free during absorption/emission events [73]). When the ion absorbs a photon from the laser beam, its momentum changes by  $\Delta\mathbf{p}_{ab} = \hbar\mathbf{k}$ , where  $\hbar$  is the reduced Planck constant and  $\mathbf{k}$  ( $|\mathbf{k}| = 2\pi/\lambda$ ) is the wave vector. The ion is in the excited state after this photon absorption. It then decays back to ground state in a few nanoseconds for typical atomic ions used in quantum information experiments. Unlike the photon absorption process, the spontaneous emission is isotropic and does not have preferred directions. This effect results in a random walk in momentum space.

After this absorption-emission process is repeated many times, the recoil momentum kicks from the spontaneous emission tend to cancel each other, resulting in zero net momentum transfer,  $\langle\Delta\mathbf{p}_{se}\rangle = 0$ . If the absorption is totally random during the trap oscillation, i.e. it has equal probability to happen over the whole oscillation cycle, the imparted momentum to the ion by the absorption will average to zero as well. No momentum will be gained during the absorption and emission process. However, the symmetry of the photon absorption process is broken due to the Doppler effect. This preferential absorption gives rise to dissipation. If the laser is tuned slightly below the transition frequency  $\omega_a$ , the ion is more likely to absorb a photon when the ion oscillates towards the laser source than when it moves in the opposite direction of the incoming laser beam. This velocity-dependent absorption reduces the kinetic energy of the ion. This is

called Doppler cooling.

Apparently there is a limit to the temperature the ion can eventually achieve due to this kind of cooling. Suppose the ion is initially at rest, i.e. it has zero kinetic energy<sup>1</sup>. The random walk in phase space due to recoils from the absorption and emission of photons will actually heat the ion up because  $\langle \mathbf{p}^2 \rangle \neq 0$  although  $\langle \mathbf{p} \rangle = 0$ . In the end, the heating owing to these random recoils (fluctuation) and the cooling due to the velocity-dependent absorption (dissipation) will reach an equilibrium. In a true one-dimensional problem [78], when the laser is tuned below the atomic resonance frequency  $\omega_a$  by  $\Gamma/2$ , the minimum temperature  $T_D$  that can be achieved is [156]

$$T_D = \hbar\Gamma/(2k_B) , \quad (2.25)$$

where  $T_D$  is called Doppler limit and  $k_B$  is the Boltzmann constant. Here we take the thermal energy to be  $k_B T_D/2$  for that degree of freedom, i.e.  $k_B T_D/2 = E_{eq}$ , where  $E_{eq}$  is the statistical average of ion energy over long time.

For an ion in a 3D trap, if the laser beam is at an oblique angle to all axes, i.e. no mode is perpendicular to the laser, then all the modes are cooled. When the laser has the same projection along all three directions, the cooling limit in all directions will be the same as the true one-dimensional case given by Eqn. 2.25 [59; 159]. It is worth mentioning that it is possible to achieve cooling in a certain direction slightly below the Doppler limit by aligning the laser in such a way that it has larger projection along this direction. This is because the cooling rate along this direction increases while the heating rate due to the spontaneous

---

<sup>1</sup>It is displaced slightly from the trap center owing to the averaged radiative pressure described above [156].

emission does not change. Note that cooling in one direction below the Doppler limit comes at the cost of a strong increase in the minimum temperature along other directions [59; 159].

### 2.3.2 Experimental Doppler cooling of $^{171}\text{Yb}^+$

We assumed previously that the ion is a two-level system thus it can be cooled by a single laser slightly red detuned from the resonant frequency. In practice, the ion has a much more complicated energy level structure. Usually at least one additional repumper laser is necessary to close a cycling transition.

Even more levels are involved in the Doppler cooling of the  $^{171}\text{Yb}^+$  ion presented in this thesis, as shown in Fig. 2.3. The cooling is achieved using the  $^2\text{S}_{1/2} |F = 1\rangle \rightarrow ^2\text{P}_{1/2} |F = 0\rangle$  transition at 369.53 nm. Around 20 mW of laser power at 369.53 nm is produced by a Toptica TA-SHG pro laser by frequency-doubling a strong 739.06 nm laser beam (produced by amplifying a diode laser light with a tapered amplifier) in a bow-tie cavity. Part of the output is sent through an electro-optic modulator (EOM, Newport 4851-02) with a resonant frequency around 7.37 GHz. The resulting positive second-order sideband repumps the population trapped in the hyperfine state  $^2\text{S}_{1/2} |F = 0\rangle$  by coupling it to the state  $^2\text{P}_{1/2} |F = 1\rangle$ . The beam is then sent through an acousto-optic modulator (AOM) and the positive first order beam is coupled to a single-mode fiber. The fiber output is sent to the trap. The AOM in the beam path ensures that the beam can be switched on and off in less than 1  $\mu\text{s}$  and the single-mode fiber facilitates the beam alignment and performs spatial-mode filtering. A magnetic field of a few gauss in a proper direction is applied to destabilize the dark states in  $^2\text{S}_{1/2} |F = 1\rangle$  manifold [5].

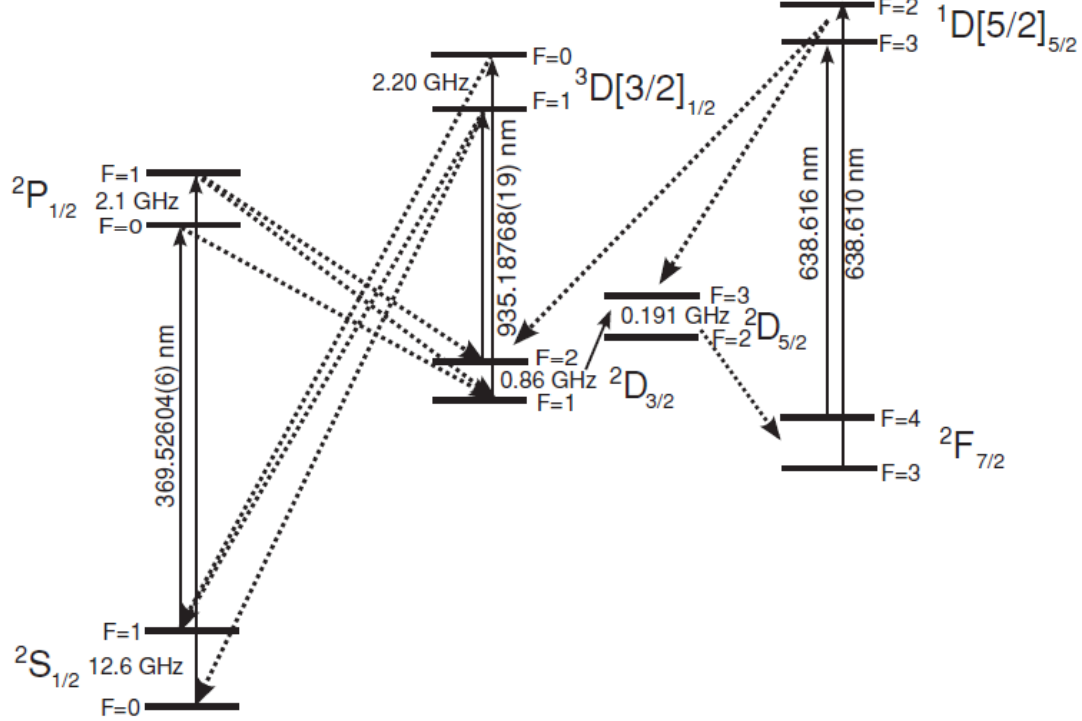


Figure 2.3: Energy levels relevant to the Doppler cooling of  $^{171}\text{Yb}^+$  [94]. Doppler cooling is performed on the transition  $^2\text{S}_{1/2} |F = 1\rangle \rightarrow ^2\text{P}_{1/2} |F = 0\rangle$  with a 369.53 nm laser. Off-resonant coupling to  $^2\text{P}_{1/2} |F = 1\rangle$  gives rise to population trapping in  $^2\text{S}_{1/2} |F = 0\rangle$ . It is depopulated by adding sidebands to the 369.53 nm laser with an EOM (see text). A 935.19 nm laser with sidebands generated with an EOM addresses the  $^2\text{D}_{3/2}$  manifold (it is populated due to small branching from  $^2\text{P}_{1/2}$  manifold) by coupling it to  $^3\text{D}[3/2]_{1/2}$  that quickly decays back to  $^2\text{S}_{1/2}$ . The ions may also end up in a low-lying metastable  $^2\text{F}_{7/2}$  state (lifetime: a few years) a few times per hour, which quenches the cooling cycling. An extra laser at around 638.61 nm returns the ion back to the cooling cycle.

The  $^2\text{P}_{1/2}$  manifold may also decay to the metastable  $^2\text{D}_{3/2}$  manifold (lifetime 51 ms) with a small branching ratio (0.5%). It is depopulated with a commercial external-cavity diode laser at 935.19 nm (Toptica DL pro). Similar to the addressing of population trapped in hyperfine states of  $^2\text{S}_{1/2}$ , the 935.19 nm laser is also phase-modulated with an EOM at 3.07 GHz to repump populations from both  $|F = 1\rangle$  and  $|F = 2\rangle$  hyperfine sublevels of  $^2\text{D}_{3/2}$ . Owing to the presence of

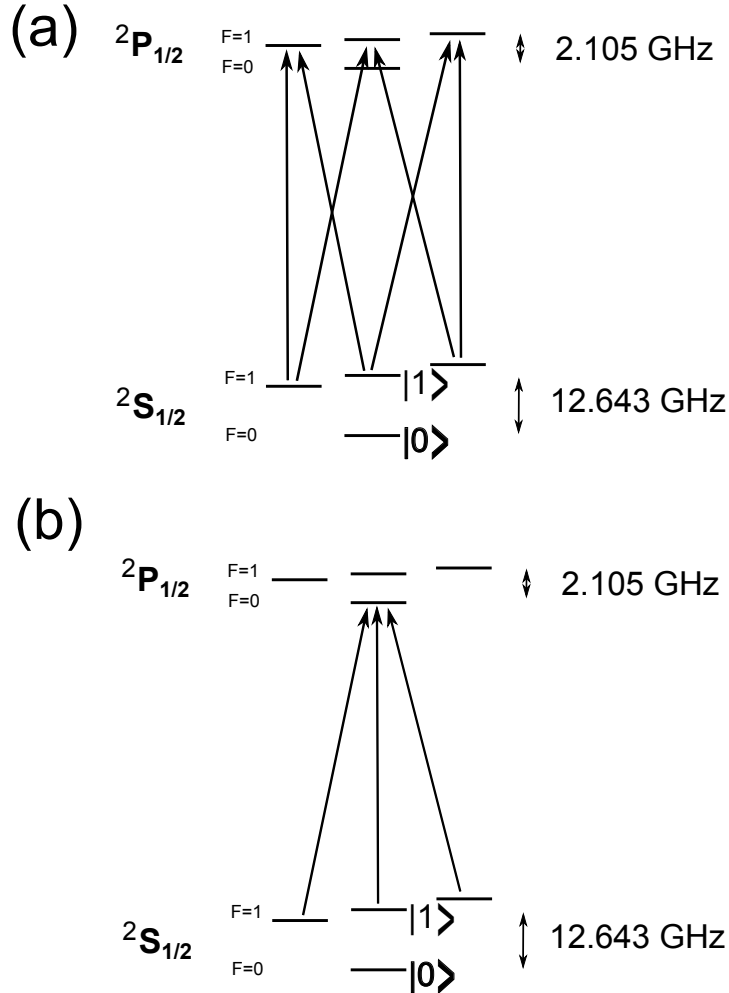


Figure 2.4: Schemes for state initialization and detection. (a) The ion is initialized in state  $|0\rangle$  by driving the transition  ${}^2S_{1/2} |F=1\rangle \rightarrow {}^2P_{1/2} |F=1\rangle$ . (b) State detection with standard fluorescence techniques by application of light that is resonant with the transition  ${}^2S_{1/2} |F=1\rangle \rightarrow {}^2P_{1/2} |F=0\rangle$ . If the ion is in state  $|1\rangle$ , it scatters many photons; if the ion is in state  $|0\rangle$ , few photons can be collected.

the metastable  ${}^2F_{7/2}$  state with very long lifetime (around 6 years), the cycling transition may quench a few times per hour. A homemade external-cavity diode laser at 638.61 nm is added to empty the  ${}^2F_{7/2}$  state and return the ion to the cooling-cycle transition.

State initialization and detection are essential for quantum information processing. The initialization of the ion in state  ${}^2S_{1/2} |F = 0, m_F = 0\rangle \equiv |0\rangle$  is performed by another 369.53 nm beam that is phase-modulated by an EOM at 2.105 GHz, which matches the hyperfine splitting of  ${}^2P_{1/2}$  state. The carrier of the EOM couples resonantly the transition  ${}^2S_{1/2} |F = 1\rangle \rightarrow {}^2P_{1/2} |F = 0\rangle$ , while the positive first order couples the transition  ${}^2S_{1/2} |F = 1\rangle \rightarrow {}^2P_{1/2} |F = 1\rangle$ . The ion is pumped into the dark state  $|0\rangle$  after scattering a few photons (see Fig. 2.4) with almost unit fidelity. The same beam with the EOM switched off is used for state detection. The ion scatters many photons if it is in state  ${}^2S_{1/2} |F = 1, m_F = 0\rangle \equiv |1\rangle$  and few photons if the ion is in state  $|0\rangle$  (see Fig. 2.4).

The overall photon detection efficiency in our setup is around 0.08%. We experimentally choose the detection-beam power such that, if the ion is in state  $|1\rangle$ , we can collect 10 photons on average during 1 ms. We set the photon-number threshold to be 2, i.e. if more than two photons are detected, the ion is defined to be in state  $|1\rangle$ ; otherwise, the ion is defined to be in state  $|0\rangle$ . The detection fidelity for state  $|1\rangle$  is 97.5%, while the detection fidelity for state  $|0\rangle$  is 99.4%.

For efficient cooling and state manipulation of  ${}^{171}\text{Yb}^+$ , the 369.53 nm laser is stabilized in frequency to well within the linewidth of the main transition. To achieve this, the fundamental laser before the frequency doubling, i.e. 739.06 nm laser, is locked to a cavity using Pound-Drever-Hall techniques [9; 35]. The length of this cavity is then stabilized to an absolute frequency reference in iodine using saturated-absorption spectroscopy.

For more details of the laser system regarding Doppler cooling, state initialization and detection of  ${}^{171}\text{Yb}^+$ , see [108].

### 2.3.3 Compensation of micromotion

Once the ion is Doppler cooled, its micromotion can be detected and compensated. The horizontal or vertical shift of ion's position from the nodal line causes excess micromotion along the same direction. For detection of micromotion along horizontal (vertical) direction only, we align the cooling laser in the horizontal (vertical) plane (with substantial projection along radial direction) and monitor the modulation of the fluorescence rate induced by Doppler shift with a time-to-digital converter (TDC) [6]. The TDC is synchronized with the trap rf signal and is triggered once every four cycles while the detection of the arrival of a photon serves as the stop pulse. Since the rf frequency is much larger than the counting rate of the collected photons, the probability to detect one more photon after the stop pulse owing to the first photon is negligible. It means that the probability to detect a photon is uniform over the time interval between two successive triggers when the modulated Doppler shift due to micromotion is absent. When micromotion is present, however, the TDC histogram as a function of the delay between the start and stop is a sinusoidal curve with the same frequency as the trap rf signal. One can extract a modulation amplitude as an indication of the amplitude of the micromotion, i.e. the radial displacement of the ion from the nodal line.

Independent control of the DC voltages of two neighboring rods offers full control of this radial displacement. One can shift the ion's equilibrium position horizontally or vertically in the radial plane independently by scanning the difference or sum of these two voltages. With a computer-controlled digital-to-analog converter (DAC), the scanning is automated, and so is finding the minimum modulation amplitude of the TDC histogram for a single ion (for fixed number of stop

pulses, i.e. detected photons). We can compensate the micromotion on a daily basis (to the level of 2 mV on the rods) in about one minute.

## 2.4 Cooling to the motional ground state

### 2.4.1 Theory

After Doppler cooling, the ion's (kinetic and potential) energy is around  $\hbar\Gamma/2$ . It corresponds to a mean phonon number

$$\langle n \rangle \sim \Gamma/(2\omega_t) . \quad (2.26)$$

For a typical atomic ion and a typical trapping frequency, this corresponds to a few phonons. For  $\text{Yb}^+$  and a trapping frequency of around 1 MHz used in this thesis,  $\langle n \rangle \sim 10$ . The motional state after Doppler cooling is a mixed state and the phonon number follows a thermal distribution [73; 95]

$$P_n = \frac{\bar{n}^n}{(\bar{n} + 1)^{n+1}} . \quad (2.27)$$

The motional state at this level can only show limited quantum effects. A higher population of ground state is required as a prerequisite for preparation of other nonclassical states [95]. Note that Doppler cooling is always applied first to pre-cool the ion, followed by whatever scheme is used later for ground state cooling.

Cooling to the ground state has been achieved before by sideband cooling [30; 77; 113; 118], Raman sideband cooling [18; 29; 47; 98], electromagnetic induced transparency (EIT) cooling [84; 100; 117], cavity sideband cooling [76; 146] and microwave radiation cooling [31; 64; 111; 148] (see Chapter 5). All these schemes

rely on the coupling of the motional states of the ion to its internal states. And it is essential to resolve the sidebands due to the ion's motion in the trap for all of them.

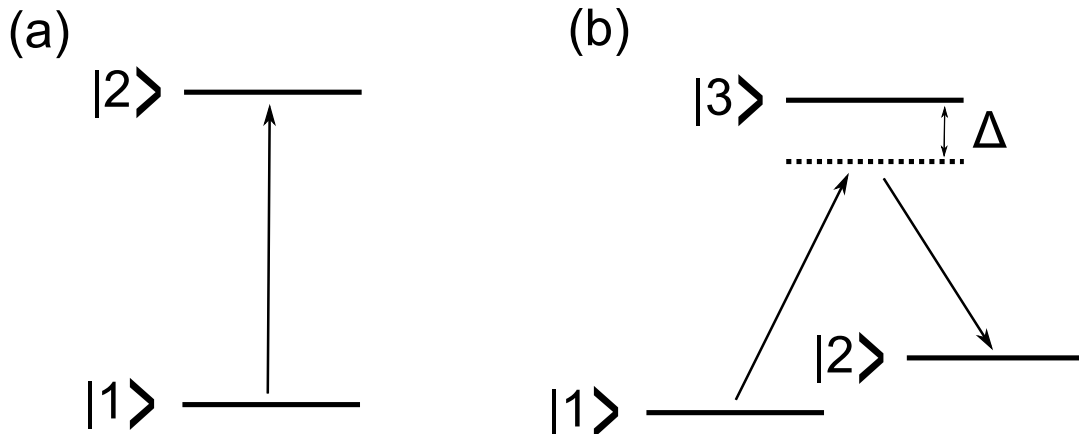


Figure 2.5: Single-photon transition and Raman transition. (a) A narrowband laser drives a single-photon transition  $|1\rangle \rightarrow |2\rangle$  directly. (b) States  $|1\rangle$  and  $|2\rangle$  are Raman coupled via a (virtual) excited state  $|3\rangle$  by two phase-locked lasers. Both lasers are detuned from the excited state by  $\Delta$ .

Sideband cooling and Raman sideband cooling are the two most widely used methods for ground state cooling. For sideband cooling, a very narrow transition (on the order of a few Hz), usually dipole forbidden, is driven with a narrowband laser. For Raman sideband cooling, the transition between states  $|1\rangle$  and  $|2\rangle$  (both are usually sublevels of ground states) is driven with a pair of phase-locked lasers that are detuned from an excited state  $|3\rangle$  (see Fig. 2.5). It can be shown that Raman transition is formally equivalent to a narrow single-photon transition by adiabatically eliminating the third near-resonant excited state  $|3\rangle$  [73]. The wave vector will be replaced by an effective one

$$\mathbf{k}_{eff} = \mathbf{k}_1 - \mathbf{k}_2, \quad (2.28)$$

where  $\mathbf{k}_1$  and  $\mathbf{k}_2$  are wave vectors of the Raman beams. When both Raman beams are detuned from state  $|3\rangle$  by the same amount  $\Delta$ , the effective Rabi frequency is [20]

$$\Omega_{eff} = \frac{\Omega_1\Omega_2}{2\Delta}, \quad (2.29)$$

where  $\Omega_1$  and  $\Omega_2$  are the Rabi frequencies of the transitions  $|1\rangle \rightarrow |3\rangle$  and  $|2\rangle \rightarrow |3\rangle$ , respectively. The effective width of  $|1\rangle$  and  $|2\rangle$ , coming from the off-resonant scattering of level  $|3\rangle$ , is on the order of  $\gamma\Omega_{eff}/\Delta$ , where  $\gamma$  is the width of  $|3\rangle$  [20].

In the following theoretical description of the coupling between motional and internal states, we will use the single-photon transition for simplicity. The treatment of the Raman transition is similar and in the experiments described in this thesis we will use Raman transitions for sideband cooling.

Classically the sidebands arise from the periodic frequency modulation of the laser seen in the rest frame of the ion owing to the Doppler effect [155; 156]. Instead of a monochromatic light, the ion confined in the trap with a trapping frequency  $\omega_t$  sees a range of frequencies which consist of the initial frequency (carrier) and a series of sidebands separated by trapping frequency. When the frequency of a sideband is smaller (greater) than carrier by  $n\omega_t$ , we call it the  $n$ -th red (blue) sideband. Suppose a single ion oscillates inside the trap with an amplitude of  $\Delta x$ , then the maximum speed  $v_{max}$  can be calculated using

$$\frac{1}{2}mv_{max}^2 = \frac{1}{2}m\omega_t^2\Delta x^2, \quad (2.30)$$

which leads to

$$v_{max} = \omega_t\Delta x. \quad (2.31)$$

The amplitude of frequency modulation due to the Doppler effect is

$$\begin{aligned}\Delta\omega &= kv_{max} \\ &= \frac{2\pi\omega_t\Delta x}{\lambda},\end{aligned}\tag{2.32}$$

and the frequency modulation index  $\beta = \Delta\omega/\omega_t$  is

$$\beta = \frac{2\pi}{\lambda}\Delta x.\tag{2.33}$$

The intensities of the carrier and sidebands follow the Bessel function of the first kind <sup>1</sup> (see Fig. 5.3). It is proportional to  $\beta^n$  for the  $n$ th sideband when  $\beta$  is small compared to unity. This sets a lower limit for  $\beta$ . Given that the oscillation amplitude of the ion is typically on the order of 10 nm after Doppler cooling, this limit mainly constrains the field wavelength. For long-wavelength radiation, like microwave, the sidebands can not be driven efficiently because  $\beta$  is much smaller than unity. For the hyperfine splitting of electronic ground state of  $^{171}\text{Yb}^+$ , the corresponding transition frequency is 12.6 GHz, the wavelength is 2.38 cm and  $\beta$  is on the order of  $10^{-7}$ .

On the other hand, for large values of the frequency modulation index  $\beta$ , some sidebands may also be driven with low efficiencies. This is because the intensities

---

<sup>1</sup>The frequency modulation is equivalent to phase modulation since the accumulated phase in frequency modulation is

$$\int_0^t (\omega_l + \Delta\omega \cos(\omega_t t)) dt = \omega_l t + \beta \sin(\omega_t t),\tag{2.34}$$

where  $\omega_l$  is the laser frequency in the lab frame. The sidebands and their intensities can be extracted from

$$e^{i(\omega_l t + \beta \sin(\omega_t t))} = \sum_{n=-\infty}^{n=\infty} J_n(\beta) e^{i(\omega_l + n\omega_t)t},\tag{2.35}$$

where  $J_n(\beta)$  is the  $n$ -th Bessel function of the first kind.

of the sidebands do not increase monotonically with  $\beta$  when the modulation index is on the order of 1. They can even have zero points, which correspond to missing sidebands. For example, for the first red sideband,  $J_1(\beta) = 0$  for  $\beta \approx 3.8$ . If  $\beta > 3.8$  and we use the first red sideband to perform sideband cooling, instead of ground state, the ion will be “trapped” in the state where  $\beta \approx 3.8$ . Given that the typical wavelength of the light is on the order of hundreds of nanometers, this limit mainly constrains the oscillation amplitude where efficient sideband cooling can be achieved.

In the quantum mechanical treatment, the oscillation amplitude should be replaced by the spatial extent of the wave function of the ion. For the state  $|n\rangle$  with  $n$  phonons, the size of the wave packet is

$$\begin{aligned} x_n &= \sqrt{\langle n|x^2|n\rangle} \\ &= \sqrt{x_0^2 \langle n|(\hat{a} + \hat{a}^\dagger)^2|n\rangle} \\ &= \sqrt{2n+1}x_0, \end{aligned} \tag{2.36}$$

where  $x_0 = \sqrt{\hbar/(2m\omega_t)}$  is the spatial extent of the ground-state wave function,  $\hat{a}$  and  $\hat{a}^\dagger$  are the annihilation and creation operators, respectively. The regime when

$$kx_n \ll 1 \tag{2.37}$$

is called Lamb-Dicke regime [73], a regime of strong localization. It corresponds to the upper limit of the frequency modulation index in our classical description.

A parameter

$$\eta = kx_0 \tag{2.38}$$

is called Lamb-Dicke parameter. It resembles the classical frequency modulation

index  $\beta$  when the ion is in the ground state.

All the experiments that demonstrated ground state cooling have an initial Doppler cooling stage that pre-cool the trapped ions to the Lamb-Dicke regime. For a given linewidth of a transition used in Doppler cooling, the Lamb-Dicke criterion sets a lower limit for the trapping frequency for efficient sideband cooling. Combining Eqn. 2.26, 2.36 and 2.37, we obtain

$$\omega_t \gg k_{eff} \sqrt{\frac{\hbar\Gamma}{2m}} . \quad (2.39)$$

For  $^{171}\text{Yb}^+$ , inserting  $\Gamma/(2\pi) = 19.6$  MHz and  $k_{eff} = \sqrt{2}k \approx \sqrt{2} \times 2\pi/375\text{nm}$ <sup>1</sup>, we obtain

$$\omega_t \gg 2\pi \times 570 \text{ kHz} . \quad (2.40)$$

If the trapping frequency satisfies this condition, the ion after Doppler cooling is in the Lamb-Dicke regime.

It is worth mentioning that the strong localization regime, or Lamb-Dicke regime, also implies a low probability to change the motional state after spontaneously emitting a photon. Once the first red sideband is resolved and has reasonable intensity, one tunes the laser at this frequency. The ion absorbs one photon of energy  $\hbar(\omega_a - \omega_t)$ , bringing the ion to the excited state and at the same time removing one motional quanta. When the ion spontaneously emits a photon and returns to the ground state, its vibrational energy may, in general, increase or decrease. The average change of vibrational energy is the recoil energy  $R = \hbar^2 k^2 / (2m)$ . The condition for cooling to occur is that the recoil energy  $R$  is

---

<sup>1</sup>In our case, two Raman beams around 375 nm are perpendicular to each other.

smaller than the energy of a motional quanta  $\hbar\omega_t$  [156], i.e.

$$\frac{\hbar^2 k^2}{2m} \ll \hbar\omega_t , \quad (2.41)$$

which leads to

$$k\sqrt{\frac{\hbar}{2m\omega_t}} \ll 1 , \quad (2.42)$$

i.e.

$$\frac{2\pi}{\lambda}x_0 = \eta \ll 1 . \quad (2.43)$$

This condition is clearly satisfied if the ion is in the Lamb-Dicke regime. We emphasize that it is only a necessary condition for the system to achieve ground state cooling.

The condition of localization can also be recast in the momentum space [20]

$$\Delta x \ll \frac{\lambda}{2\pi} \implies \Delta p = \frac{\hbar}{\Delta x} \gg \frac{2\pi\hbar}{\lambda} = \hbar k . \quad (2.44)$$

This formula means that the momentum dispersion of the ion is much larger than the photon recoil momentum. It suggests that the wave functions in phase space before and after the photon recoil almost overlap with each other. Consequently, the transition without changing the motional state, i.e. the carrier, dominates over the sidebands.

At last, we would like to point out that, in some sense, sideband cooling is still one kind of Doppler cooling, but it is performed at a very weakly allowed transition so that  $\Gamma \ll \omega_t$ . Instead of treating the photon absorptions and emissions as occurring instantly, we consider the coherence during successive oscillations, which gives rise to sidebands [155]. However, it is still the asymmetry in the

photon absorption and the symmetry in the photon emission that gives rise to dissipation<sup>1</sup>. In this case, the cooling limit is not  $\hbar\Gamma/2$  any more, simply because it is lower than the lowest energy that quantum mechanics allows for a harmonic oscillator, i.e.  $\hbar\omega_t/2$ . Instead it is  $\langle n \rangle_{min} \simeq (\Gamma/(2\omega_t))^2 \ll 1$  [98; 155]. In practice, a transition at such a low rate is usually not capable of achieving ground state cooling due to the presence of other heating effects. This is overcome by oversaturating this transition and coupling the upper state via a fast transition to another high-lying state that is strongly coupled to the ground state. It effectively “lends some width” to a narrow transition and recycles to the ground state very rapidly [131].

For the full quantum mechanical treatment of internal and motional states coupling, see [73; 131]. We only outline the derivation here.

The Hamiltonian of the system can be written in three parts

$$\hat{H} = \hat{H}_A + \hat{H}_M + \hat{H}_I , \quad (2.45)$$

where  $\hat{H}_A$ ,  $\hat{H}_M$  and  $\hat{H}_I$  describe the internal electronic level of the ion, the motional Hamiltonian and interactions mediated by the applied laser fields, respectively. We can write down the expressions of these parts as

$$\hat{H}_A = \hbar\omega_a \hat{\sigma}_z , \quad (2.46)$$

$$\hat{H}_M = \hbar\omega_t (a^\dagger a + 1/2) , \quad (2.47)$$

$$\hat{H}_I = \frac{\hbar\Omega}{2} (\hat{\sigma}_+ + \hat{\sigma}_-) \left( e^{i\eta(a+a^\dagger)} e^{-i\omega_t t} + e^{-i\eta(a+a^\dagger)} e^{i\omega_t t} \right) , \quad (2.48)$$

where  $\hat{\sigma}_z = |e\rangle\langle e| - |g\rangle\langle g|$  is the Pauli matrix,  $\omega_t$  is the laser frequency,  $\Omega$  is

<sup>1</sup>This is not true in cavity sideband cooling, where the asymmetry in photon emission leads to dissipation [146].

the Rabi frequency characterizing the coupling between  $|g\rangle$  and  $|e\rangle$  driven by the laser,  $\hat{\sigma}_+ = |e\rangle\langle g|$ , and  $\hat{\sigma}_- = |g\rangle\langle e|$ .

Transforming into the interaction picture with free Hamiltonian  $\hat{H}_0 = \hat{H}_A + \hat{H}_M$  and the interaction  $\hat{H}_I$ , we obtain

$$\hat{H}_{int} = e^{(i/\hbar)\hat{H}_0 t} \hat{H}_I e^{-(i/\hbar)\hat{H}_0 t} . \quad (2.49)$$

Making the rotating-wave approximation (neglecting the term  $\omega_l + \omega_a$ ),

$$\hat{H}_{int} = \frac{\hbar\Omega}{2} e^{i\eta(\hat{a}e^{-i\omega_l t} + \hat{a}^\dagger e^{i\omega_l t})} \hat{\sigma}_+ e^{-i\delta t} + H.c. , \quad (2.50)$$

where  $\delta = \omega_l - \omega_a$  is the detuning and H.c. refers to Hermitian conjugate.

After Taylor expansion of this expression and making rotating wave approximation again, we get expressions describing the sidebands of the transitions. In Lamb-Dicke regime in particular, the dominant terms are

$$\text{for } \delta = 0, \quad \hat{H}_{int} = \frac{\hbar\Omega}{2} (\hat{\sigma}_+ + \hat{\sigma}_-) ; \quad (2.51)$$

$$\text{for } \delta = -\omega_l, \quad \hat{H}_{int} = \frac{\hbar\Omega}{2} \eta (\hat{a}\hat{\sigma}_+ + \hat{a}^\dagger\hat{\sigma}_-) ; \quad (2.52)$$

$$\text{for } \delta = \omega_l, \quad \hat{H}_{int} = \frac{\hbar\Omega}{2} \eta (\hat{a}^\dagger\hat{\sigma}_+ + \hat{a}\hat{\sigma}_-) ; \quad (2.53)$$

which characterize the carrier, the first order red sideband and the first order blue sideband, respectively.

The corresponding Rabi frequencies in the Lamb-Dicke regime to the lowest

phonon-number-dependent order are<sup>1</sup>:

$$\Omega_{n,n} = \Omega (1 - \eta^2 n) \quad (\text{carrier}) ; \quad (2.54)$$

$$\Omega_{n-1,n} = \sqrt{n} \eta \Omega \quad (\text{red sideband}) ; \quad (2.55)$$

$$\Omega_{n+1,n} = \sqrt{n+1} \eta \Omega \quad (\text{blue sideband}) ; \quad (2.56)$$

where  $\Omega_{m,n}$  characterizes the transition from state with  $n$  phonons to  $m$  phonons.

### 2.4.2 Experimental realization of ground state cooling

We use Raman transitions to perform the motional ground state cooling. Raman transitions are typically achieved using two phased-locked laser beams that are separated in frequency domain by the energy difference of the states to be coupled. It requires either two lasers that are phase-locked or a single laser that is modulated at high frequency, which is technically demanding.

For the experiments presented in this thesis, a picosecond mode-locked pulsed laser, i.e. a frequency comb, is used to bridge the large frequency gap [15; 47; 97]. Frequency scanning over one repetition rate  $\nu_r$  is sufficient to address the transitions within the pulse bandwidth  $\nu$  (see Fig. 2.6). For a typical picosecond mode-locked pulsed laser, the repetition rate is  $\nu_t \sim 100$  MHz and the bandwidth is  $\nu \sim 300$  GHz.

In some sense, every single comb tooth works as an individual laser and they are phase-locked naturally by the laser mode-locking. The Raman transition is driven by absorption from one comb tooth and stimulated emission into another. These two comb teeth may come from either a single beam or two beams from

---

<sup>1</sup>For exact expressions, see Eqn. (70) in reference [73].

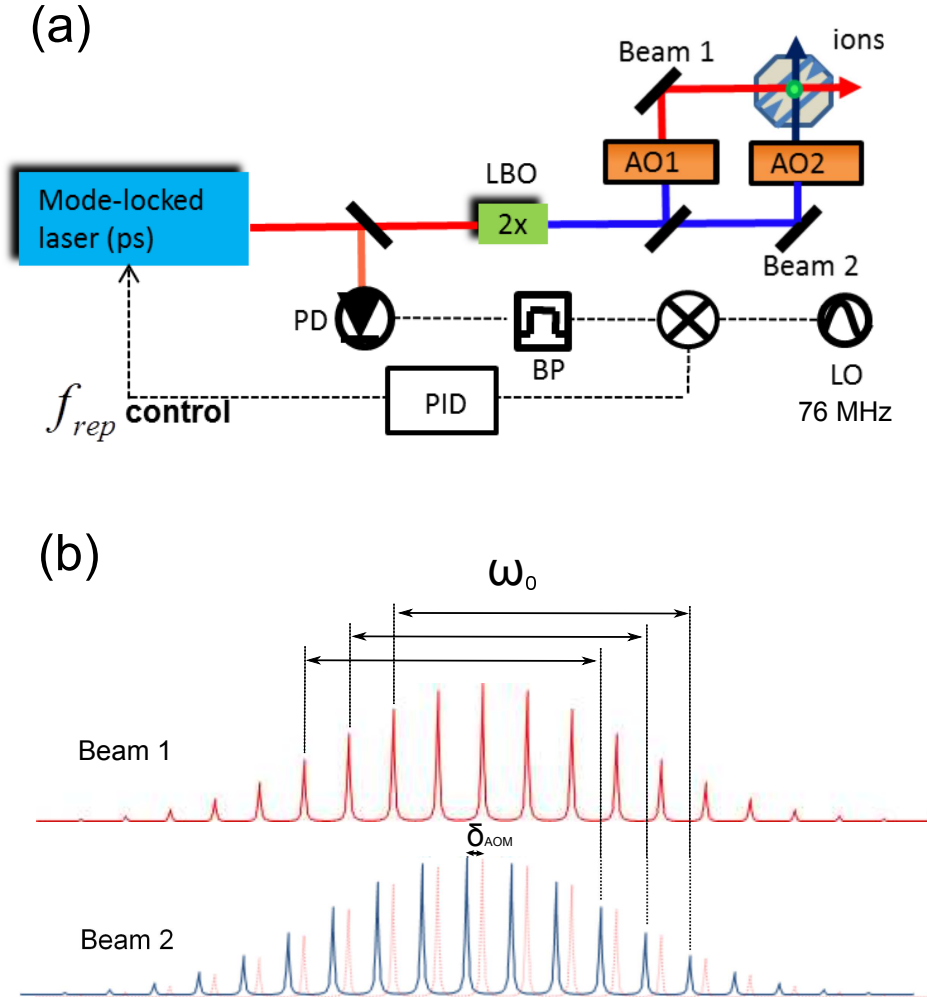


Figure 2.6: Raman coupling with a picosecond mode-locked pulsed laser. (a) Scheme of the experimental setup. The emitted light from a mode-locked Ti:sapphire (Ti:sapph) laser is frequency-doubled by a LBO crystal. It is then split into two and sent through two AOMs (AO1 and AO2 in the figure) to generate a relative frequency offset  $\delta_{\text{AOM}}$  between two beams. The beams are then focused into the ion from two different directions to couple the modes of interest. To achieve stable frequency difference between two comb teeth, the repetition rate of the laser is phase-locked to a stable local oscillator by a feedback controlling a piezo mounted on one of the laser cavity mirrors. (b) By controlling the relative frequency offset of two beams  $\delta_{\text{AOM}}$ , states with separation  $\omega_0 \gg \delta_{\text{AOM}}$  can be Raman coupled. The laser power is utilized efficiently due to the equal spacing of neighboring comb teeth.

different directions. In the latter case the motional states of the ion are coupled to its internal states as described previously. The equal spacing between neighboring comb teeth makes it a very convenient tool, because once the frequency difference between one pair of comb teeth matches the desired energy difference, for any other comb tooth, one can always find one comb tooth satisfying the same condition, as shown in Fig. 2.6(b). This ensures that the power is utilized efficiently. We phase-lock the repetition rate to a stable rf source (Stanford Research, SG382) to make sure that the frequency difference between different comb teeth is stable (see Fig. 2.6(a)). It is worth pointing out that the carrier-envelope phase need not to be locked since the absolute frequency is irrelevant for the Raman transition.

The Raman lasers (Raman beam 1 and Raman beam 2) couple the hyperfine states (see Fig. 2.7) in the electronic ground state of  $^{171}\text{Yb}^+$ , i.e.  $^2\text{S}_{1/2} |F = 0, m_F = 0\rangle \equiv |0\rangle$  and  $^2\text{S}_{1/2} |F = 1, m_F = 0\rangle \equiv |1\rangle$ . Fig. 2.7 shows energy levels involved. States  $|0\rangle$  and  $|1\rangle$  are Raman coupled through the excited  $^2\text{P}_{1/2}$  state (coupling to  $^2\text{P}_{3/2}$  is negligible due to the large detuning  $> 100$  THz). The corresponding Rabi frequency is [153]

$$\Omega_{eff} = \frac{1}{4\hbar^2} \sum_i \frac{\langle 1 | \mathbf{d} \cdot E_2 \hat{\epsilon}_2 | i \rangle \langle i | \mathbf{d} \cdot E_1 \hat{\epsilon}_1 | 0 \rangle}{\Delta_i} \quad (2.57)$$

where  $\mathbf{d}$  is the electric dipole operator,  $E_{1(2)} \hat{\epsilon}_{1(2)}$  characterizes the laser field with  $E_{1(2)}$  the electric field amplitude and  $\hat{\epsilon}_{1(2)}$  the polarization of Raman beam 1 (Raman beam 2),  $|i\rangle$  are the virtual intermediate states of the Raman process and  $\Delta_i$  are the corresponding detunings from the real transitions (see Fig. 2.7).

An additional simplification arises from the fact that the coupling via  $\pi$  light is forbidden by selection rules. This is because neither the transition  $|0\rangle \longleftrightarrow ^2\text{P}_{1/2}$

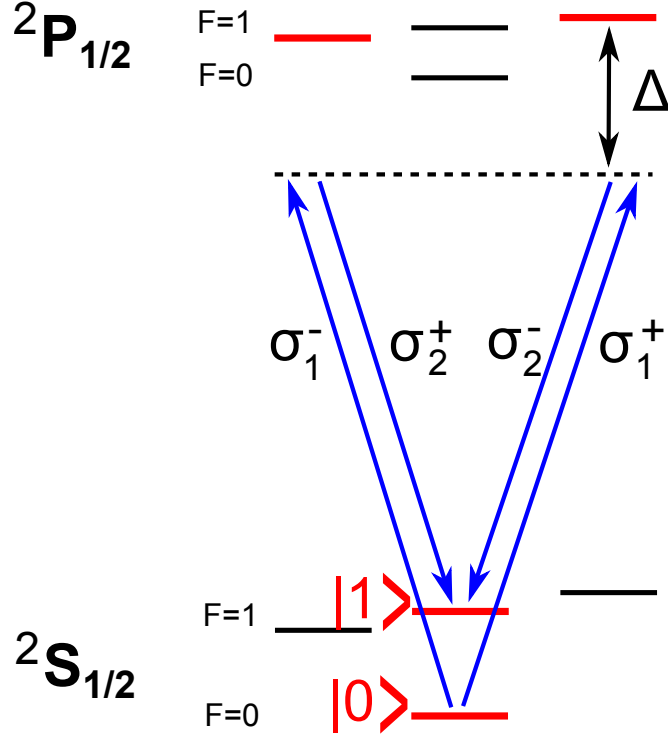


Figure 2.7: Raman coupling between states  $|0\rangle$  and  $|1\rangle$ . Selection rules simplify the Raman coupling, leaving only the red-line states involved. The Raman detuning  $\Delta$  is usually between 10 THz to 30 THz in this thesis.  $\sigma_{1,2}^{\pm}$  refers to the desired Raman beam (beam 1 or beam 2) and its polarization ( $\sigma^+$  or  $\sigma^-$ ) to drive the Raman transition  $|0\rangle \rightarrow |1\rangle$ .

$|F = 0, m_F = 0\rangle$  nor the transition  $|1\rangle \longleftrightarrow ^2P_{1/2} |F = 1, m_F = 0\rangle$  can be driven by  $\pi$  light since the Clebsch-Gordan coefficients in both cases are zero. It indicates that both Raman beams should be linearly polarized and perpendicular to the magnetic field to minimize the projection along  $\pi$  polarization. It also simplifies Eqn. 2.57 since only two intermediate states coupled via  $\sigma^+$  and  $\sigma^-$  light need to be considered (see Fig. 2.7). By calculating Eqn. 2.57 with proper Clebsch-Gordan coefficients indicated in Fig. 2.7 by blue arrows, we know that the polarization direction of these two beams should be perpendicular to each other to make sure that the coupling through two channels interferes constructively.

To produce the Raman beams, the output of a 1.6 W mode-locked Ti:Sapphire laser (pulse duration 3 ps, repetition rate 76 MHz) is frequency-doubled by a Lithium triborate (LBO) crystal, generating about 200 mW of light at 375 nm or so (we change the wavelength from experiment to experiment, the detuning  $\Delta_i$  is typically larger than 10 THz). The resulting beam is then split into two, sent through two separate acousto-optical modulators (AOMs), and focused to a beam waist of 15  $\mu\text{m}$  at the ion position. We change the directions of the beams from experiment to experiment to make sure that the modes of interest are coupled. The path lengths of the two beams are matched to a precision much better than the picosecond pulse length with a homemade retroreflector that can change the path length of one of the beams<sup>1</sup>. The polarizations of the two beams are set to be linear and mutually orthogonal to each other and to the magnetic field to precision better than one percent with a quarter waveplate followed by a half waveplate in each beam.

To achieve sideband cooling, we first apply 1 ms of Doppler cooling to pre-cool the ion to the Lamb-Dicke regime. We then typically apply 150 or so Raman pulses at the first order red sideband. Each pulse is followed by 5  $\mu\text{s}$  of optical pumping to reinitialize the ion back in the  $|0\rangle$  state. The duration of the Raman pulse is increased (determined by the Rabi frequency  $\Omega_{0,1}$  in Eqn. 2.55, initial phonon number after Doppler cooling and number of pulses applied) during the sideband cooling sequence to account for the decreased Rabi frequency of the sideband transition as the mean phonon number decreases.

For the experiments presented in this thesis, we can cool all the modes of

---

<sup>1</sup>Two fast photodiodes (Hamamatsu Photonics, G4176-03) placed at equal distances from the trap center are used to detect the arrival times of the pulses from two beams. The detected arrival times are compared using an oscilloscope (LeCroy, WaveRunner 610Zi) with precision better than the pulse duration. The path lengths are then fine-tuned to optimize the Rabi frequency of the Raman transition.

interest below  $\langle n \rangle \sim 0.05$  phonons. The heating rates of radial normal modes for  $^{171}\text{Yb}^+$  are measured to be around 35/s at the trapping frequency of 1 MHz or so, while the heating rate for axial mode is around 20/s at the trapping frequency of 0.6 MHz.

## Chapter 3

# Quantum logic for the control and manipulation of molecular ions using a frequency comb

A frequency comb laser field can be used to couple internal quantum states of an ion and its motion. This coupling has recently been experimentally demonstrated for hyperfine states of atomic  $\text{Yb}^+$  ion [47]. Due to the large bandwidth and precise control afforded by the frequency comb, it is particularly suitable for addressing multiple molecular energy levels [132]. This allows us to apply “quantum logic” ideas for control and manipulation of molecular states that were initially developed for quantum logic gates in ion trap quantum computing, and subsequently used for precision spectroscopy with atomic ions [120; 125; 126]. In this chapter, based on such quantum logic techniques [33; 120; 125; 126], we propose an experimental scheme to prepare, manipulate and detect the internal states of a cold trapped molecular ion.

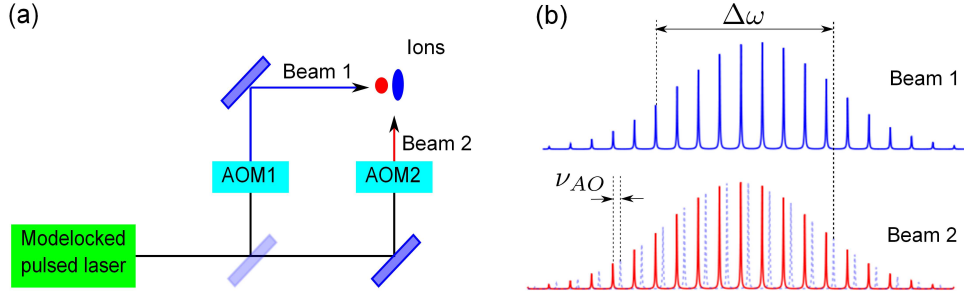


Figure 3.1: The proposed experimental setup. (a) Light emitted by a modelocked pulsed laser with repetition rate  $f_{rep}$  is split into two beams, sent through acousto-optical modulators to offset the relative frequency between two beams by  $\nu_{AO}$  and incident upon the atomic and molecular ions from two different directions. (b) Spectrum of the frequency combs. If resonance conditions are satisfied the setup can drive a stimulated Raman transition between a pair of energy levels  $\Delta\omega$  apart.

### 3.1 Model

The experimental setup that we consider is shown in Fig. 6.1. We confine a diatomic molecular ion together with an atomic ion in a standard rf-Paul trap. Due to Coulomb interaction, the atomic and molecular ions share common modes of motion. The motion of the molecular and atomic ions are cooled to the ground state by sideband cooling [98]. Two laser beams generated by a modelocked pulsed laser with a repetition rate  $f_{rep}$  are offset by frequency  $\nu_{AO}$  with acousto-optical modulators and focused on the ions from two different directions.

In order to drive a stimulated Raman transition between two quantum states separated by  $\Delta\omega$ , the repetition rate  $f_{rep}$  and offset frequency  $\nu_{AO}$  should satisfy the resonance condition

$$\Delta\omega = Mf_{rep} \pm \nu_{AO}. \quad (3.1)$$

Here the integer number  $M$  is the comb index. The time averaged resonance Rabi

frequency between two states coupled by an off-resonance pulsed laser is [47]

$$\Omega = \Omega_0 \left( \frac{\Delta\omega\tau}{e^{\Delta\omega\tau/2} - e^{-\Delta\omega\tau/2}} \right), \quad (3.2)$$

where  $\tau$  is the pulse duration,  $\Omega_0 = s\gamma^2/2\Delta$ , and  $s = \bar{I}/I_{sat}$ ,  $\bar{I}$  is the average intensity,  $I_{sat}$  is the saturation intensity,  $\Delta$  is the detuning of the pulsed laser from an excited state, and  $\gamma$  is the excited state decay rate. The Rabi flopping is suppressed if the energy splitting between two states  $\Delta\omega$  is greater than the bandwidth of the pulsed laser  $1/\tau$ . The typical pulse duration of a mode-locked Ti:sapphire pulsed laser on the order of 100 fs - 1 ps provides sufficient bandwidth to address transitions between rotational and hyperfine states in a molecule. Pulses from both directions should arrive at the position of the ions at the same time, therefore the path length difference between two arms cannot exceed  $c\tau$  (about 30  $\mu\text{m}$  for a 100 fs pulse). This is similar to the requirement on the path length difference in say, parametric down conversion experiments [53]. The Rabi flopping signal between two hyperfine ‘‘clock’’ states of the atomic ion can serve as an alignment tool to ensure the overlap between two pulses at the location of the ions.

To address the motion of the ions we detune the spectral beat note between the two laser beams from the two photon resonance between molecular states  $|m_1\rangle$  and  $|m_2\rangle$  by  $\omega_t$ , the frequency of a common motional mode. In this case the interaction Hamiltonian in the Lamb-Dicke limit has the form [157]

$$\hat{H}_I = \hbar\eta\Omega(a^\dagger\sigma_- + a\sigma_+) \quad (3.3)$$

where  $a^+$  ( $a$ ) is the phonon creation (annihilation) operator for the common

mode of motion of two ions, and  $\sigma_+ = |m_1\rangle\langle m_2|$  ( $\sigma_- = |m_2\rangle\langle m_1|$ ) is the raising (lowering) operator for the transition. The change in the molecular quantum state is accompanied by a simultaneous change of the motional state of the ions. In the ground state of motion, the Rabi frequency of a transition is equal to  $\Omega_s = \eta\Omega$ , where  $\eta = k\sqrt{\hbar/2m\omega_t}$  is the Lamb-Dicke parameter, and  $k$  is the wave vector difference between the two laser beams.

The state of the molecular ion can be detected using aforementioned quantum logic techniques [120; 126]. If the atomic and molecular ions were initially in a ground state of motion, driving a Raman transition that couples the state of the molecular ion  $|m_1\rangle$  to a collective motional mode of the ions generates a phonon if the molecular ion was in the state  $|m_1\rangle$ , and does not change the motion if the molecular ion was in any other state. The phonon can be detected later by coupling the motion of the ions to the spin of an atomic ion, followed by the atomic ion state detection using standard fluorescence technique.

Due to the periodic structure of the frequency comb, scanning the offset frequency  $\nu_{AO}$  produces a spectrum that repeats itself every  $f_{rep}$ . Measurement of the absolute energy difference between two states therefore requires knowledge of both the offset frequency  $\nu_{AO}$  and the comb index  $M$ . The latter can be determined by measuring the spectrum as a function of the offset frequency  $\nu_{AO}$  for several slightly different repetition rates and comparing the results [138].

We can also prepare a molecular ion in a well defined quantum state by coupling the internal and motional degrees of freedom. We start with atomic and molecular ions in the ground state of motion after sideband cooling and drive the  $J, n = 0 \rightarrow J - 2, n = 1$  Raman transition in the molecule, where  $n$  is number of phonons in a given motional mode (see Fig. 3.2). If the ions are in the ground state of motion, decrease of the angular momentum via the  $J, n = 0 \rightarrow J - 2, n = 1$

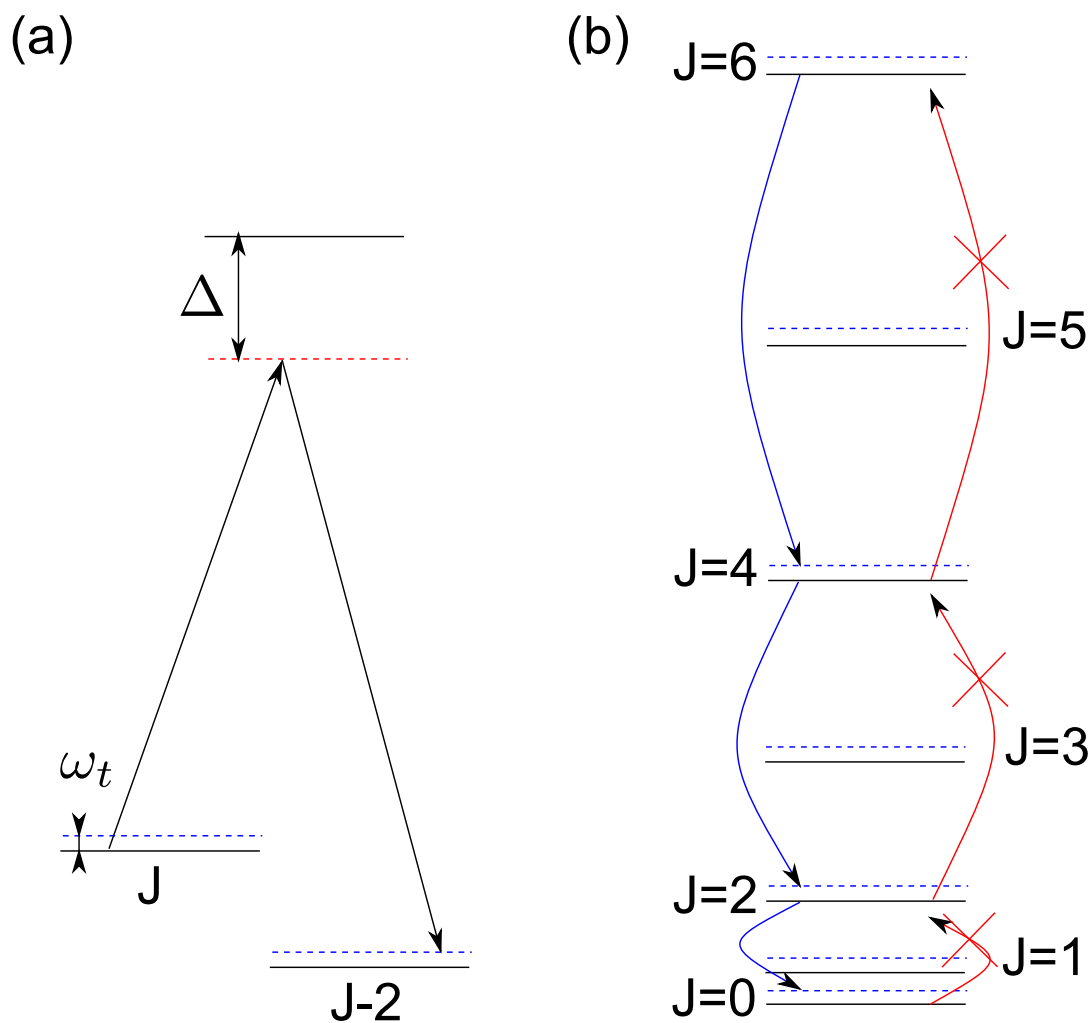


Figure 3.2: Cooling of molecular rotational states. (a) Stimulated Raman transition is driven on a “blue” motional sideband so that Raman transition from rotational state  $J$  to  $J - 2$  adds one phonon to the motional mode of the ions. (b) If the molecule is cooled to the ground state of motion and phonons are continuously removed by sideband cooling of a co-trapped atomic ion, transitions that increase  $J$  are not allowed, leading to an efficient build up of the population in the  $J = 0$  and  $J = 1$  states.

transition is allowed. However, the opposite transition  $J - 2 \rightarrow J$  is not allowed, since it requires subtracting motional energy from the ions that are already in the ground state. If after each step phonons are removed from the trap by sideband cooling, the angular momentum  $J$  of the molecule decreases, leading to a buildup of population in the  $J = 0$  or  $J = 1$  state.

It is interesting to note that this cooling scheme can be made more efficient if we use the periodic structure of a frequency comb. For example, the proper choice of repetition rate and offset frequency allows us to drive transitions between at least two pairs of levels at the same time. In some special cases, for example, heavy molecules with no hyperfine structure confined in a tight trap, when the centrifugal distortion constant  $D$  is small compared to the rotational constant  $B$ , the splitting between energy levels

$$E(J + 2) - E(J) \simeq 6B \left( \left(1 + 6\frac{D}{B}\right) + 4J\left(1 + 15\frac{D}{B}\right) + 4\frac{D}{B}(9J^2 + 2J^3) \right) \quad (3.4)$$

increases almost linearly with  $J$  and can be matched to the periodic structure of a frequency comb, which allows even more pairs of levels to be addressed simultaneously. This can speed up the cooling process even if the Rabi frequencies are not the same for different pairs of levels, since the transition will always result in the net decrease of the angular momentum  $J$  even if a perfect  $\pi$  - pulse for every transition is not produced simultaneously.

The number of Zeeman sublevels in the  $J+2$  state is larger than in the state  $J$ , therefore it is impossible to couple all the sublevels of the upper state to the lower one simultaneously via a Raman transition, which leads to population trapping in the states with higher angular momentum. To avoid it we can alternate the polarization of the Raman beams between several configurations to make sure

that all sub-levels in the upper  $J + 2$  state are coupled to the sublevels of the lower  $J$  state. Alternatively, we can apply a weak magnetic field to mix the Zeeman sublevels. However, the latter approach is less desirable since Zeeman splitting can increase the number of energy levels one has to address.

### 3.2 Possible implementation

As a possible first step towards the implementation of this scheme, we consider a  $\text{SiO}^+$  molecular ion trapped together with an  $\text{Yb}^+$  atomic ion. The spectral properties of  $\text{SiO}^+$  are known [14; 136]. The wavelength for the  $A^2\Pi(\nu = 0) \rightarrow B^2\Sigma^+(\nu = 0)$  transition is about 414 nm, and the  $X^2\Sigma^+(\nu = 0) \rightarrow B^2\Sigma^+(\nu = 0)$  transition wavelength is near 383 nm, close to the 370 nm transition of atomic  $\text{Yb}^+$  ion. Nearly diagonal Franck-Condon factors for the  $X^2\Sigma^+(\nu = 0) \rightarrow B^2\Sigma^+(\nu = 0)$  transition in  $\text{SiO}^+$  maximize the two-photon Rabi frequency. The absence of hyperfine structure for the most abundant molecule  $\text{Si}_{28}\text{O}_{16}$  simplifies the energy level structure.

The energy of rotational states in the ground electronic state  $X$  and vibrational state  $\nu = 0$  is  $E_X(J) = BJ(J+1) + DJ^2(J+1)^2$ , where for  $\text{SiO}^+$   $B = 21.51$  GHz and  $D = 33.1$  kHz [14]. At room temperature about 98% of population is distributed among states with angular momentum from  $J = 0$  to  $J = 35$  of the lowest vibrational state  $\nu = 0$ . While it is still possible to apply the cooling scheme described in the paper directly, the large number of populated levels and magnetic fields can significantly increase the number of required cooling steps. Therefore some initial cooling of the rotational degrees of freedom is desirable.

One approach to decrease the number of populated rotational states is optical pumping with spectrally shaped broadband light [83; 104; 143], as demonstrated

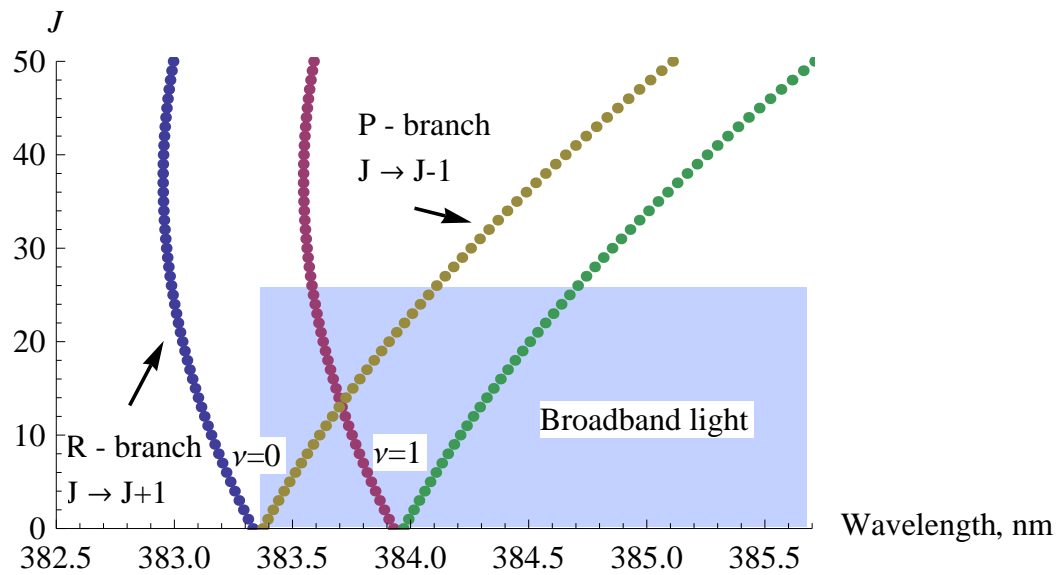


Figure 3.3: Optical pumping scheme for  $\text{SiO}^+$  molecule. The P ( $J \rightarrow J - 1$  transitions), and R-branched ( $J \rightarrow J + 1$  for the  $\text{SiO}^+$  molecule) are well separated. Number of populated rotational states in a molecule can be reduced using optical pumping with spectrally filtered broadband light that excites  $J \rightarrow J - 1$ , but not  $J \rightarrow J + 1$ ).

in [82]. For the  $X^2\Sigma^+(\nu = 0) \rightarrow B^2\Sigma^+(\nu = 0)$  transition in  $\text{SiO}^+$ , the  $R$  ( $J \rightarrow J + 1$  transitions) and  $P$  ( $J \rightarrow J - 1$  transitions) branches are well separated (see Fig. 3.3). Light with intensity  $dI/d\lambda = 1\text{mW/nm}$  can be produced by a gas discharge lamp or a femtosecond pulsed laser, and spectral filtering with a resolution better than 0.2 nm is achievable with a diffraction grating. Focusing this light into a 50  $\mu\text{m}$  spot provides a scattering rate of about  $10^5$  photons per second. This scattering rate can decrease the number of populated rotational states to less than 10 in about a millisecond for final preparation of states with quantum logic schemes.

For a realistic average intensity of the modelocked pulsed laser at the ion position of about  $1000\text{ W/cm}^2$ , laser detuning  $\Delta/2\pi = 20\text{ THz}$ , lifetime of  $B^2\Sigma^+$  excited state  $1/\gamma = 70\text{ ns}$ , and saturation intensity of the molecular transition  $I_{\text{sat}} = 45\text{ W/m}^2$  one can expect the time averaged Rabi frequency (3.2) on the carrier transition to be  $\Omega_0/2\pi = 0.2\text{ MHz}$ . For a Lamb-Dicke parameter  $\eta = 0.1$ , the duration of the  $\pi$  pulse on a sideband transition of a molecule is about  $100\ \mu\text{s}$ . The sideband cooling step should have a comparable duration. Assuming that the rotational population is distributed among the 10 lowest  $J$  states, and that it takes about 10 cycles to bring the population from  $J$  to  $J - 2$  level, we estimate the total cooling time to be on the order of 20 ms which is much faster than the  $\sim 20\text{ s}$  achievable by alternative schemes that rely on blackbody radiation for repumping between rotational states [127; 137].

Spontaneous emission will likely remove the molecule out of the cooling cycle and leave it in a different rotational, or even different vibrational state. Assuming that the bandwidth of the mode locked pulsed laser  $\sim 1/\tau \ll \Delta$  the rate of spontaneous emission can be estimated as  $R_s = 2\gamma\Omega/\Delta = 0.3\text{ s}^{-1}$ , much slower than the duration of the cooling sequence.

Another mechanism lowering the efficiency of the cooling protocol is the accidental coincidence between the Raman sideband transition from the  $J$  to  $J - 2$  state and the  $J - 1 \rightarrow J + 1$  transition that can populate angular momentum levels that have already been depopulated. However the probability of this coincidence, assuming only  $N_J = 10$  lowest rotational levels are populated, is relatively low:

$$p \sim 4N_J\Omega_0/(2\pi f_{rep}) \simeq 0.1,$$

where  $f_{rep} \simeq 80\text{MHz}$  is a typical repetition rate of a modelocked pulsed laser. This coincidence can be avoided by the proper choice of the laser repetition rate or a decrease in the Raman laser power.

The accidental coincidence between different transitions driven by a frequency comb can also present a problem during state detection. However, one can always optimize the repetition rate of the pulse laser to avoid this coincidence for the particular state. Another problem that can limit a state detection fidelity is a non-perfect sideband cooling, or the ion heating during the experimental sequence, which introduces an error during the coupling of internal and motional states. Nevertheless, at the end of the protocol, the molecule is left in one of two known rotational states and, similar to [120; 126], the state detection protocol can be repeated several times to improve the fidelity.

# Chapter 4

## Zeeman-splitting-assisted quantum-logic spectroscopy of trapped ions

In this chapter, we will first describe the proposal and experimental demonstration using two atomic ions a state detection technique employing state-dependent magnetic  $g$ -factors, which in turn show distinct Zeeman splittings. It is then followed by our current progress towards the implementation of this scheme to the molecular ion  $\text{SiO}^+$ . Such “Zeeman-splitting-assisted quantum logic spectroscopy” (ZS-QLS) uses lasers far-detuned from one-photon transitions to drive Raman transitions between Zeeman sublevels, hence does not require any scattering from the spectroscopy ion. Being a Raman version of the original implementation of QLS [126], ZS-QLS uses long-lived Zeeman sublevels instead of a metastable electronic excited state. Nevertheless, ZS-QLS as a state detection method can be combined with other techniques (e.g. laser excitation) to perform spectroscopy in the optical domain.

## 4.1 Model

To implement ZS-QLS, one begins with a Doppler-cooled logic ion (L) that sympathetically cools a spectroscopy ion (S). Together, they form a two-ion crystal and share common modes of motion. The motional modes along one direction are cooled to the ground state of motion by sideband cooling the logic ion.

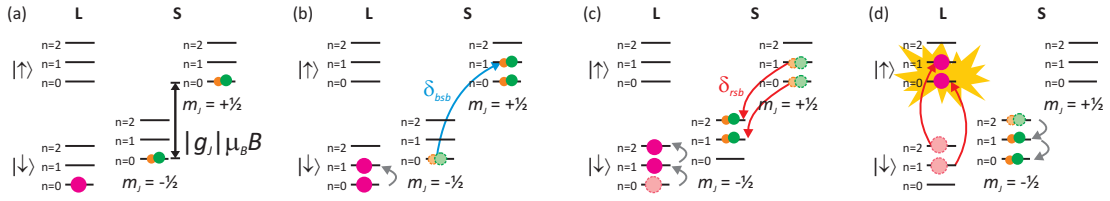


Figure 4.1: Schematic of Zeeman-splitting quantum logic spectroscopy for  $g_J < 0$ . (a) Both the logic ion (L) and its co-trapped spectroscopy ion (S) are sideband-cooled to the ground motional state. To probe if the spectroscopy ion is in the  $J = 1/2$  state regardless of its distribution amongst the Zeeman sublevels, (b) a blue sideband of the Zeeman transition is applied, followed by (c) the corresponding red sideband. A mixture of one and two phonons can then be excited. (d) The presence of phonons is detected by driving the red sideband of the logic qubit transition  $| \downarrow \rangle \rightarrow | \uparrow \rangle$  and measuring the logic ion fluorescence.

To probe the Zeeman splitting of the spectroscopy ion in a state of angular momentum  $J$  and magnetic g-factor  $g_J < 0$ , a pair of Raman lasers are applied such that their frequency difference  $\delta_{\text{bsb}}$  is blue detuned by one normal mode frequency  $\omega_n$  from the Zeeman splitting  $|g_J| \mu_B B$  ( $\mu_B$  is the Bohr magneton) (Fig. 4.1b). For an ion initialized in the state  $|J, m_J\rangle$  where the magnetic quantum number  $m_J$  is less than  $J$ , a phonon will be added to the motion of the ion crystal with high probability. However, if the spectroscopy ion is initially in the state  $|J, m_J = J\rangle$ , the blue-sideband pulse would not have added any phonons. One therefore needs to apply a red-sideband Raman pulse  $\delta_{\text{rsb}}$  to add any phonons (Fig. 4.1c)<sup>1</sup>. Applying the blue and red sideband pulses sequentially ensures

<sup>1</sup> For an ion driven to the  $|J, m_J + 1\rangle$  state after the first Zeeman blue-sideband pulse, the

that phonons can be excited regardless of the probability distribution between the Zeeman sublevels. ZS-QLS can also be applied to states of  $g_J > 0$ , in which case the first Zeeman blue-sideband pulse addresses all states  $|J, m_J > -J\rangle$  and the red-sideband pulse ensures that  $|J, m_J = -J\rangle$  is addressed.

Finally, the presence of phonons are detected with the logic ion, which fluoresces brightly when its internal state is successfully flipped upon driving the red motional sideband of the logic qubit transition (Fig. 4.1d). Since the red-sideband Rabi frequencies for one- and two-phonon states are different (see Eqn. 2.55), one has to choose a pulse time that maximizes the overall detection probability.

If the two-photon Raman detuning is far from the Zeeman splitting of the chosen state, no phonons are added and the logic ion remains dark. Likewise, if the spectroscopy ion resides in a state of different magnetic  $g$ -factor from the chosen two-photon Raman transition, the logic ion also remains dark.

The suitability of ZS-QLS for a given atomic or molecular species depends on three main factors: I. the lifetime of the state whose Zeeman splitting is being probed must be long enough to resolve the motional sidebands; II. the spectroscopy ion must have states of different magnetic  $g$ -factors; III. the Zeeman splitting between  $m_J$  sublevels in a given  $J$  state should not overlap with splittings from other  $J$  states. Given that a large class of molecular ions possess rotational states that are relatively long-lived (satisfying I) and have different  $g$ -factors (satisfying II), we now examine the applicability of ZS-QLS to molecular ions in greater detail.

In molecular ions, the magnetic  $g$ -factor comes from three contributions: the electron (spin and orbital) angular momentum, nuclei spin, and molecule rotation.

---

subsequent red-sideband pulse can drive the ion to the  $|J, m_J + 2\rangle$  (if available) or  $|J, m_J\rangle$  state, thereby removing or adding another phonon. Nevertheless, the combined action of the Zeeman blue and red sideband pulses serves to excite a phonon with high probability.

The second and third contributions are small (on the order of  $1/1840$  compared to the first contribution). In the absence of hyperfine splitting, we can focus on the first contribution.

For states of Hund's coupling case (a), the dependence of  $g_J$  on the rotational level  $J$  goes as [51]

$$g_J = \frac{(\Lambda + 2\Sigma)(\Lambda + \Sigma)}{J(J + 1)}, \quad (4.1)$$

where  $\Lambda$  and  $\Sigma$  are projections of the electron orbital and spin angular momentum on the molecular axis, respectively. While  $g_J = 0$  for  ${}^2\Pi_{1/2}$  states, the numerator of  $g_J$  from Eq. (4.1) is 1 for  ${}^1\Pi$  and 2 for  ${}^2\Pi_{3/2}$ , respectively. The  $J$ -dependence of  $g_J$  does not rely on the presence of any particular molecular transitions or spectroscopic constants such as diagonal Franck-Condon overlaps, therefore any molecule with a low-lying case (a)  ${}^1\Pi$  or  ${}^2\Pi_{3/2}$  state such as  $\text{O}_2^+$  and  $\text{SO}^+$  can be detected with ZS-QLS. Further, quadratic Zeeman shifts are expected to be small for reasonable table-top magnetic fields ( $< 200$  Hz for  $5$  G), satisfying constraint III for ZS-QLS.

For states described by Hund's coupling case (b), the magnetic  $g$ -factor in the weak magnetic field is [51]

$$g_{JNS} = \Lambda^2 \frac{J(J + 1) + N(N + 1) - S(S + 1)}{2J(J + 1)N(N + 1)} + \frac{J(J + 1) + S(S + 1) - N(N + 1)}{J(J + 1)}, \quad (4.2)$$

where  $S$  is the electron spin quantum number and  $N = J - S$ . In the strong-field regime, however, the coupling between  $S$  and  $N$  are weaker than their individual couplings to the applied magnetic field, thus the magnetic  $g$ -factor is split into

two components:

$$g_N = \frac{\Lambda^2}{N(N+1)}; \quad g_S = 2. \quad (4.3)$$

For the  $^1\Sigma$  state, the magnetic  $g$ -factor is 0, so the state cannot be detected using ZS-QLS. For the  $^2\Sigma$  state,  $\Lambda = 0$ , leaving only the second term in Eq. (4.2). One must therefore be careful to avoid the strong-field regime, where the  $g$ -factor loses its dependence on the rotational quantum number. Further, in molecular ions like  $\text{CO}^+$  and  $\text{SiO}^+$  where  $^2\Sigma$  is the ground state, requirement III is fulfilled only in weak magnetic fields ( $B \lesssim 2 \text{ G}$  for  $\text{SiO}^+$  [128]). For stronger magnetic fields, the quadratic Zeeman shift for low-lying rotational levels can be significant compared to the difference in Zeeman splittings between adjacent rotational levels. One exception is the  $J = 1/2$  state: only comprising two Zeeman sub-levels, it has no quadratic shift and  $g_J = g_S = 2$ . ZS-QLS can then be applied up to stronger magnetic fields ( $B \lesssim 20 \text{ G}$  for  $\text{SiO}^+$ ), as long as other rotational states are not in the strong-field regime and possess the same magnetic  $g$ -factor (Eq. (4.3)).

## 4.2 Proof-of-principle experiment

To demonstrate the feasibility of ZS-QLS for state detection, we implemented the proposed scheme with  $^{171}\text{Yb}^+$  as the logic ion and  $^{174}\text{Yb}^+$  as the spectroscopy ion. In  $^{171}\text{Yb}^+$ , states  $|\downarrow\rangle \equiv |^2S_{1/2}, F=0, m_F=0\rangle$  and  $|\uparrow\rangle \equiv |^2S_{1/2}, F=1, m_F=0\rangle$  are chosen as qubit states [108]. In  $^{174}\text{Yb}^+$ ,  $|g_J| = 2$  for the ground state.

Both ions are trapped in the trap with secular trap frequencies  $(\omega_x, \omega_y, \omega_z) = 2\pi \times (0.91, 0.97, 0.79) \text{ MHz}$  for a single  $^{171}\text{Yb}^+$  ion. We load an ion crystal consisting of a single  $^{171}\text{Yb}^+$  and a single  $^{174}\text{Yb}^+$  by performing the isotope-selective

resonance-enhanced two-photon ionization on Yb atoms emitted from an oven, as described in Chapter 2. The 369.53 nm and 935.19 nm lasers are tuned to Doppler cool the  $^{171}\text{Yb}^+$ . Since the 369.53 nm and 935.19 nm lasers are 2.4 GHz and 2.7 GHz red-detuned from their respective transitions in  $^{174}\text{Yb}^+$ , the  $^{174}\text{Yb}^+$  ion is not efficiently Doppler-cooled and is instead sympathetically cooled by the  $^{171}\text{Yb}^+$  ion. These two ions are displaced along the  $\hat{z}$  direction and share the axial in-phase and out-of-phase normal modes of motion with frequencies  $(\omega_{ip}, \omega_{op}) = 2\pi \times (0.78, 1.37)$  MHz.

The mode-locked Ti:Sapphire laser used to produce Raman lasers for motional state control in this experiment is tuned to 377.2 nm. The two Raman beams are sent from orthogonal directions and interfere at the trap center to form a running-wave optical lattice along  $\hat{z}$ . Depending on the frequency difference between the two AOMs, the Raman lasers can drive the qubit carrier transition in  $^{171}\text{Yb}^+$ , its motional sidebands, or the  $^{174}\text{Yb}^+$  Zeeman sublevel motional sidebands. The use of a frequency comb provides the added advantage of being able to drive all the above Raman transitions with a single laser [47]. The polarizations of the Raman lasers are set to be linear and oriented such that all three components  $\pi, \sigma^+, \sigma^-$  relative to the quantization axis are present. This allows us to drive the  $\Delta m_J = 0$  qubit transition for efficient sideband cooling as well as the  $\Delta m_J = \pm 1$  transitions in  $^{174}\text{Yb}^+$ .

To begin ZS-QLS, the Raman lasers are tuned to the in-phase and out-of-phase normal mode red sidebands of the  $^{171}\text{Yb}^+$  qubit transition for sideband cooling. One hundred sideband-cooling cycles are applied, leaving the two-ion crystal with an average phonon number of  $\bar{n} = 0.029(15)$  for the out-of-phase normal mode. With  $^{171}\text{Yb}^+$  initialized in  $|\downarrow\rangle$  [108], the Raman lasers then apply a blue-sideband pulse ( $\delta_{\text{bsb}} = |g_J|\mu_B B + \omega_{op}$ ) followed by a red-sideband pulse

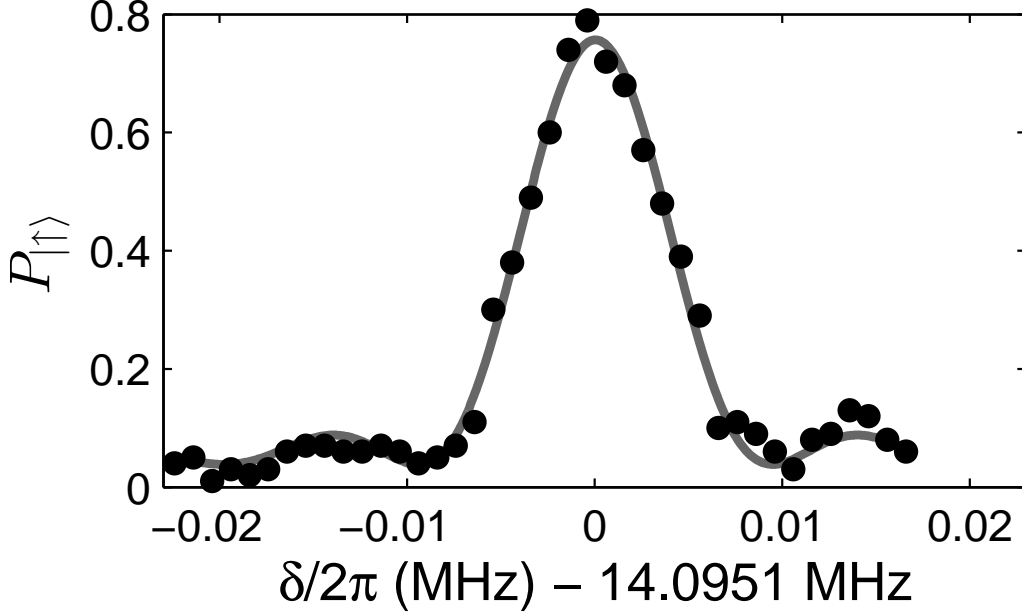


Figure 4.2: Probability of  $^{171}\text{Yb}^+$  occupying the bright  $|\uparrow\rangle$  state as a function of the average Raman laser detuning from the  $^2S_{1/2}$  Zeeman splitting in  $^{174}\text{Yb}^+$ .

( $\delta_{\text{rsb}} = |g_J|\mu_B B - \omega_{op}$ ), each of  $\pi$ -pulse time  $100 \mu\text{s}$ . Here, the magnetic field  $B = 5.0 \text{ G}$  is applied at  $45^\circ$  from  $\hat{z}$ . The out-of-phase normal mode is chosen because it exhibits a low heating rate of  $2.9(4)$  phonons/s. Finally, the presence of phonons is detected by tuning the Raman laser to the red sideband of the  $^{171}\text{Yb}^+$  qubit transition and applying the standard state detection technique to the logic ion [108]. Figure 4.2 shows a scan of the Raman laser detuning about the Zeeman splitting. The frequency difference between the two Raman pulses is fixed to be  $2\omega_{op}$  while the average frequency  $\delta$  is varied. The spectrum is fit to a Rabi lineshape with a peak position at  $|g_J|\mu_B B = 14.0951(1) \text{ MHz}$ . The inferred  $|g_J|$  of 2 is consistent with the  $^{174}\text{Yb}^+$  ion occupying its ground electronic state.

The initial population distribution between the two  $|m_J\rangle$  sublevels can also be mapped onto the probabilities of populating one phonon versus two phonons. The Rabi oscillations detected on the qubit red sideband are then a superposition

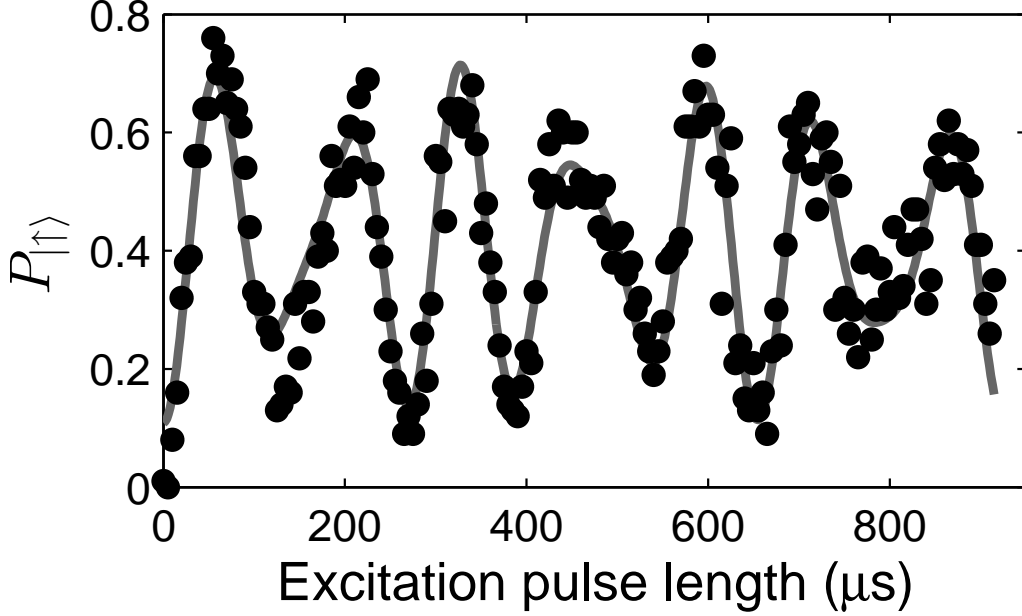


Figure 4.3: Probability of  $^{171}\text{Yb}^+$  occupying the bright  $|\uparrow\rangle$  state after applying the Zeeman blue and red sidebands, as a function of the  $^{171}\text{Yb}^+$  qubit red sideband pulse duration. The data is fit to a sum of Rabi oscillations arising from one phonon and two phonons that are populated with the probabilities 0.70(3) and 0.30(3), respectively.

of those with Rabi frequencies  $\Omega\eta$  and  $\Omega\eta\sqrt{2}$  respectively (see Eqn. 2.55), where  $\Omega/(2\pi) = 50.67(7)$  kHz refers to the qubit carrier Rabi frequency and  $\eta = 0.15$  is the Lamb-Dicke parameter. The pulse durations of both the Zeeman blue and red sidebands are set to be  $\pi/(\Omega\eta)$ . Hence, the probability of exciting a second phonon given one phonon already being present is  $p_- \sin^2(\sqrt{2}\pi/2)$ , where  $p_-$  is the initial probability of occupying the  $|m_J = -1/2\rangle$  state. The probability of exciting only one phonon in the Zeeman scheme is  $p_-(1 - \sin^2(\sqrt{2}\pi/2)) + p_+$ , where  $p_+$  is the initial probability of occupying the the  $|m_J = +1/2\rangle$  state. Figure 4.3 shows a scan of the pulse duration of the qubit red sideband. According to the fit, the two-phonon and one-phonon modes are populated with probabilities 0.30(3) and 0.70(3). One can therefore infer the initial probabilities  $p_-$  and  $p_+$  to be

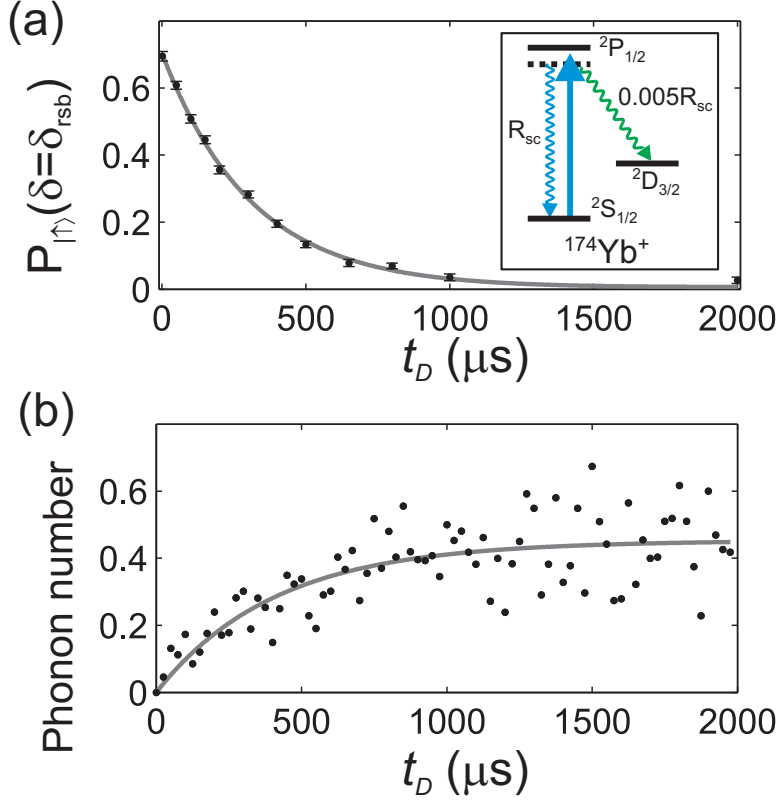


Figure 4.4: Optical pumping of  $^{174}\text{Yb}^+$  into the  $^2D_{3/2}$  state. (a) The loss of population in the  $^2S_{1/2}$  state can be probed by measuring the on-resonance probability of the logic ion in the bright state  $P_{|\uparrow\rangle}(\delta = \delta_{rsb})$  as a function of the  $^2D_{3/2}$  state optical pumping time  $t_D$ . The data is fit to an exponential decay with a decay time constant of  $312(8) \mu\text{s}$ . (Inset) Energy levels and branching ratios in  $^{174}\text{Yb}^+$ . (b) Phonon number versus optical pumping time  $t_D$  for the out-of-phase normal mode. The data is fit to the functional form  $n = n_0(1 - e^{-t_D/\tau})$ .

0.47(5) and 0.53(4), respectively, in accordance with the fact that no particular state preparation of  $^{174}\text{Yb}^+$  was carried out.

Besides populating the ground state, the  $^{174}\text{Yb}^+$  ion can be optically pumped into its metastable  $^2D_{3/2}$  state where  $|g_J| \neq 2$ , by tuning the 935 nm repumper laser far off resonance while scattering off a 369 nm laser detuned 300 MHz from its  $^2S_{1/2} - ^2P_{1/2}$  transition. The branching ratio for decay from the  $^2P_{1/2}$  state is 1:0.005 (Fig. 4.4 (a) inset) [108]. The  $^2D_{3/2}$  optical pumping sequence is

followed by at least two cycles of sideband cooling to remove phonons added from photon-recoil heating, so that the ions remain in the motional ground state before applying the Zeeman sideband pulses. We then take the height of the peak as recorded in Fig. 4.2 for different optical pumping times  $t_D$ . Figure 4.4 (a) shows an exponential decay with a fit time constant of  $312(8) \mu\text{s}$ , which corresponds to a decay of the  $^2S_{1/2}$  population as the  $^{174}\text{Yb}^+$  probability of occupying the  $^2D_{3/2}$  state increases. The natural lifetime of the  $^2D_{3/2}$  state is 52.7 ms and exerts a negligible effect on the measured decay.

As a check on the  $^2D_{3/2}$  state pumping of  $^{174}\text{Yb}^+$ , we measure the photon-recoil heating induced by the 369 nm optical pumping laser on the two-ion crystal. We also start with the ions sideband-cooled to the motional ground state. Photon recoil of the  $^{174}\text{Yb}^+$  ion adds phonons, which are detected by comparing the ratios of the blue to red sideband amplitudes of the qubit transition [147]. The phonon number eventually saturates when the  $^{174}\text{Yb}^+$  ion is pumped into the  $^2D_{3/2}$  state. The time constant for optical pumping as measured with the out-of-phase normal mode sidebands is  $400(60) \mu\text{s}$  (Fig. 4.4b), which agrees to within  $1.5 \sigma$  of the exponential decay time measured using ZS-QLS.

### 4.3 Sideband cooling of $\text{SiO}^+$ to the motional ground state

We have proposed and demonstrated a quantum logic scheme for detecting the states of dark ions based on the state-dependent magnetic  $g$ -factor. ZS-QLS is particularly well-suited for detecting rotational states in molecular ions. Given the lack of closed cycling transitions in molecular ions, existing popular methods

for rovibrational state detection include resonance-enhanced multiphoton dissociation [52; 105; 116; 121; 130] and laser-induced charge transfer [124; 141], both of which are destructive to the ion species. On the contrary, ZS-QLS is nondestructive, allowing for repetitive experiments with a single molecular ion that forms an ideal system for precision measurement.

The first step to implement this scheme is the sideband cooling of the ion crystal formed by an easily accessible atomic ion and a molecular ion ( $^{171}\text{Yb}^+$  and  $\text{SiO}^+$  in our case). In the proof-of-principle experiment with two different isotopes of  $\text{Yb}^+$  described previously, we know naturally what the spectroscopy ion is due to the isotope-selective loading. It is not so straightforward to determine what the molecular ion is in the trap given that it is produced by laser ablation, which also produces many other different ion species that may be loaded into the trap. The loading of the correct molecular ion is verified by mass spectroscopy, which exploits the dependence of the trapping frequency of the crystal on the mass of the dark ion.

### 4.3.1 Mass spectroscopy of the molecular ion

Following Chapter 2, we define the spring constants  $k_i$  to characterize the trap (harmonic) potential for a single trapped ion with mass  $m$ ,

$$k_i \equiv m\omega_i^2, \quad (4.4)$$

where  $i = x, y, z$  refer to three principal directions and  $\omega_i$  are the corresponding trapping frequencies. Adding more ions with different masses does not influence the trapping potential coming from the trap itself. From Eqn. 2.22 2.23 2.17 and 2.13, one can see that  $k_z$  is independent of the mass of the ion, while  $k_{x(y)}$  is not.

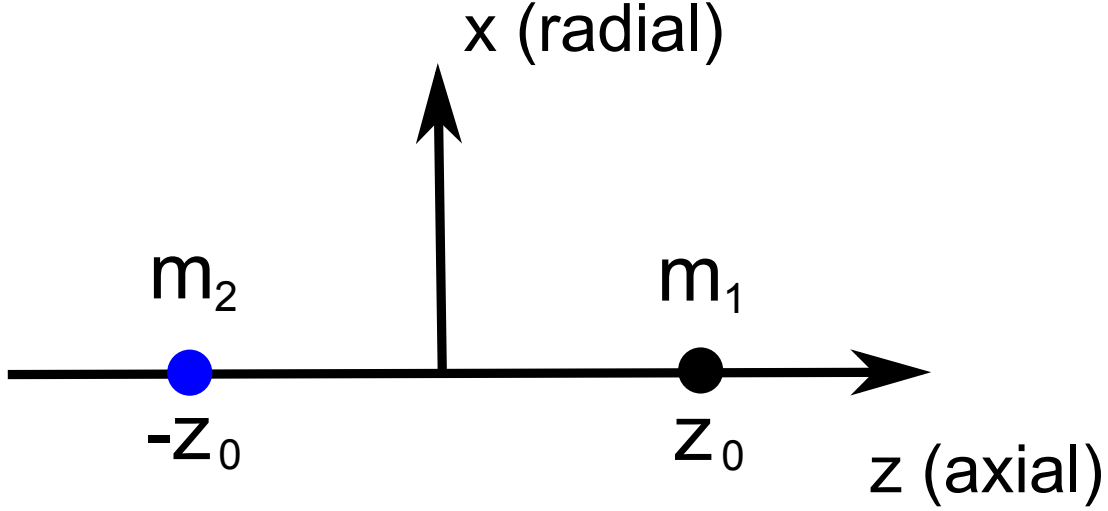


Figure 4.5: Two ions with mass  $m_1, m_2$  are confined in the same trap and  $2z_0$  is the distance between the ions at equilibrium.

We add one more subscript index to  $k_{x(y)}$  for the case with more than one ion in the trap to label the ions,

$$k_{x(y)j} \equiv m_j \omega_{x(y)j}^2, \quad (4.5)$$

Suppose that two ions with mass  $m_1, m_2$  are confined in the same trap and aligned along the axial direction (see Fig. 4.5). The center point of crystal is set to be the origin of our coordinate system. We consider  $x$  and  $z$  directions only to simplify the algebra. Formulas for  $y$  direction can be derived similarly. The kinetic and potential energy of the system are

$$T = \frac{1}{2}m_1\dot{z}_1^2 + \frac{1}{2}m_2\dot{z}_2^2 + \frac{1}{2}m_1\dot{x}_1^2 + \frac{1}{2}m_2\dot{x}_2^2, \quad (4.6)$$

$$V = \frac{1}{2}k_z Z_1^2 + \frac{1}{2}k_z Z_2^2 + \frac{1}{2}k_{x1}x_1^2 + \frac{1}{2}k_{x2}x_2^2 + \frac{e^2}{4\pi\epsilon_0} \frac{1}{\sqrt{(x_1 - x_2)^2 + (Z_1 - Z_2)^2}}. \quad (4.7)$$

where  $x_i, Z_i$  are coordinates of the ion  $i$  and  $\epsilon_0$  is the permittivity of vacuum.

By setting  $\partial V/\partial x_1 = 0$ ,  $\partial V/\partial x_2 = 0$ ,  $\partial V/\partial Z_1 = 0$  and  $\partial V/\partial Z_2 = 0$ , we obtain the equilibrium position  $x_1 = x_2 = 0$ ,  $Z_1 = z_0$  and  $Z_2 = -z_0$ , where  $z_0 = [e^2/(16\pi\epsilon_0 k_z)]^{1/3}$ . We define the deviation from the equilibrium position along the axial direction to be  $z_1 = Z_1 - z_0$  and  $z_2 = Z_2 + z_0$  for ion 1 and ion 2 and expand the potential energy at this position to the second order,

$$\begin{aligned} V &= k_z z_1^2 + k_z z_2^2 - k_z z_1 z_2 \\ &+ \frac{1}{2}(k_{x1} - \frac{k_z}{2})x_1^2 + \frac{1}{2}(k_{x2} - \frac{k_z}{2})x_2^2 + \frac{1}{2}k_z x_1 x_2. \end{aligned} \quad (4.8)$$

The Lagrangian of the system is,

$$\begin{aligned} \mathcal{L} &= T - V \\ &= \frac{1}{2}m_1 \dot{z}_1^2 + \frac{1}{2}m_2 \dot{z}_2^2 - (k_z z_1^2 + k_z z_2^2 - k_z z_1 z_2) + \frac{1}{2}m_1 \dot{x}_1^2 + \frac{1}{2}m_2 \dot{x}_2^2 \\ &\quad - \frac{1}{2} \left( (k_{x1} - \frac{k_z}{2})x_1^2 + (k_{x2} - \frac{k_z}{2})x_2^2 + k_z x_1 x_2 \right). \end{aligned} \quad (4.9)$$

By applying the Lagrange's equation,  $d(\partial\mathcal{L}/\partial\dot{x})/dt - \partial\mathcal{L}/\partial x = 0$ , to this Lagrangian, we obtain two sets of equations decoupled from each other,

$$\begin{cases} m_1 \ddot{z}_1 + 2k_z z_1 - k_z z_2 = 0 \\ m_2 \ddot{z}_2 + 2k_z z_2 - k_z z_1 = 0 \end{cases} \quad (4.10)$$

and

$$\begin{cases} m_1 \ddot{x}_1 + (k_{x1} - \frac{1}{2}k_z)x_1 + \frac{1}{2}k_z x_2 = 0 \\ m_2 \ddot{x}_2 + (k_{x2} - \frac{1}{2}k_z)x_2 + \frac{1}{2}k_z x_1 = 0. \end{cases} \quad (4.11)$$

Suppose the ions oscillate collectively along  $x$  ( $z$ ) direction with frequency  $\omega_x$

$(\omega_z)$  and amplitude of  $A_{xj}$  ( $A_{zj}$ ). By setting  $z_1 = A_{z1}e^{i\omega_z t}$ ,  $z_2 = A_{z2}e^{i\omega_z t}$  and  $x_1 = A_{x1}e^{i\omega_x t}$ ,  $x_2 = A_{x2}e^{i\omega_x t}$ , these two sets of equations are transformed into

$$\begin{cases} -m_1\omega_z^2 A_{z1} + 2k_z A_{z1} - k_z A_{z2} = 0 \\ -m_2\omega_z^2 A_{z2} + 2k_z A_{z2} - k_z A_{z1} = 0 \end{cases} \quad (4.12)$$

and

$$\begin{cases} -m_1\omega_x^2 A_{x1} + (k_{x1} - \frac{1}{2}k_z)A_{x1} + \frac{1}{2}k_z A_{x2} = 0 \\ -m_2\omega_x^2 A_{x2} + (k_{x2} - \frac{1}{2}k_z)A_{x2} + \frac{1}{2}k_z A_{x1} = 0 . \end{cases} \quad (4.13)$$

If the equations have nontrivial solutions for the oscillation amplitudes, the determinant of the corresponding matrices must be zero, i.e.

$$\begin{vmatrix} -m_1\omega_z^2 + 2k_z & -k_z \\ -k_z & -m_2\omega_z^2 + 2k_z \end{vmatrix} = 0 \quad (4.14)$$

and

$$\begin{vmatrix} -m_1\omega_x^2 + (k_{x1} - \frac{1}{2}k_z) & \frac{1}{2}k_z \\ \frac{1}{2}k_z & -m_2\omega_x^2 + (k_{x2} - \frac{1}{2}k_z) \end{vmatrix} = 0 . \quad (4.15)$$

The solutions to these equations are

$$\omega_{zip}^2 = \frac{(m_1 + m_2) - \sqrt{m_1^2 + m_2^2 - m_1 m_2}}{m_1 m_2} k_z , \quad (4.16)$$

$$\omega_{zop}^2 = \frac{(m_1 + m_2) + \sqrt{m_1^2 + m_2^2 - m_1 m_2}}{m_1 m_2} k_z , \quad (4.17)$$

and

$$\omega_{xip}^2 = \frac{(m_1(k_{x2} - \frac{1}{2}k_z) + m_2(k_{x1} - \frac{1}{2}k_z)) + \sqrt{(m_1(k_{x2} - \frac{1}{2}k_z) - m_2(k_{x1} - \frac{1}{2}k_z))^2 + m_1m_2k_z^2}}{2m_1m_2}, \quad (4.18)$$

$$\omega_{xop}^2 = \frac{(m_1(k_{x2} - \frac{1}{2}k_z) + m_2(k_{x1} - \frac{1}{2}k_z)) - \sqrt{(m_1(k_{x2} - \frac{1}{2}k_z) - m_2(k_{x1} - \frac{1}{2}k_z))^2 + m_1m_2k_z^2}}{2m_1m_2}, \quad (4.19)$$

where  $\omega_{xip}$  and  $\omega_{xop}$  ( $\omega_{zip}$  and  $\omega_{zop}$ ) are two possible solutions that describe the in-phase and out-of-phase motion of the crystal respectively along  $x$  ( $z$ ) direction. They are expressed as functions of the masses and spring constants of both ions.

When a single logic ion (assume its mass is  $m_1$ ) is trapped, its trapping frequencies can be measured. We can infer its spring constants according to 4.5. Since both ions share the same trap, from Eqn. 2.22 2.23 2.17 and 2.13, we derive the spring constants for the other ion,

$$k_{x2} = \frac{2k_{x1} + (1 - \mu)(1 - \alpha)k_{z1}}{2\mu}, \quad (4.20)$$

where  $\mu = m_2/m_1$  is the mass ratio. To simplify the algebra, we assume that the radial confinement is symmetric, i.e.  $\alpha = 0$ . Thus, the frequencies of the collective motion in the ion crystal can be expressed as functions of normal-mode frequencies of the logic ion and the mass ratio between these two ions. The final expressions are

$$\omega_{zip}^2 = \frac{(1 + \mu) - \sqrt{\mu^2 - \mu + 1}}{\mu} \omega_{z1}^2 \quad (4.21)$$

$$\omega_{zop}^2 = \frac{(1 + \mu) + \sqrt{\mu^2 - \mu + 1}}{\mu} \omega_{z1}^2 \quad (4.22)$$

and

$$\omega_{xip}^2 = \frac{\left(\frac{1+\mu^2}{\mu} \omega_{x1}^2 + \frac{1-2\mu-\mu^2}{2\mu} \omega_{z1}^2\right) + \sqrt{\left(\frac{1-\mu^2}{\mu} \omega_{x1}^2 + \frac{1-2\mu+\mu^2}{2\mu} \omega_{z1}^2\right)^2 + \mu \omega_{z1}^4}}{2\mu} \quad (4.23)$$

$$\omega_{xop}^2 = \frac{\left(\frac{1+\mu^2}{\mu} \omega_{x1}^2 + \frac{1-2\mu-\mu^2}{2\mu} \omega_{z1}^2\right) - \sqrt{\left(\frac{1-\mu^2}{\mu} \omega_{x1}^2 + \frac{1-2\mu+\mu^2}{2\mu} \omega_{z1}^2\right)^2 + \mu \omega_{z1}^4}}{2\mu} . \quad (4.24)$$

Given that the frequencies of collective modes can be measured experimentally, the formulas above offer a way to determine the mass of the dark spectroscopy ion.

Defining the ratio of oscillation amplitudes,  $R_z = A_{z2}/A_{z1}$  and  $R_x = A_{x2}/A_{x1}$ , from Eqn. 4.12 and 4.13, we obtain

$$R_{zip} = 2 - \frac{\omega_{zip}^2}{\omega_z^2} , \quad (4.25)$$

$$R_{zop} = 2 - \frac{\omega_{zop}^2}{\omega_z^2} , \quad (4.26)$$

$$R_{xip} = \frac{2\omega_{xip}^2 - 2\omega_{x1}^2 + \omega_{z1}^2}{\omega_{z1}^2} , \quad (4.27)$$

$$R_{xop} = \frac{2\omega_{xop}^2 - 2\omega_{x1}^2 + \omega_{z1}^2}{\omega_{z1}^2} . \quad (4.28)$$

These ratios are particularly important for the sympathetic cooling [57; 159].

For a special case  $\mu = 1$ , the frequencies of the collective modes and the ratios

of the oscillation amplitudes are

$$\omega_{zip} = \omega_{z1} \quad (4.29)$$

$$\omega_{zop} = \sqrt{3}\omega_{z1} \quad (4.30)$$

$$\omega_{xip} = \omega_{x1} \quad (4.31)$$

$$\omega_{xop} = \sqrt{\omega_{x1}^2 - \omega_{z1}^2} \quad (4.32)$$

and

$$R_{zip} = 1 \quad (4.33)$$

$$R_{zop} = -1 \quad (4.34)$$

$$R_{xip} = 1 \quad (4.35)$$

$$R_{xop} = -1. \quad (4.36)$$

### 4.3.2 Loading and sympathetic cooling of the $\text{SiO}^+$ ions

We developed two methods to load the  $\text{SiO}^+$  ions and both are based on the laser ablation of a SiO target. To prepare the SiO target, we mix the SiO powder with some distilled water on top of a microscope slide (5 mm  $\times$  15 mm). After the water evaporates, a layer (thickness  $\sim$  0.1 mm) of the SiO powder is stuck on the glass surface. This SiO target is mounted side by side with the Yb foil in the vacuum chamber as shown in Fig. 2.1. Similar to the loading of  $\text{Yb}^+$  ions, the loading of  $\text{SiO}^+$  ions are achieved either by capturing the  $\text{SiO}^+$  ions that are ionized during the ablation or by photoionizing the neutral SiO molecules (produced by the ablation) in the trap volume. In the former case, the same Q-switched Nd:YAG laser as used to load  $\text{Yb}^+$  ions is then focused on the SiO

target with a similar spot size ( $\sim 50\mu\text{m}$ ). The minimum single-pulse energy for the trap to capture the ions ranges from  $50\ \mu\text{J}$  to  $100\ \mu\text{J}$  depending on which part of the target the pulses ablate. In the latter case, the ablation is performed by a nitrogen laser (SRS NL100) at  $337\ \text{nm}$  while the aforementioned Nd:YAG laser serves as the photoionization laser. The photoionization laser is gated such that the pulses it produces reach the trap  $20\ \mu\text{s}$  later than the pulses from ablation laser. This delay is experimentally determined to account for the time of flight between the SiO target and the trap center. The neutral SiO molecules can be photoionized by a multiphoton process with a single pulse (pulse energy  $3\ \text{mJ}$  and diameter  $30\ \mu\text{m}$ ). The numbers of the captured  $\text{SiO}^+$  ions in both cases are roughly controlled by the single-pulse energies of the ablation pulses and the presence of a single  $\text{SiO}^+$  ion in the trap is further verified with the camera after it is crystallized with a single  $\text{Yb}^+$  ion.

A single  $^{171}\text{Yb}^+$  ion is trapped to sympathetically cool the  $\text{SiO}^+$  ion. Due to the large mass difference (mass ratio  $\mu = 0.26$ ) between these two ions, the sympathetic cooling does not work efficiently [57; 159]. The cooling rate of a certain motional mode is proportional to the square of the corresponding oscillation amplitude of the cooling ion [159]. Thus, it is substantially determined by the ratio of oscillation amplitudes given a certain amount of energy in this mode. The ratios of axial oscillation amplitudes are determined by the mass ratio only. For a  $^{171}\text{Yb}^+$ - $\text{SiO}^+$  crystal,  $R_{zip} = 0.6$  and  $R_{zop} = -6.4$  according to Eqn 4.25 and Eqn 4.25. On the other hand, the ratios of radial oscillation amplitudes depend on both the mass ratio  $\mu$  and the trapping frequencies. For the axial confinement of  $\omega_1 = 2\pi \times 800\ \text{kHz}$ , we plot the  $R_{xip}$  and  $R_{xop}$  as functions of radial confinement  $\omega_{x1}$ , as shown in Fig. 6.9. One can see that the axial in-phase mode and radial out-of-phase mode can be cooled well while the axial out-of-phase mode and radial

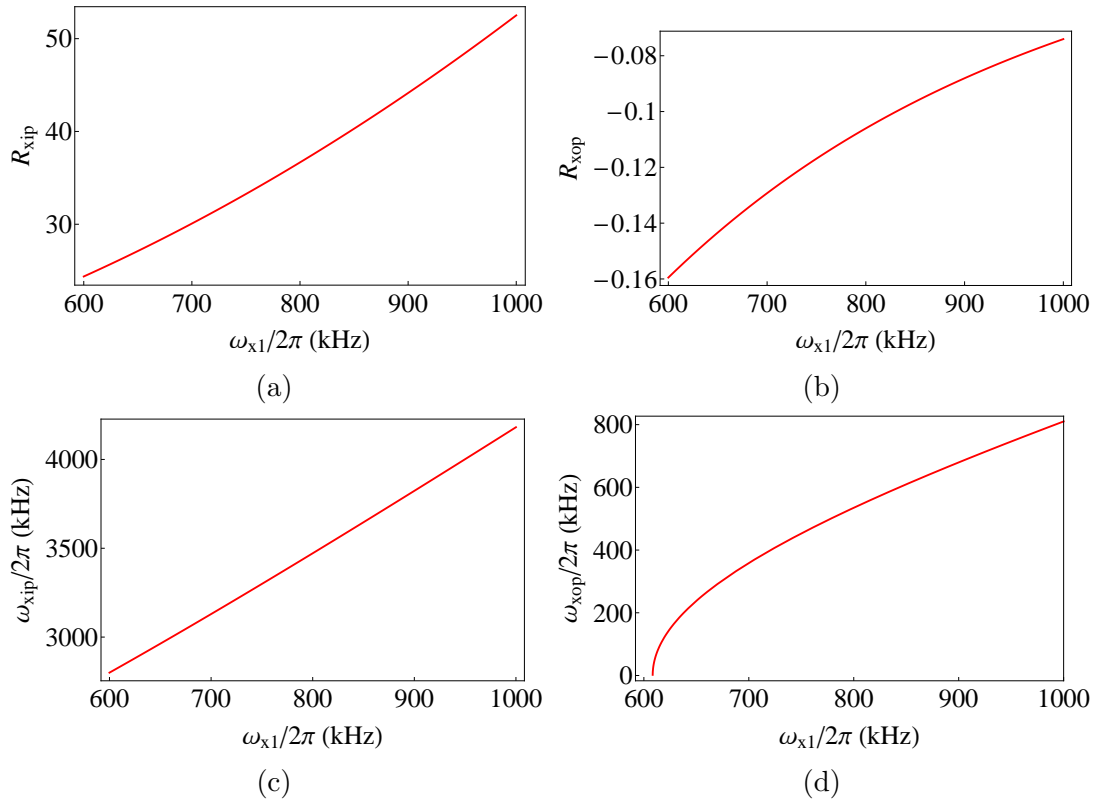


Figure 4.6: The ratios of oscillation amplitudes  $R_{xip}$  (a),  $R_{xop}$  (b) and the frequencies of collective motional modes  $\omega_{xip}$  (c),  $\omega_{xop}$  (d) as functions of a single  $^{171}\text{Yb}^+$  ion trapping frequency  $\omega_{x1}$ . We assume a symmetric radial confinement, i.e.  $\omega_{x1} = \omega_{y1}$ .

in-phase mode limit the cooling of the crystal <sup>1</sup>. It is experimentally found that a single  $^{174}\text{Yb}^+$  ion is capable of sympathetically cooling a single  $\text{SiO}^+$  ion that is initially hot to form a two-ion crystal along the axial direction while the  $^{171}\text{Yb}^+$  ion is not due to its lower photon-scattering rate, i.e. less efficient Doppler cooling <sup>2</sup>. However,  $\text{SiO}^+-^{171}\text{Yb}^+$  ions can be crystallized by Doppler cooling if the radial confinement is relaxed to the extent that the crystal is aligned along the radial direction. Doppler cooling is achieved by sending three cooling beams with tens of microwatt in each beam (focused on the ions with diameters of around  $30\ \mu\text{m}$ ) from different directions with different detunings ( $-50\ \text{MHz}$ ,  $-200\ \text{MHz}$  and  $-500\ \text{MHz}$ ) with respect to the resonant transition. After the ions are crystallized, as observed from the camera, we increase the radial confinement above the threshold of radial-axial transition by increasing the rf power sent to the trap resonator. The trap is operated close to the threshold to have a relatively small  $R_{xip}$  to enhance the cooling rate of the corresponding mode. In the experiments presented here, the trap frequencies are  $(\omega_x, \omega_y, \omega_z)=2\pi \times (770\ \text{kHz}, 830\ \text{kHz}, 800\ \text{kHz})$  for a single  $^{171}\text{Yb}^+$  ion.

Before any loading of the  $\text{SiO}^+$  ions, a single trapped  $^{171}\text{Yb}^+$  ion is Doppler cooled with three cooling beams and monitored with the camera. After a single  $\text{SiO}^+$  ion is loaded into the trap, usually we can not confirm its presence with the camera immediately. It typically takes one minute before it shows itself by colliding with the  $^{171}\text{Yb}^+$  ion and transforming a bright well-localized spot on the camera into a fuzzy cloud centered in the trap center with diameter of around

---

<sup>1</sup>The axial motion and radial motion behave in different ways because they possess different dependence on the masses of the ions.

<sup>2</sup>Doppler cooling of  $^{171}\text{Yb}^+$  ions is performed by driving  $^2\text{S}_{1/2} |F=1\rangle \rightarrow ^2\text{P}_{1/2} |F=0\rangle$  transition. Less photons are scattered owing to the existence of three Zeeman sublevels in the  $^2\text{S}_{1/2} |F=1\rangle$  state, which form a dark state that is destabilized by applying an external magnetic field [5].

10  $\mu\text{m}$ . The time scale we observe here is consistent with the recently reported result on sympathetic cooling of the hot ions from Roos's group [41]. If more than one hot ion is loaded, similar to the  $\text{Yb}^+$  ion, we apply the trap “off-on” techniques to select a single  $\text{SiO}^+$  ion. The off-time interval is carefully chosen such that the probability to lose the  $\text{SiO}^+$  ion when only one  $\text{SiO}^+$  ion is present in one off-on cycle is small but the  $\text{SiO}^+$  ion still can escape from the trap after many cycles (typically tens of cycles). The off-on cycles are repeated until the crystallization occurs after the radial confinement is lowered to a certain extent, which is determined experimentally.

An additional benefit is gained since the probability to lose a certain ion is higher if more ions are partially localized (fuzzy cloud). The off-on cycle may dump the extra  $\text{SiO}^+$  ions relatively more efficiently. However, if too many hot ions are partially localized, the off-on technique does not work since the probability for the  $^{171}\text{Yb}^+$  ion to stay till the end of the off-on cycles is statistically small. This probability is further degraded by the fact that the  $^{171}\text{Yb}^+$  ion is also relatively more delocalized due to the higher temperature, which in turn increases its probability to escape from the trap during one off-on cycle.

To prevent, as much as we can, this from happening, we always apply a few off-on cycles immediately after we see the transformation of the well-localized spot to a fuzzy cloud <sup>1</sup>. This is assisted by the fact that the time scale of the sympathetic cooling of the hot ions is slower than people's reaction time. It means that when those off-on cycles are applied, some of the hot ions may be still very delocalized and thus have a relative high probability to escape from the trap. Note that the off-on technique does not work either if so many hot ions are captured that the presence of these hot ions may heat the  $^{171}\text{Yb}^+$  ion immediately

---

<sup>1</sup>Having a graduate student that can react as fast as Lionel Messi actually may help.

to the extent that we can not see any scattering from the ion with the camera.

When the crystal is aligned along the axial direction, it melts typically in every two minutes or so and it may happen during the data taking. We automate the crystalization process by monitoring the scattering rate collected from the  $^{171}\text{Yb}^+$  ion with the PMT during the Doppler cooling in the experimental sequence and use it as the feedback to control the variable attenuator that in turn controls the rf power sent to the trap.

We emphasize that some of the description above is qualitative and selecting a hot ion produced from ablation is not deterministic. Better understanding of the dynamics of sympathetic cooling of the hot ions, especially in the case with very different masses, and quantitative calibration of off-on technique are desirable. Nevertheless, given the very long trapping time of the ions ( $\sim 5$  hours), the time devoted to the loading of a single molecular ion ( $\sim 20$  min) is worthwhile.

### 4.3.3 Cooling of a single $\text{SiO}^+$ ion to motional ground state

Once these two ions are crystallized and aligned along the axial direction, we measure the frequencies of both axial in-phase mode and axial out-of-phase mode for mass spectroscopy by measuring the corresponding sideband frequencies. We mitigate the influence of the AC Stark shift of the sidebands from the off-resonant coupling to the carrier transition by attenuating the power of the Raman pulses. The uncertainty of the measurement of the dark ion's mass, which is around 1 AMU, mainly comes from the drift of the axial trapping frequency since axial confinement in our trap is coupled to the radial confinement, which is not stable

due to fluctuation of rf power coupled to the trap<sup>1</sup>. Around 40% of the captured dark ions using photoionization loading method have the mass of either 44AMU or 45 AMU.

For sideband cooling of the single molecular ion, we first apply 0.1 ms of Doppler cooling of the  $^{171}\text{Yb}^+$  ion with three cooling beams followed by 3 ms of typical Doppler cooling described in Chapter 2. Raman pulses for the first order red sidebands of both axial in-phase mode and axial out-of-phase mode are applied alternately and repeated for 100 times. As in Chapter 2, the duration of the Raman pulse is varied with each Raman pulse followed by the state reinitializaion. The corresponding red and blue sidebands of axial in-phase mode and axial out-of-phase mode before and after sideband cooling are shown in Fig. 4.7. The red sidebands after sideband cooling in both modes are mostly diminished, indicating a very high population of the motional ground state.

## 4.4 Conclusion and outlook

In this chapter and the previous chapter, we propose methods to prepare, detect and manipulate the internal states of the molecular ion with quantum logic schemes. These approaches are general and they do not impose restrictive requirements on molecular structure, and can be applied to a wide range of molecular ions.

A method to load a single molecular ion is presented together with the sideband cooling of the its motional state. This paves the way for the experimental realization of the proposals described previously. It can open the way to control

---

<sup>1</sup>The radial confinement is actively stabilized in the experiments presented in Chapter 6, but not in this experiment.

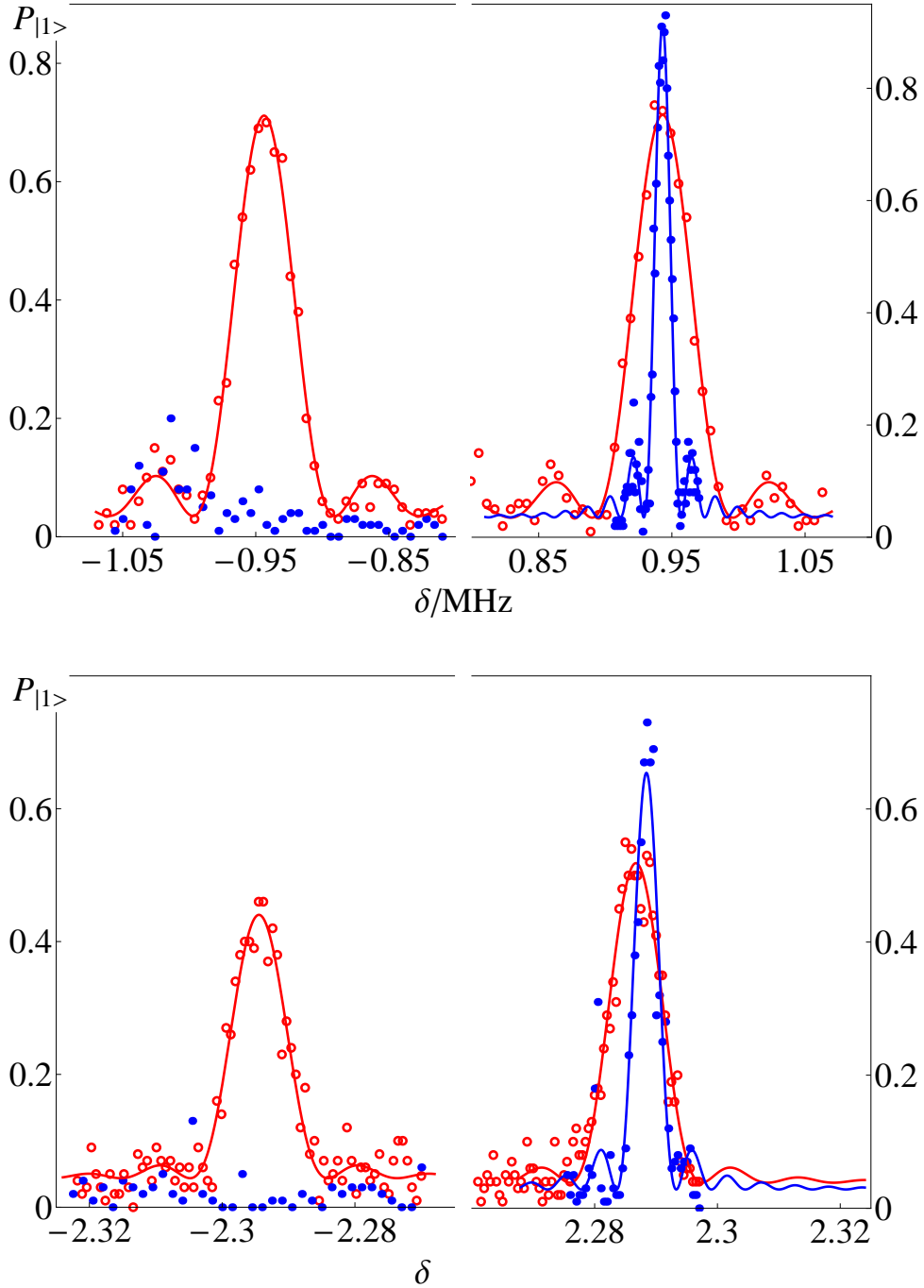


Figure 4.7: Raman sideband cooling of a single molecular ion to the motional ground state. The upper figure shows the red sideband and blue sideband of axial in-phase mode before (red circles) and after (blue dots) sideband cooling. Similarly, the lower figure shows the red sideband and blue sideband of axial out-of-phase mode before (red circles) and after (blue dots) sideband cooling.

quantum states of molecular ions and find applications in precision measurements, quantum information, and quantum chemistry.

# Chapter 5

## Microwave control of trapped-ion motion assisted by a running optical lattice

In this chapter, we describe the experimental demonstration of microwave coupling between the internal and motional states of a trapped  $^{171}\text{Yb}^+$  ion placed in a running spin-dependent optical lattice. We use this coupling to achieve resolved sideband cooling of a single trapped ion to the ground state of motion. Use of the running optical lattice eliminates the requirement for interferometric stability during the entire experiment (several hours). Instead, the relative phase between two optical beams should be stable for the duration of a single experimental cycle only (less than 1 ms), a requirement that is much easier to satisfy in the laboratory. In addition, driving internal transitions separated by 12.6 GHz directly with microwaves as opposed to Raman lasers removes the need for high frequency optical modulators.

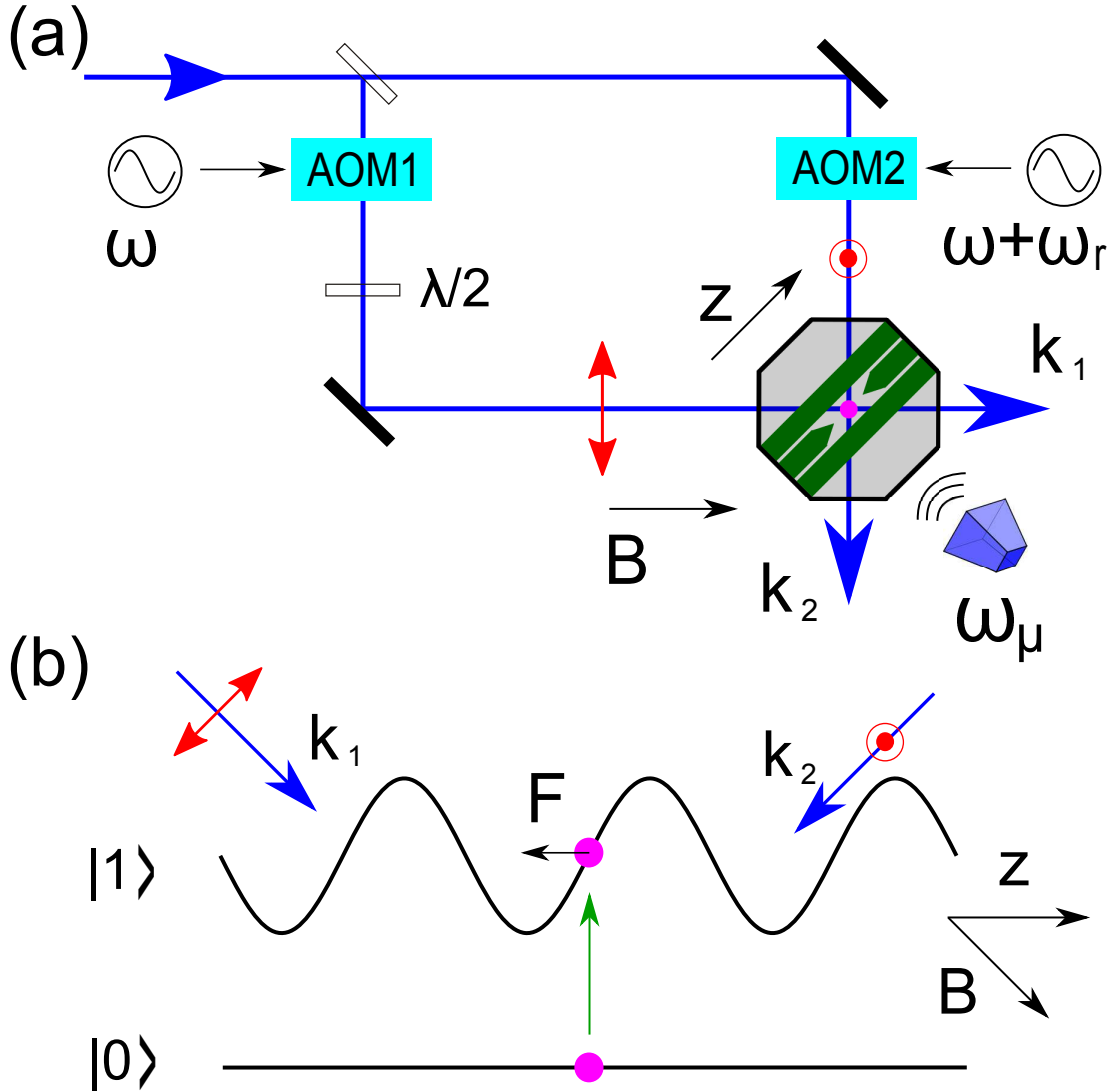


Figure 5.1: (a) Schematic of the experimental setup. Two laser beams of wavevectors  $\mathbf{k}_1$ ,  $\mathbf{k}_2$  and frequency difference  $\omega_r$  are overlapped onto the trapped  $^{171}\text{Yb}^+$  ion (pink dot) to form an optical lattice of running wave frequency  $\omega_r$  along  $\hat{z}$  direction. The red arrow or dot inside a circle represents the polarization of each lattice beam. (b) AC Stark shift for the  $|1\rangle$  and  $|0\rangle$  spin states in the optical lattice at a given instant of time. Spin-motion coupling is effected by the optical lattice imparting a kick ( $\mathbf{F}$ ) onto the ion upon the microwave field flipping the ion spin state.

## 5.1 Experimental setup

A schematic of the experimental setup is shown in Fig. 6.1(a). The single  $^{171}\text{Yb}^+$  ion is confined in the trap with the secular trapping frequencies  $(\omega_x, \omega_y, \omega_z) = 2\pi \times (0.91, 0.97, 0.79)$  MHz. The Doppler cooling, state initialization and detection are the same as introduced in Chapter 2. A magnetic field of 5.5 G is applied at  $45^\circ$  angle with respect to the optical lattice axis ( $\hat{z}$ ) to destabilize the dark states in the  $^2S_{1/2}$  manifold and lift the degeneracy between the  $^2S_{1/2}$  sublevels for state-selective addressing by microwave radiation. The qubit states in this chapter are  $|0\rangle \equiv |S_{1/2}, F = 0, m_F = 0\rangle$  and  $|1\rangle \equiv |S_{1/2}, F = 1, m_F = -1\rangle$ . Microwave radiation at 12.6 GHz, emitted by a microwave horn placed 5 cm away from the trap, is used to drive the magnetic dipole transition between  $|0\rangle$  and  $|1\rangle$  with a Rabi frequency of  $\Omega/2\pi = 43$  kHz.

The Raman beams in Chapter 2 serve as optical lattice beams. In this case, they are sent from two orthogonal directions that form  $45^\circ$  and  $135^\circ$  angles respectively with the  $\hat{z}$ -axis. The beams interfere at the ion position to generate an optical lattice superimposed on the harmonic ion trap potential. The polarizations of the two beams are linear and mutually orthogonal. In this configuration, the polarization in the optical lattice changes from linear to circular to orthogonal linear to opposite circular and back to linear within  $\sqrt{2}\lambda/2 = 2\pi/\Delta k$ , giving rise to a strong spatial dependence of the differential Stark shift between the  $|0\rangle$  and  $|1\rangle$  states of the trapped ion (see Fig.6.1(b)). Given the repetition rate of the laser is much faster than the trap frequency, only the average optical potential affects the ion motion. Hence, if the driving frequencies of the two AOMs differ by  $\omega_r$ , we will get effectively the same running optical lattice propagating along the  $\hat{z}$  direction, as if the pulsed laser is replaced by a continuous wave laser that

induces a differential AC Stark shift oscillating with amplitude  $\Delta\omega_0$ .

## 5.2 Measurement of the Stark shift

The energy splitting between  $|0\rangle$  and  $|1\rangle$  can be measured by driving  $|0\rangle \rightarrow |1\rangle$  transition with microwave radiation. In our case, each frequency scan typically takes a few seconds. It contains around 20 points, where each point is an average of 100 experiments, and each experiment takes around 3ms. The Stark shift, in principle, can be extracted by measuring the microwave resonance frequencies for different phases of the optical lattice. But it is technically challenging to stabilize and control the phase of the optical lattice with respect to the ion position long enough to complete a frequency scan. Instead, we try to include the contribution of all the phases into every point of the frequency scan by scanning the optical lattice phase. The scan is slow enough such that the optical lattice phase at the ion position does not change during a single  $10 \mu\text{s}$  microwave pulse, i.e.  $\omega_r \ll \Omega$ , but fast enough that the phase is random for each of 100 experiments (0.3 s) that contributes to a point in a frequency scan plot. We use scanning frequency of 10kHz, i.e.  $\omega_r/(2\pi) = 10 \text{ kHz}$ , and scan the microwave frequency with microwave pulse of  $11.0 \mu\text{s}$ . The data is shown in Fig. 5.2 (h). For simplicity, we fit it with a weighted average of Rabi profile with uniform frequency distribution over the oscillating range. We can see from Fig. 5.2 h that it qualitatively fits. The oscillating amplitude of the Stark shift is estimated to be  $\Delta\omega_0/2\pi = 310(10) \text{ kHz}$ .

Fig. 5.2 also shows microwave frequency scan profiles for a series of different running frequencies. In Fig. 5.2 (a), the optical lattice is standing, i.e.  $\omega_r = 0$ . The phase fluctuation is caused by the interferometric instability only. The average effect for a certain point does not show up systematically. This means that

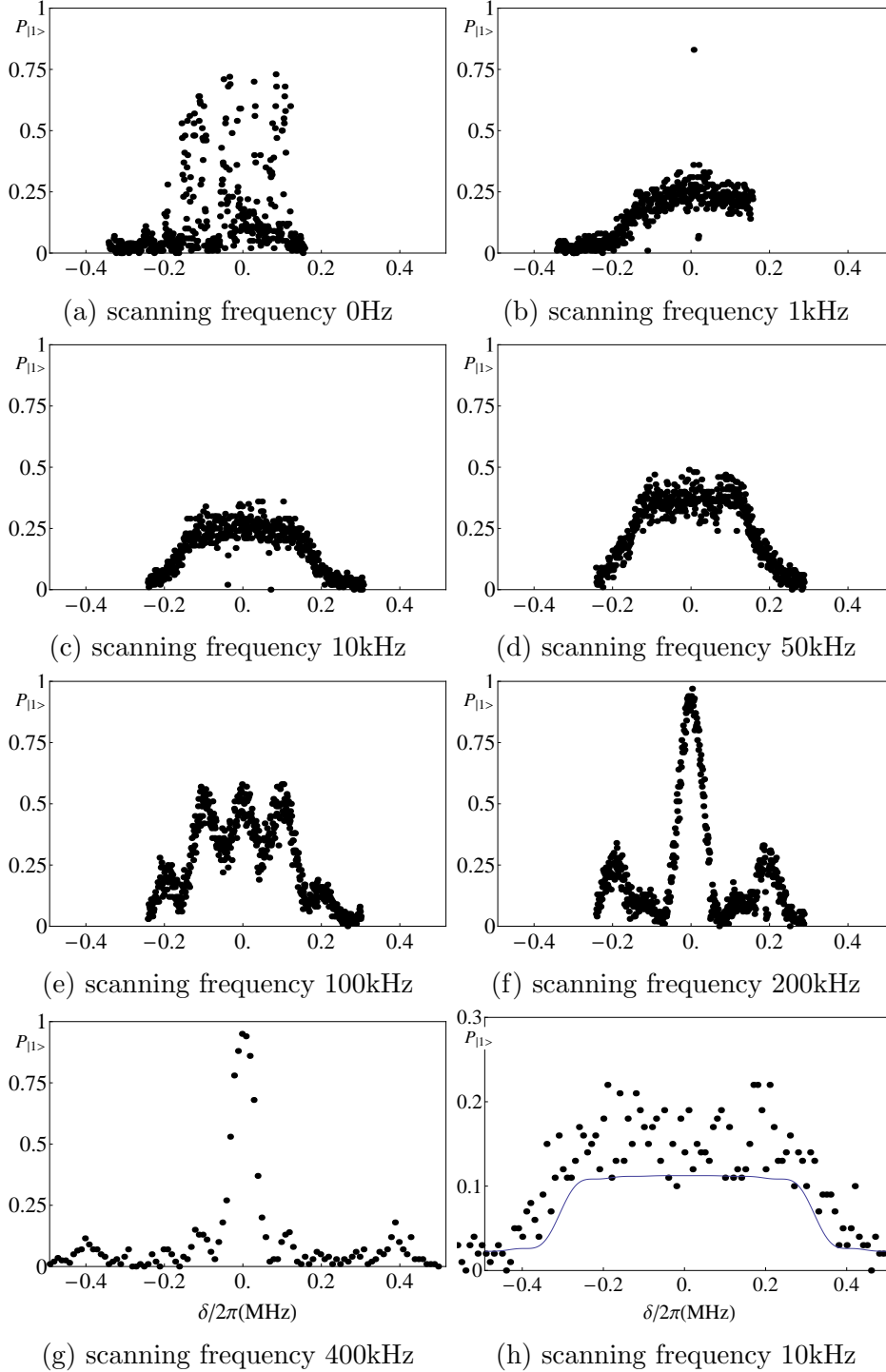


Figure 5.2: Microwave frequency scans in the presence of a running optical lattice with 0 Hz (a), 1 kHz (b), 10 kHz (c), 50 kHz (d), 100 kHz (e), 200 kHz (f), 400 kHz (g), 10 kHz (h). The microwave pulse duration is set such that it can flip the spin completely without the Raman beams. This  $11.8 \mu\text{s}$  for (a) to (g) and  $11.0 \mu\text{s}$  for (h).

the time scale over which the phase of the optical lattice is stable is comparable to the time to measure one point, i.e. 0.3 s. This is consistent with the assumption we had previously: the relative phase between two optical beams is stable for the duration of a single experimental cycle.

When the optical lattice is running, in the frame of the ion, the microwave detuning appears to be sinusoidally frequency modulated with oscillation amplitude of  $\Delta\omega_0$ . This frequency modulation gives rise to sidebands surrounding the main carrier separated from each other by modulation frequency. When the lineshape is broader than the modulation frequency, i.e.  $\Omega \gg \omega_r$ , the sidebands can not be resolved. This is shown in Fig. 5.2 (a) to (d). It is also true for the data presented in Fig. 5.2 (h), which we use to measure the Stark shift oscillation amplitude  $\Delta\omega_0$ . When the modulation frequency is comparable or higher than the Rabi frequency, however, the accompanying sidebands will be resolved. The small sidebands can be clearly seen in Fig. 5.2 (g).

In addition, the amplitudes of the carrier and the symmetrically placed sidebands follow the Bessel function of the first kind. Fig. 5.3 shows the relative intensity of the carrier, the first order sidebands and the second order sidebands as a function of the modulation index  $\beta = \Delta\omega_0/\omega_r$ . The fact that  $J_0(\beta) = 0$  at  $\beta = \Delta\omega_0/\omega_r \approx 2.4$  may offer a way to a more precise measurement of the  $\Delta\omega_0$  since  $\omega_r$  can be known precisely.

In this experiment, care is also taken to choose the repetition rate of the pulsed laser such that the generated frequency comb does not drive any stimulated Raman transitions between hyperfine states of the  $\text{Yb}^+$  ion [47].

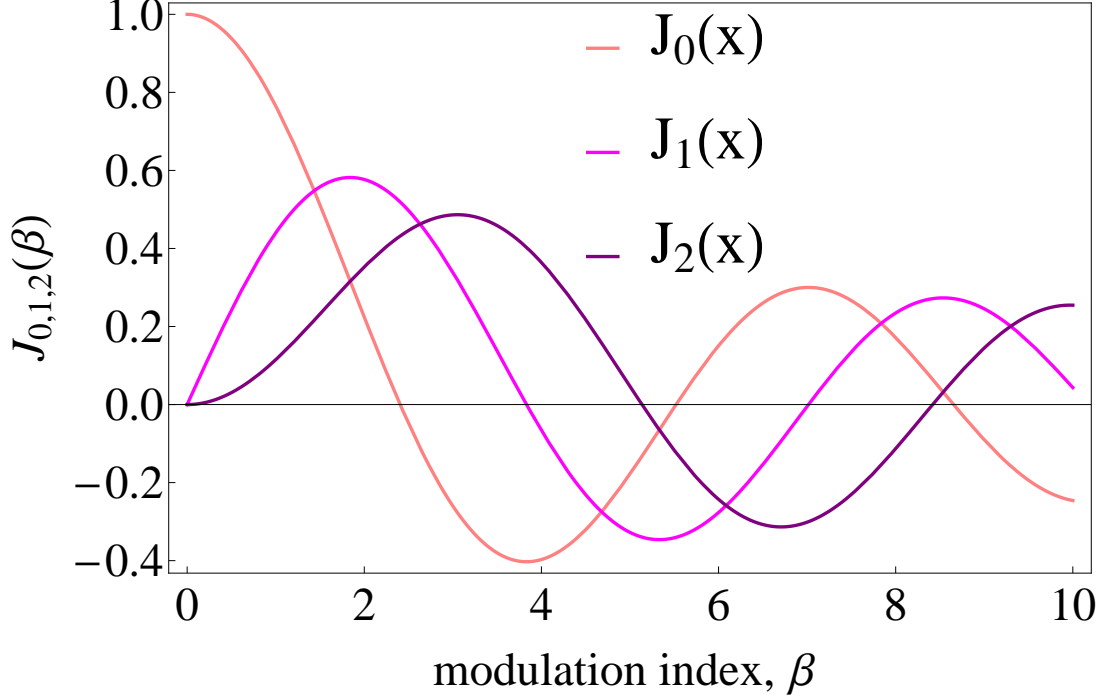


Figure 5.3: Bessel function of the first kind. Relative intensity of the main carrier, the first and second sidebands due to the running optical lattice. Note that  $J_0(\beta) = 0$  if  $\beta = \Delta\omega_0/\omega_r \approx 2.4$

### 5.3 Theory

We assume that the ion does not move in the previous section. Now let us derive a comprehensive theory to include the influence of the motion of the ion.

The interaction of a trapped ion with the running optical lattice and microwave field of frequency  $\omega_\mu$  can be described by a Hamiltonian of the form  $H = H_0 + V(t)$ , where

$$\begin{aligned}
 H_0 &= \hbar\omega_z a^\dagger a + \frac{1}{2}\hbar\omega_0 \sigma_z, \\
 V(t) &= \frac{1}{2}\hbar\sigma_z \delta\omega_0(z, t) + \frac{1}{2}\hbar\Omega(\sigma_+ + \sigma_-)(e^{-i\omega_\mu t} + e^{i\omega_\mu t}).
 \end{aligned} \tag{5.1}$$

Here  $\hbar\omega_0$  is the energy difference between the ion internal states  $|0\rangle$  and  $|1\rangle$ ,  $\sigma_z = |1\rangle\langle 1| - |0\rangle\langle 0|$ ,  $\sigma_+ = |1\rangle\langle 0|$ ,  $\sigma_- = |0\rangle\langle 1|$ ,  $a^\dagger$  and  $a$  are creation and annihilation operators for the ion motional mode,  $\omega_z$  is the secular trap frequency,  $\Omega$  is the microwave transition Rabi frequency, and  $\delta\omega_0(z, t) = \Delta\omega_0 \sin(\Delta kz - \omega_r t)$  is the differential Stark shift of the ion energy levels in the presence of the running optical lattice. In the Lamb-Dicke regime, near the ion equilibrium position  $z = 0$ , we can keep only terms to the first order in  $z$  in an expansion of the differential Stark shift expression, i.e.

$$\delta\omega_0(z, t) = \Delta\omega_0(-\sin \omega_r t + \eta(a^\dagger + a) \cos \omega_r t). \quad (5.2)$$

Here  $\eta = \Delta kz_0$  is the Lamb-Dicke parameter,  $z_0 = \sqrt{\hbar/2m\omega_z}$  is the spread of the ion wave function along the  $\hat{z}$  direction, and  $m$  is the ion mass.

After transforming the Hamiltonian to the interaction picture

$$H_i(t) = e^{iH_0 t/\hbar} V(t) e^{-iH_0 t/\hbar} \quad (5.3)$$

and using the rotating wave approximation for the microwave interaction, we obtain

$$\begin{aligned} H_i(t) = & \frac{1}{4} \hbar \Delta\omega_0 \eta \sigma_z a (e^{-i(\omega_z + \omega_r)t} + e^{-i(\omega_z - \omega_r)t}) \\ & - \frac{i}{4} \hbar \Delta\omega_0 \sigma_z e^{-i\omega_r t} + \frac{1}{2} \hbar \Omega \sigma_+ e^{-i\delta t} + H.c., \end{aligned} \quad (5.4)$$

where  $\delta = \omega_\mu - \omega_0$  is the detuning of the microwave field from the  $|0\rangle \rightarrow |1\rangle$  transition.

Following Ref. [61] and dropping fast oscillating terms, the effective Hamilto-

nian for the detuning  $\delta = \pm\omega_r$  is given by

$$H_{st} = i\hbar\Delta\omega_0\Omega(\sigma_+ - \sigma_-)/(4\omega_r), \quad (5.5)$$

which corresponds to a change in the ion internal spin state only, i.e.  $|0\rangle|n_m\rangle \rightarrow |1\rangle|n_m\rangle$ , where  $|n_m\rangle$  means the motional Fock state with phonon number  $n$ . In a similar way, the effective Hamiltonian for the sidebands at detuning  $\delta = -(\omega_z \pm \omega_r)$  can be written as

$$H_{rsb} = -\frac{\hbar\Delta\omega_0\eta\Omega}{4(\omega_z \pm \omega_r)} (a\sigma_+ + a^\dagger\sigma_-). \quad (5.6)$$

When tuned to this red sideband [157], the microwave field drives the  $|0\rangle \rightarrow |1\rangle$  transition while destroying a phonon in the ion motional mode, i.e.  $|0\rangle|n_m\rangle \rightarrow |1\rangle|(n-1)_m\rangle$ . When the condition  $\delta = \omega_z \pm \omega_r$  is satisfied, the effective Hamiltonian given by

$$H_{bsb} = \frac{\hbar\Delta\omega_0\eta\Omega}{4(\omega_z \pm \omega_r)} (a\sigma_- + a^\dagger\sigma_+) \quad (5.7)$$

describes blue sidebands, which characterizes the transition  $|0\rangle|n_m\rangle \rightarrow |1\rangle|(n+1)_m\rangle$ . The spin-motion couplings induced by these terms are analogous to the more familiar red and blue sidebands driven by a pair of Raman lasers [157], but with the Lamb-Dicke parameter replaced by  $\eta_{\pm}^{eff} = \eta\Delta\omega_0/(2(\omega_z \pm \omega_r))$ .

## 5.4 Experimental characterization of the Hamiltonian

The measured probability of the  $|0\rangle \rightarrow |1\rangle$  transition as a function of the microwave detuning  $\delta$  is shown in Fig. 5.4 for  $\omega_r/2\pi = 300$  kHz. Three kinds of

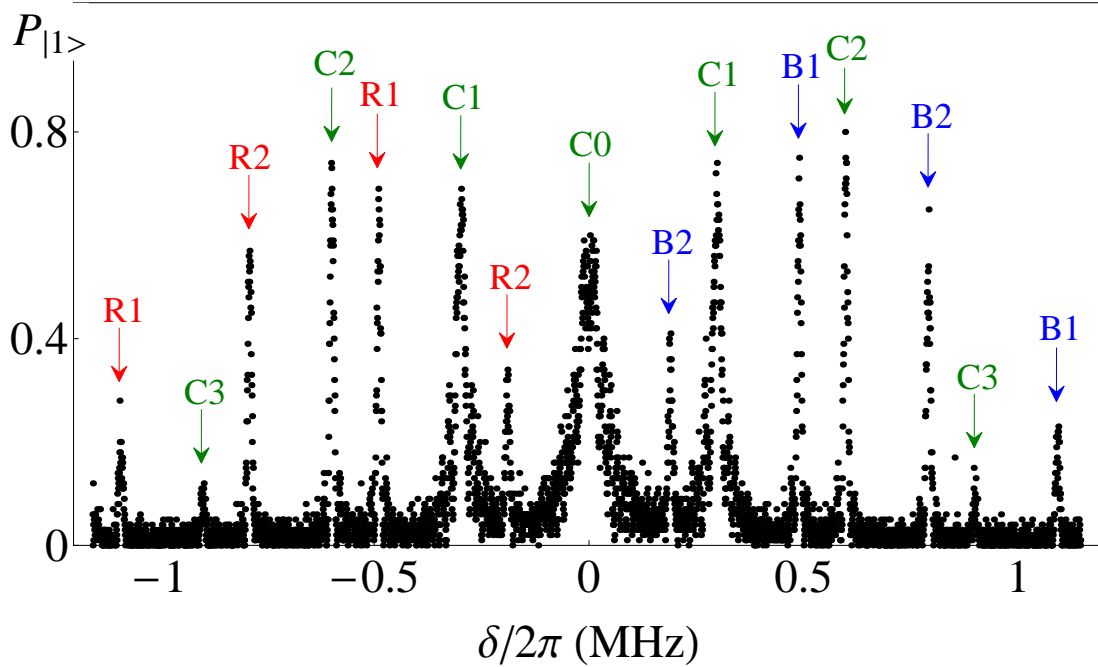


Figure 5.4: Probability of the  $|0\rangle \rightarrow |1\rangle$  transition after a  $75 \mu\text{s}$  microwave pulse as a function of microwave detuning  $\delta$ . Every point is the average of 100 measurements. The peak labeled C0 corresponds to the carrier microwave transition, while R1 and B1 correspond to the red and blue motional sidebands respectively. Peaks labeled  $C_n$ ,  $R_n$ ,  $B_n$  contain contributions from higher order terms that scale as  $(\Delta\omega_0/\omega_z)^n$ .

transitions can be identified in this graph. The main carrier peak (C0) corresponds to the transition between the internal states of the ion without changing its motional state. It is accompanied by a series of smaller peaks  $C_n$  separated by  $\omega_r$  that correspond to higher order terms that scale as  $(\Delta\omega_0/\omega_r)^n$ . This is consistent with the description using Bessel function, since  $J_n(\beta)$  scale as  $\beta^n$  when  $\beta = \Delta\omega_0/\omega_r$  is small. This has been recognized in Fig. 5.2. The B1 (R1) sidebands at the detunings  $\omega_z \pm \omega_r$  and  $-(\omega_z \pm \omega_r)$  respectively correspond to transitions that change both internal and motional states of the ion, and are described by the effective Hamiltonian  $H_{bsb}$  ( $H_{rsb}$ ). As in the case of the carrier, these peaks are accompanied by sidebands of higher order in  $\Delta\omega_0/\omega_r$ .

According to Eqn. 5.7, the transition at blue sideband B1, i.e.  $|0\rangle|n_m\rangle \rightarrow |1\rangle|(n+1)_m\rangle$ , will have the Rabi frequency of

$$\Omega_{nB1} = \sqrt{n+1}\Omega_{0B1} \quad (5.8)$$

where

$$\Omega_{0B1} = \eta_{\pm}^{eff}\Omega \quad (5.9)$$

is the Rabi frequency of the transition  $|0\rangle|0_m\rangle \rightarrow |1\rangle|1_m\rangle$ . To extract  $\Omega_{0B1}$ , the internal-state evolution of the Doppler-cooled ion is measured for a given running lattice frequency  $\omega_r$  and microwave detuning  $\delta = \omega_z \pm \omega_r$  (see Fig. 5.5 inset). It is then fit to a weighted average of Rabi oscillations assuming a thermal distribution of phonons [95]. The ion temperature corresponds to an average phonon number  $\langle n \rangle = 18(2)$ . As plotted in Fig. 5.5 (blue dots and green triangles), the Rabi frequencies for the two B1 sidebands are generally asymmetric over a wide range of  $\omega_r$ . The blue and green solid lines are theory curves, described by  $\Omega_{0B1} = \eta_{\pm}^{eff}\Omega$  with no free parameters. Also depicted in Fig. 5.5 are the experimental (red squares) and theoretical (red line) Rabi frequencies for the C1 sideband at  $\delta = \omega_r$ , where the former one is extracted by a fit to an exponentially decaying sinusoidal function, while the latter one is given by  $\Omega_{C1} = \Delta\omega_0\Omega/2\omega_r = \beta\Omega/2$ . The uncertainty of the theoretical prediction, which comes from uncertainties in  $\Omega$ ,  $\eta$  and  $\Delta\omega_0$ , is represented by the thickness of the solid lines in Fig. 5.5. As expected from Eq. (5.7), the Rabi frequency of the  $\omega_z - \omega_r$  sideband exhibits resonance behavior when  $\omega_r$  approaches  $\omega_z$ . The discrepancy between the theoretical prediction and experimental values near the resonance is due to the limitations of our theoretical treatment. The theory describing motional sidebands is valid under

conditions  $\eta \ll 1$  and  $\Delta\omega_0/(\omega_z \pm \omega_r) \ll 1$  and does not take into account higher order terms in  $\Delta\omega_0/\omega_r$ . A better model to describe the C1 sideband, especially in the range where  $\omega_r$  is small, i.e.  $\beta$  is big, will be the Bessel function  $\Omega J_1(\beta)$ , which is shown as the orange line in Fig. 5.5.

The strong dependence of the R1, B1 sideband Rabi frequencies on  $\omega_r$  opens up the possibility of speeding up operations that depend on spin-motion coupling. For example, in order to speed up the sideband cooling, we can either increase  $\Delta\omega_0$  and  $\Omega$  by increasing the lattice laser power and the microwave power respectively, or decrease  $\omega_z \pm \omega_r$  by adjusting  $\omega_r$ . In the latter case, care should be taken such that the motional sidebands do not overlap with the carriers.

## 5.5 Sideband cooling

To demonstrate sideband cooling, we revert to the case of  $\omega_r/2\pi = 300$  kHz and use the red sideband at the detuning  $\delta = \omega_r - \omega_z = -2\pi \times 490$  kHz (R1). After 1 ms of Doppler cooling, 200 microwave pulses at the detuning  $\delta$  are applied to the ion. Each pulse is followed by 5  $\mu$ s of optical pumping to reinitialize the ion back in the  $|0\rangle$  state. The duration of the microwave pulse is increased from 60 to 230  $\mu$ s in steps of approximately 1  $\mu$ s throughout the sideband cooling sequence to account for the increased  $\pi$  time of the sideband transition as the mean phonon number decreases. The corresponding red and blue sidebands before and after sideband cooling are shown in Fig. 4. The red sideband after sideband cooling is mostly diminished. The height of the sideband-cooled blue sideband is limited by decoherence of the  $|0\rangle \rightarrow |1\rangle$  transition (coherence time 0.47(4) ms, see below), which is mostly attributed to magnetic field noise. From the asymmetry of the red and blue sidebands, we estimate the average number of phonons in the motional

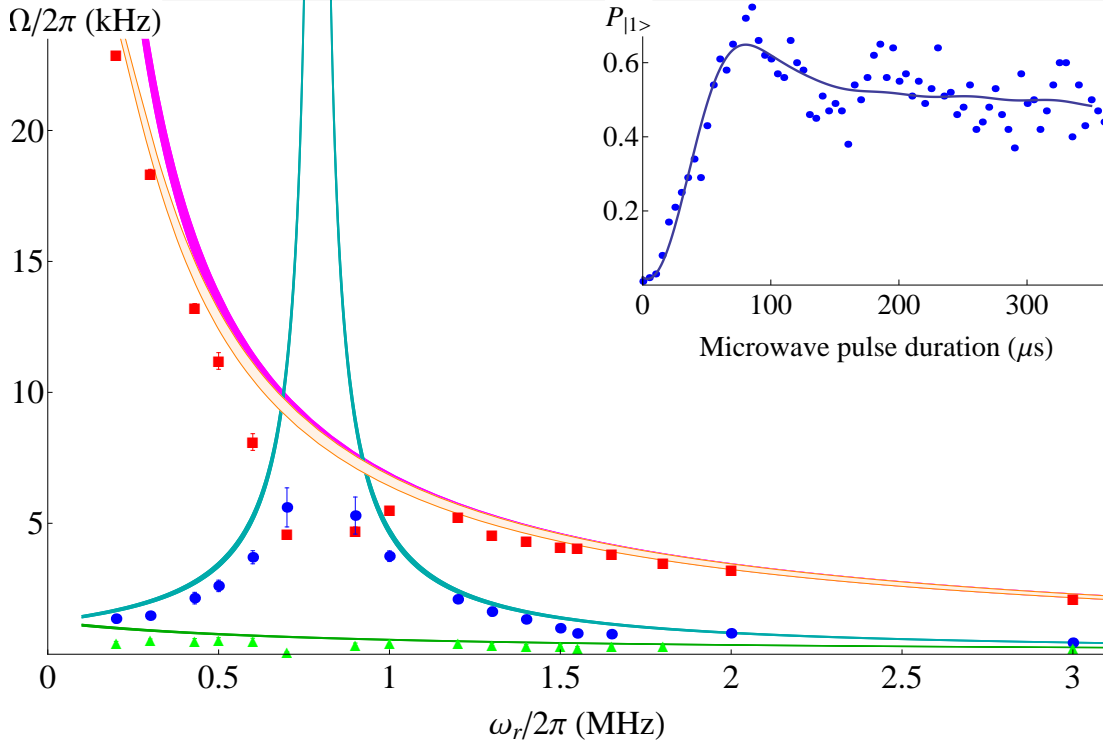


Figure 5.5: Rabi frequencies for the microwave detuning  $\delta = \omega_r$  (red squares, C1),  $\delta = \omega_z - \omega_r$  (blue dots, B1) and  $\delta = \omega_z + \omega_r$  (green triangles, B1), plotted as a function of the running lattice frequency  $\omega_r$ . The solid lines are theoretical predictions with no free parameters, with their thickness representing prediction uncertainty. The Rabi frequencies  $\Omega_{B1}$  are obtained from the internal state evolution of the ion as shown in the inset for  $\delta = \omega_z - \omega_r = 2\pi \times 490$  kHz. The Rabi oscillation data is fit assuming a thermal distribution of phonons after Doppler cooling.

mode of the ion to be  $\langle n \rangle = 0.02^{+0.04}_{-0.02}$ .

The internal-state evolutions of the ion after sideband cooling are also measured at microwave detuning  $\delta = \omega_z - \omega_r = 2\pi \times 490$  kHz (B1) and  $\delta = \pm\omega_r = \pm 2\pi \times 300$  kHz (C1) (Fig. 5.7, right column). For comparison, the corresponding evolutions before sideband cooling are shown as well (Fig. 5.7, left column). For blue sideband (B1), instead of a beating of Rabi oscillations with different frequencies resulting from different phonon numbers, as in Fig. 5.5 inset and Fig. 5.7(a),

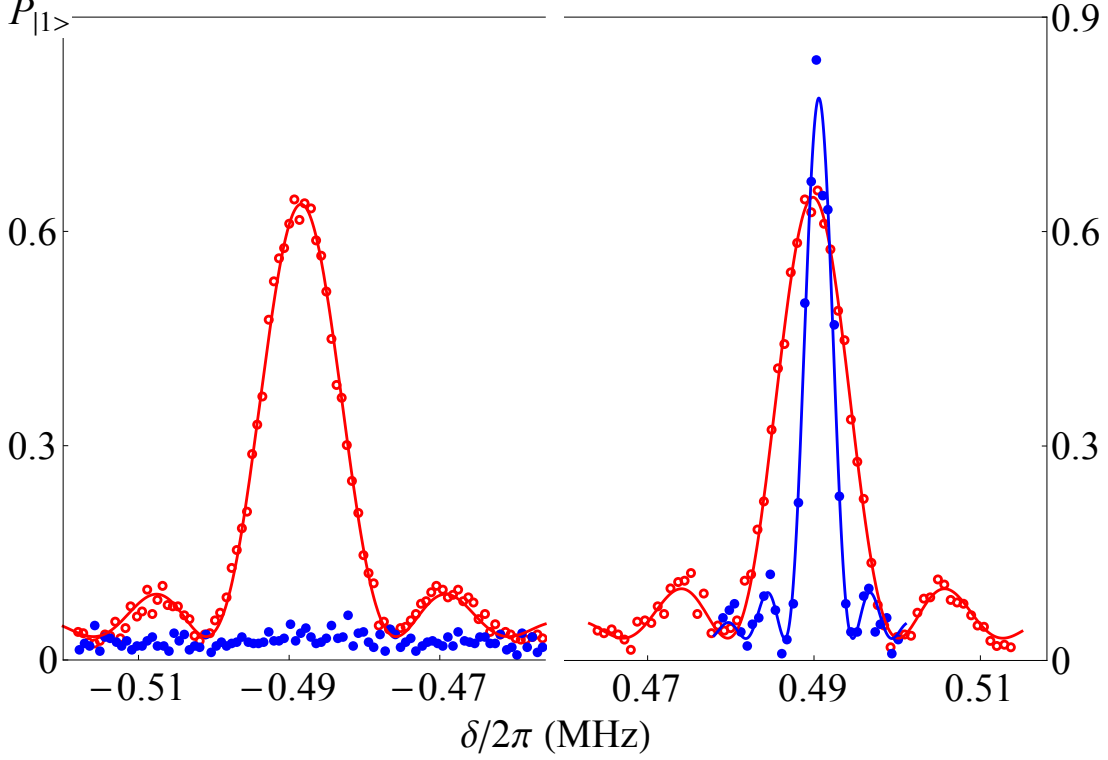


Figure 5.6: Probability of the  $|0\rangle \rightarrow |1\rangle$  transition for red sideband (left, R1) and blue sideband (right, B1) at detunings  $\delta = \mp(\omega_z - \omega_r)$  before (red open-circles, microwave pulse duration  $80 \mu\text{s}$ ) and after (blue dots, microwave pulse duration  $230 \mu\text{s}$ ) sideband cooling. Suppression of the red sideband after sideband cooling indicates cooling to near the motional ground state.

we see a decaying sinusoidal curve with a single frequency (Fig. 5.7(b), blue dots), which is supposed to be  $\Omega_{0B1}$ . The internal-state evolution before sideband cooling without lattice beams, i.e. purely driven by microwave, is also measured for comparison (Fig. 5.7(b), red dots). The microwave power is adjusted such that the Rabi frequency is also  $\Omega_{0B1}$ . We know, in this case, the decay is due to magnetic field noise. Two curves overlap with each other very well, verifying that the decay in the internal-state evolution at blue sideband after sideband cooling (Fig. 5.7(b), blue dots) is mainly caused by the decoherence of the  $|0\rangle \rightarrow |1\rangle$  magnetically sensitive transition as well.

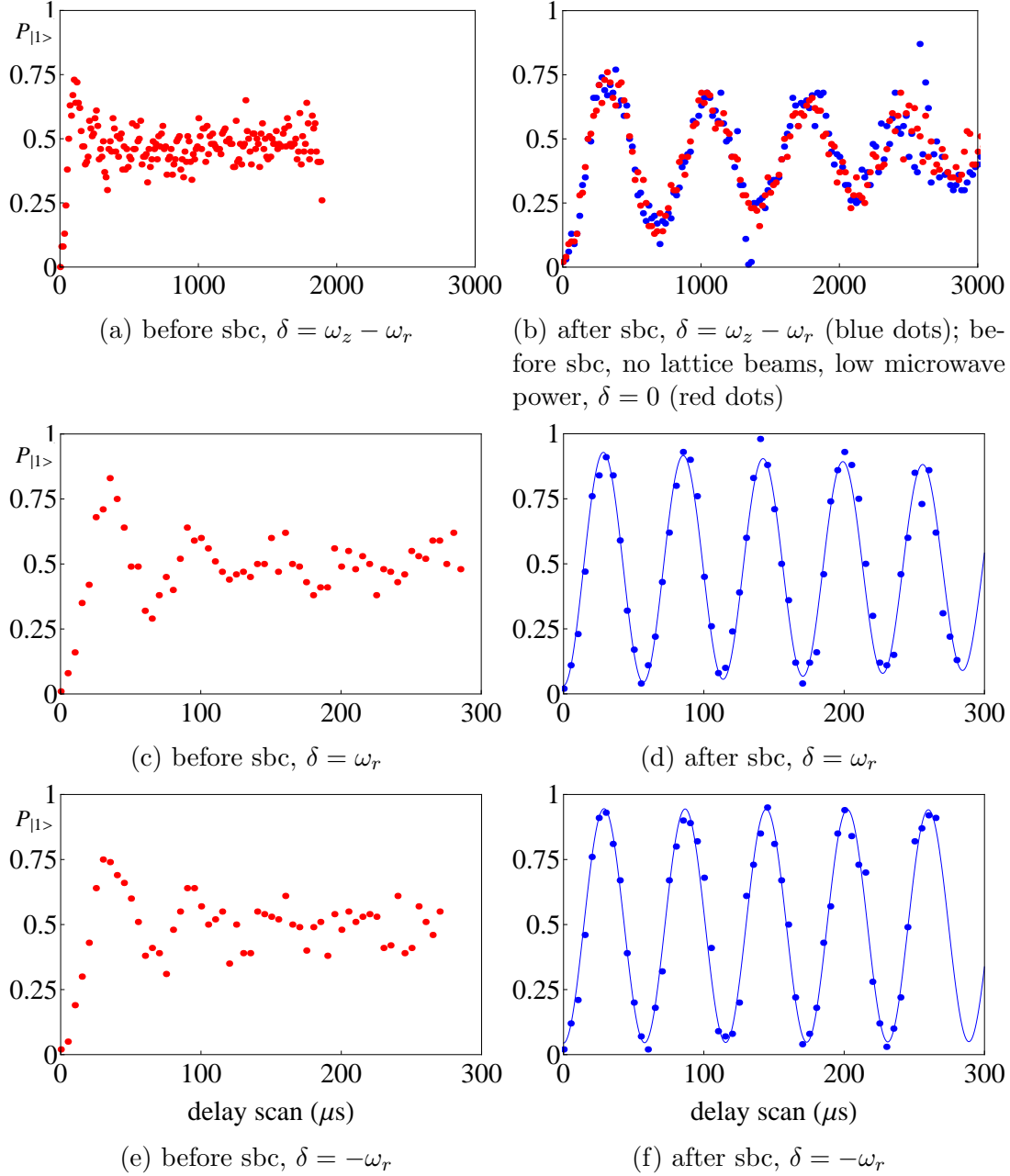


Figure 5.7: Internal-state evolution at various carriers and sidebands before (red dots) and after (blue dots) sideband cooling (sbc). The microwave and lattice beams power are the same in all the figures except the red dots in (b), which are used for comparison with blue dots in the same figure. The microwave power in this case is lowered such that the spin evolves at similar Rabi frequency as the blue dots. The blue lines in (d) and (f), which are fit to decaying sinusoidal functions, are used to guide the eye.

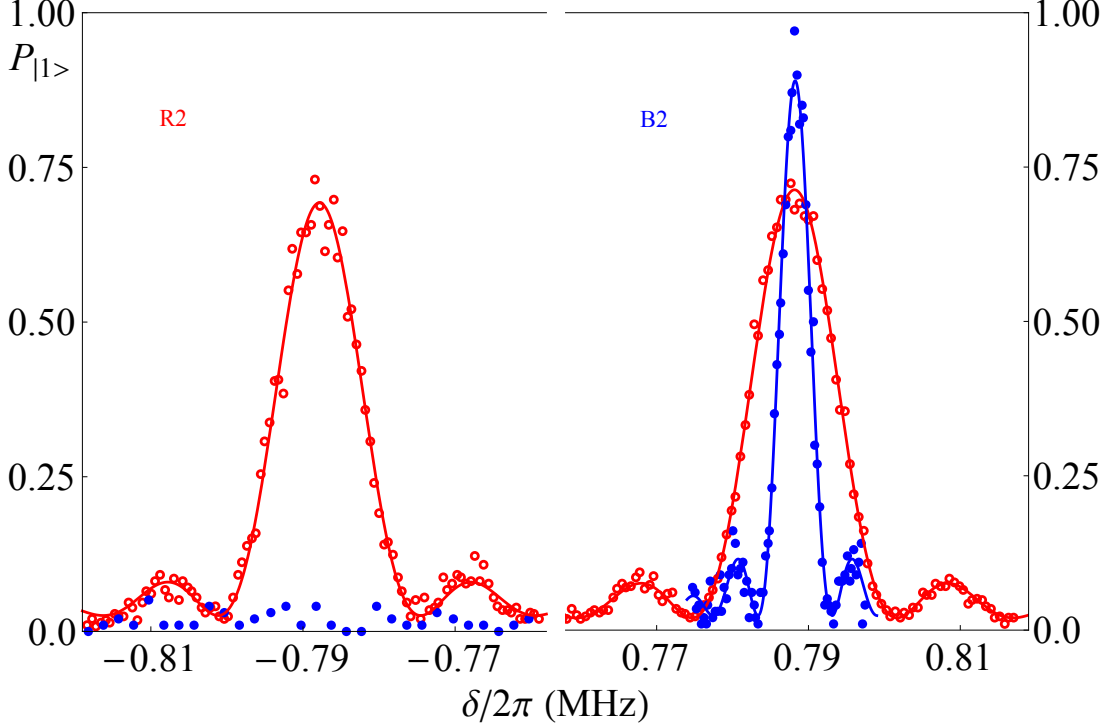


Figure 5.8: Probability of the  $|0\rangle \rightarrow |1\rangle$  transition for red sideband (left, R2) and blue sideband (right, B2) at detunings  $\delta = \mp\omega_z$  before (red open-circles, microwave pulse duration  $70 \mu\text{s}$ ) and after (blue dots, microwave pulse duration  $180 \mu\text{s}$ ) sideband cooling at the detuning  $\delta = -\omega_z$ . Suppression of the red sideband after sideband cooling indicates cooling to near the motional ground state. Note that the microwave power here is larger than that in Fig. 5.6 and the coherence time of transition  $|0\rangle \rightarrow |1\rangle$  is longer as well.

Similar effects are observed for the carriers (C1). Before sideband cooling, the evolutions are given by beatings of different frequency components (Fig. 5.7 (c) and (e)). After sideband cooling, they are decaying sinusoidal curves (Fig. 5.7 (d) and (f)). We would like to point out that the phonon-number-dependence for carriers comes from high order terms, similar to the internal and motional states coupling introduced in Chapter 2 (Eqn. 2.54).

In addition, the red sideband at detuning  $\delta = -\omega_z = -2\pi \times 790 \text{ kHz}$  (R2) was also used to achieve sideband cooling. The time sequence is similar to

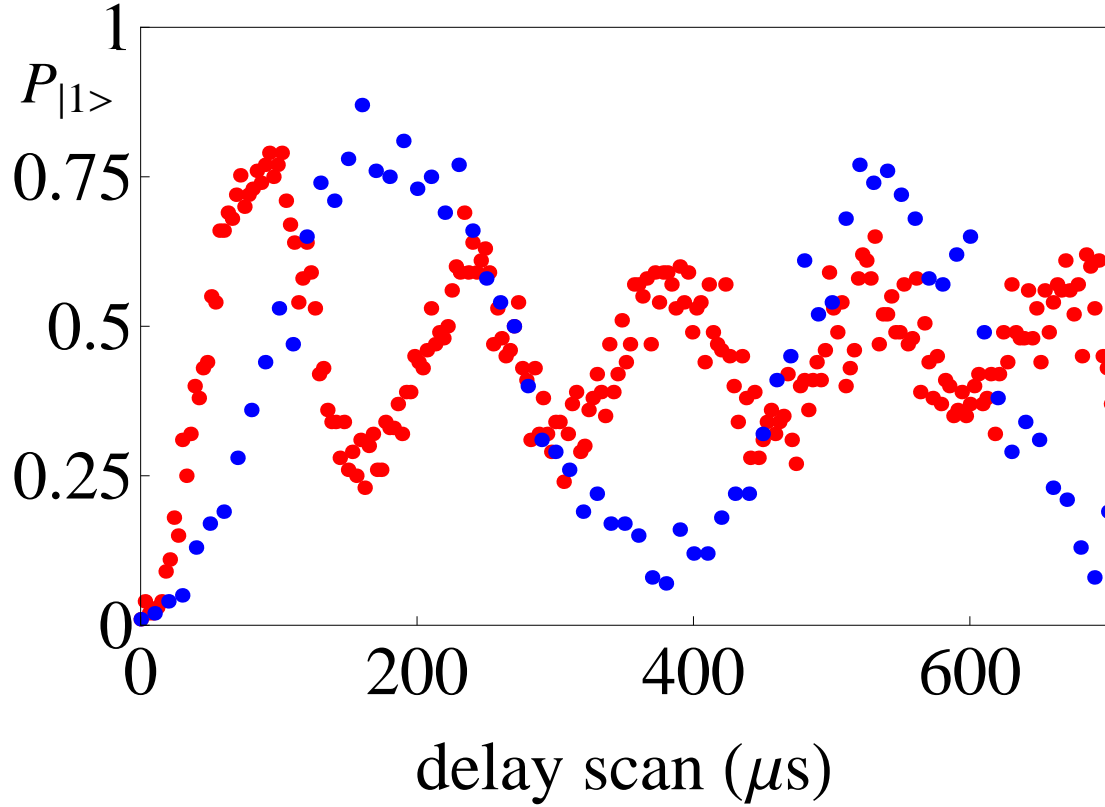


Figure 5.9: Internal-state evolution at blue sideband B2,  $\delta = \omega_z$ , before (red dots) and after (blue dots) sideband cooling at the detuning  $\delta = -\omega_z$ .

sideband cooling at the detuning  $\delta = \omega_r - \omega_z = -2\pi \times 490$  kHz (R1) that we describe previously, i.e. Doppler cooling and 200 cycles of microwave pulses with increasing pulse duration and each pulse followed by optical pumping. The corresponding red and blue sidebands before and after sideband cooling are shown in Fig. 5.8. Similarly, the average number of phonons after sideband cooling is estimated to be  $\langle n \rangle = 0.02 \pm 0.02$ . The internal-state evolution at blue sideband  $\delta = \omega_z = 2\pi \times 790$  kHz (B2) before and after sideband cooling at the detuning  $\delta = -2\pi \times 790$  kHz is shown in Fig. 5.9. As expected, the plot shows beating of different frequencies before sideband cooling and a decaying sinusoidal curve with single frequency after sideband cooling.

## 5.6 Conclusion and outlook

We realize spin-motion coupling for a single trapped ion using a uniform microwave field assisted by a running optical lattice. This technically simple scheme allows us to cool the ion to the ground state of motion. By increasing the coherence time of the magnetic-field-sensitive transition (e.g. by triggering the experiment with the main line), a high-fidelity quantum gate may be feasible. The running lattice-microwave combination offers two tiers of flexibility on the spin-motion coupling strength: one can either vary the optical lattice depth or tune the running lattice frequency relative to the secular trap frequency. The increased flexibility allows for more tunable quantum logic gates and spin-spin couplings mediated by phonon modes, where the latter can be exploited in quantum simulation [10; 64; 65] or studies of transport properties of the ions interacting with the optical lattice [7; 36; 63; 86; 115]. This technique also paves the way for molecular ion quantum logic spectroscopy [34; 72], by which the rich internal structure of molecular ions and their motion can be accessed [134].

# Chapter 6

## Phonon down-conversion in a linear ion trap

### 6.1 Introduction

The collective normal modes of the oscillation of a string of trapped ions play an essential role in quantum information processing. The potential each ion feels is a combination of the harmonic potential generated by the external electric field and the Coulomb interaction with other ions inside the trap. When the ions are sufficiently cold, e.g., after Doppler cooling, the ions oscillate with small enough amplitudes around their equilibrium positions, such that we can approximate the Coulomb potential with a Taylor series expansion to the second order without a noticeable loss of accuracy to describe the dynamics of the ions. It results in a set of independent harmonic oscillators, which corresponds to  $3N$  normal modes of motion for  $N$  ions. However, the higher order term in the Taylor expansion of Coulomb potential leads to nonlinear coupling between otherwise independent modes. Under some resonance condition, the harmonic approximation breaks

down.

In this chapter, we describe the engineering of the nonlinear interaction between modes of motion at the single-phonon level. This interaction is analogous to the degenerate optical parametric down conversion[92]. We use the nonlinearity to directly measure the parity of different quantum states of ion motion, from which we derive their corresponding Wigner functions.

## 6.2 Theory

In the following, we show theoretically how the intrinsic anharmonicity of Coulomb potential leads to the nonlinear coupling between different modes in a two-ion crystal in the trap. We note that this derivation has been presented previously [93; 106], but we detail the derivation in the case particularly interesting for our experiment for completeness.

We consider a system of two ions with the same mass  $m$  and charge  $e$  trapped in a linear Paul trap. Suppose that the trap potential is characterized by the single ion trapping frequencies  $\omega_z, \omega_x, \omega_y$  and  $\omega_z < \omega_x, \omega_y$ . In this case, the ions arrange themselves in the line along  $z$  (axial) direction, where the confinement is weaker. Following the notations in Eqn. 4.6, the kinetic energy  $T$  and potential energy  $V$  of the system have the form

$$T = \frac{1}{2}m(\dot{x}_1^2 + \dot{x}_2^2) + \frac{1}{2}m(\dot{y}_1^2 + \dot{y}_2^2) + \frac{1}{2}m(\dot{z}_1^2 + \dot{z}_2^2) , \quad (6.1)$$

$$V = \frac{1}{2}m\omega_x^2(x_1^2 + x_2^2) + \frac{1}{2}m\omega_y^2(y_1^2 + y_2^2) + \frac{1}{2}m\omega_z^2((z_1 + z_0)^2 + (z_2 - z_0)^2) \\ + \frac{e^2}{4\pi\epsilon_0} \frac{1}{\sqrt{(x_1 - x_2)^2 + (y_1 - y_2)^2 + (z_1 - z_2 + 2z_0)^2}} , \quad (6.2)$$

These expressions are simplified if we transform the coordinates as  $X = (x_1 +$

$x_2)/2$ ,  $Y = (y_1 + y_2)/2$ ,  $Z = (z_1 + z_2)/2$ , which describes the center of mass motion of the ions, and  $x = (x_1 - x_2)/2$ ,  $y = (y_1 - y_2)/2$ ,  $z = (z_1 - z_2)/2$ , which describes the relative motion. The Lagrangian then takes the form

$$\begin{aligned}
\mathcal{L} &= T - V \\
&= (m\dot{X}^2 - m\omega_x^2 X^2) + (m\dot{Y}^2 - m\omega_y^2 Y^2) - (m\dot{Z}^2 + m\omega_z^2 Z^2) \\
&\quad + (m\dot{x}^2 + m\dot{y}^2 + m\dot{z}^2) - (m\omega_x^2 x^2 + m\omega_y^2 y^2 + m\omega_z^2 (z + z_0)^2) \\
&\quad + \frac{e^2}{8\pi\epsilon_0} \frac{1}{\sqrt{x^2 + y^2 + (z + z_0)^2}}. \tag{6.3}
\end{aligned}$$

This formula shows that the three center-of-mass modes (in-phase modes) are purely harmonic. They are decoupled from the out-of-phase (OP) modes. On the other hand, the OP modes are coupled to each other by the Coulomb interaction. For our purpose, we drop the center-of-mass modes and consider only the OP modes.

By defining the canonical momentum in the standard way ( $p_x = \partial\mathcal{L}/\partial\dot{x}$  and similarly for  $p_y$  and  $p_z$ ), we write down the Hamiltonian for OP modes as follows,

$$\begin{aligned}
H &= \frac{1}{4m}(p_x^2 + p_y^2 + p_z^2) + m\omega_x^2 x^2 + m\omega_y^2 y^2 + m\omega_z^2 (z + z_0)^2 \\
&\quad + \frac{e^2}{8\pi\epsilon_0} \frac{1}{\sqrt{x^2 + y^2 + (z + z_0)^2}}. \tag{6.4}
\end{aligned}$$

For small displacements  $x$ ,  $y$ ,  $z$ , if we expand the Hamiltonian to the second order, we obtain three independent OP modes,

$$\begin{aligned}
H_0 &= \left(\frac{1}{4m}p_x^2 + m\omega_{xop}^2 x^2\right) + \left(\frac{1}{4m}p_y^2 + m\omega_{yop}^2 y^2\right) \\
&\quad + \left(\frac{1}{4m}p_z^2 + m\omega_{zop}^2 z^2\right). \tag{6.5}
\end{aligned}$$

However, if we include the terms up to the third order, we get an extra coupling term

$$V^{(3)} = \frac{m\omega_{zop}^2(x^2 + y^2)z}{z_0} + m\omega_{zop}^2\left(z_0^2 - \frac{2z}{3z_0}z^2\right). \quad (6.6)$$

The term  $m\omega_{zop}^2z_0^2$  is a constant and does not influence the dynamics. The last term ( $\sim z^3$ ) does not lead to the coupling between the modes. After dropping both terms, the Hamiltonian is

$$\begin{aligned} H &= H_0 + H_c \\ &= \left(\frac{1}{4m}p_x^2 + m\omega_{xop}^2x^2\right) + \left(\frac{1}{4m}p_y^2 + m\omega_{yop}^2y^2\right) + \left(\frac{1}{4m}p_z^2 + m\omega_{zop}^2z^2\right) \\ &\quad + \frac{m\omega_{zop}^2(x^2 + y^2)z}{z_0}. \end{aligned} \quad (6.7)$$

To quantize the motion, we introduce the following operators:

$$\hat{x} = \sqrt{\frac{\hbar}{4m\omega_{xop}}}(\hat{a} + \hat{a}^\dagger), \quad (6.8)$$

$$\hat{y} = \sqrt{\frac{\hbar}{4m\omega_{yop}}}(\hat{b} + \hat{b}^\dagger), \quad (6.9)$$

$$\hat{z} = \sqrt{\frac{\hbar}{4m\omega_{zop}}}(\hat{c} + \hat{c}^\dagger), \quad (6.10)$$

$$\hat{p}_x = i\sqrt{m\hbar\omega_{xop}}(\hat{a} - \hat{a}^\dagger), \quad (6.11)$$

$$\hat{p}_y = i\sqrt{m\hbar\omega_{yop}}(\hat{b} - \hat{b}^\dagger), \quad (6.12)$$

$$\hat{p}_z = i\sqrt{m\hbar\omega_{zop}}(\hat{c} - \hat{c}^\dagger), \quad (6.13)$$

where  $\hat{a}^\dagger$ ,  $\hat{b}^\dagger$  and  $\hat{c}^\dagger$  ( $\hat{a}$ ,  $\hat{b}$  and  $\hat{c}$ ) are the creation (annihilation) operators for the motional modes along  $x$ ,  $y$  and  $z$  directions, respectively. We obtain the following

expression,

$$\begin{aligned}
H = & \hbar\omega_{xop}(\hat{a}\hat{a}^\dagger + \frac{1}{2}) + \hbar\omega_{yop}(\hat{b}\hat{b}^\dagger + \frac{1}{2}) + \hbar\omega_{zop}(\hat{c}\hat{c}^\dagger + \frac{1}{2}) \\
& + \frac{\hbar\omega_{zop}}{8z_0} \sqrt{\frac{\hbar\omega_{zop}}{m}} \left( \frac{\hat{a}^{\dagger 2}\hat{c} + \hat{a}^2\hat{c}^\dagger + \hat{a}^2\hat{c} + \hat{a}^{\dagger 2}\hat{c}^\dagger + (2\hat{n}_x + 1)(\hat{c} + \hat{c}^\dagger)}{\omega_{xop}} \right. \\
& \left. + \frac{\hat{b}^{\dagger 2}\hat{c} + \hat{b}^2\hat{c}^\dagger + \hat{b}^2\hat{c} + \hat{b}^{\dagger 2}\hat{c}^\dagger + (2\hat{n}_y + 1)(\hat{c} + \hat{c}^\dagger)}{\omega_{yop}} \right) .
\end{aligned}$$

We are interested in the case where the frequency of radial mode along  $x$  direction is half of the frequency of the axial mode. Using the rotating wave approximation, we can finally write down Hamiltonian as follows,

$$\hat{H} = \hbar\omega_r\hat{a}^\dagger\hat{a} + \hbar\omega_s\hat{c}^\dagger\hat{c} + \frac{\hbar\Omega}{2} (\hat{a}^{\dagger 2}\hat{c} + \hat{a}^2\hat{c}^\dagger) , \quad (6.14)$$

where

$$\Omega = \frac{\omega_s}{4} \sqrt{\frac{\hbar\omega_s}{m\omega_r^2 z_0^2}} \quad (6.15)$$

is the mode coupling coefficient. The first two terms in Eq. 6.14 describe two independent harmonic oscillators that correspond to the axial and radial normal modes with the frequency  $\omega_s$  and  $\omega_r$ . The third term induces coupling between these two modes. This coupling is nonlinear in the sense that one phonon from the axial mode is converted into a pair of phonons in the radial mode and vice versa.

### 6.3 Experimental setup

The schematic of the experimental setup is shown in Fig. 6.1(a). Two  $^{171}\text{Yb}^+$  ions are confined in a four-rod linear rf-Paul trap with the single-ion secular frequencies

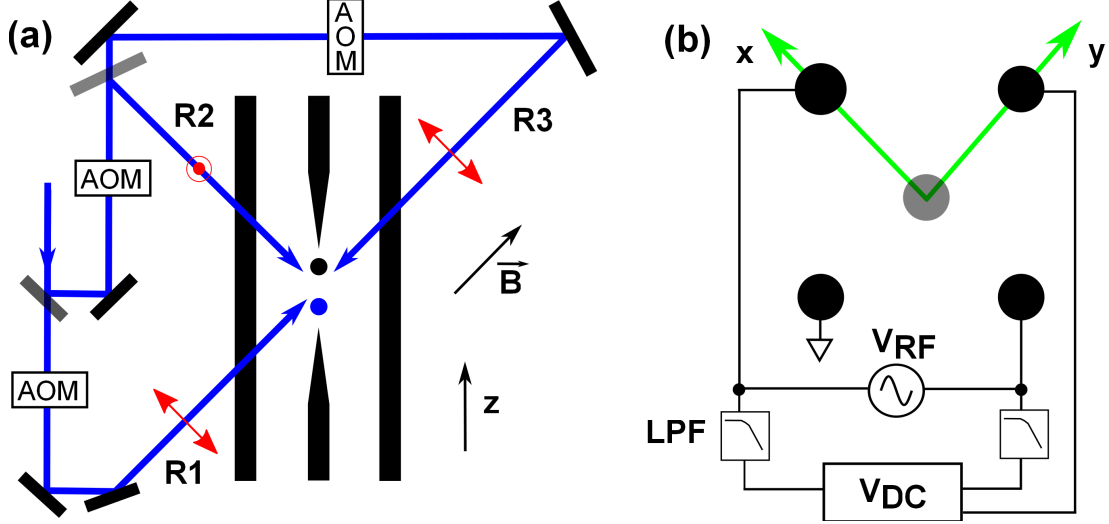


Figure 6.1: Experimental setup. (a) Schematic of the experimental setup. Three Raman beams are directed onto a two-ion crystal, such that R1 and R2 pair couples the motional states in axial direction, while the radial direction is addressed by R2 and R3 pair. The red arrows or dot inside a circle represent the polarization of each Raman beam. The magnetic field is parallel to the Raman beam R1 with the magnitude of 7.0 G. (b) Electrode configuration of the trap. The trapping frequencies in the  $x$  and  $y$  radial directions are offset from each other by adding small ( $\sim 0.5$  V) DC offset voltages to the  $x$  electrodes. The offset voltage along the  $x$  direction can be slowly changed between two values for each rod with the help of the low-pass RC filters (LPF) with time constants of 2 ms, or rapidly changed with time constants of 20  $\mu$ s. In both cases, the motional states of the ion crystal do not change [107; 114].

$(\omega_x, \omega_y, \omega_z) = 2\pi \times (0.99, 0.90, 0.75)$  MHz. In the beginning of the experiment, one of the ions is optically pumped to the metastable  $^2F_{7/2}$  state and does not interact with the laser beams. Only the internal spin of the other ion is addressed and probed in the remainder of the experiment. The optical pumping to the  $^2F_{7/2}$  state is achieved with two photons, one from the 369 nm Doppler cooling laser and the second at 386.8 nm from a broadband femtosecond modelocked pulsed laser that drives the ion from the  $^2P_{1/2}$  state to the  $(7/2, 2)_{3/2}$  state, from which the ion decays to the  $^2F_{7/2}$  state. This ion appears dark during the experiment

and the collective motion of the ion crystal is addressed by operation on the other ion, such as Doppler cooling and Raman sideband cooling by the mode-locked pulsed laser as described previously.

The Raman beams are produced by frequency doubling a 1.6 W laser light from a mode-locked Ti:Sapphire laser (pulse duration 3 ps, repetition rate 76 MHz). The frequency-doubled light has the central wavelength of 374 nm and power of 250 mW. It is split into three beams, sent through separate acousto-optical modulators (AOMs) and eventually focused to a beam waist of 15  $\mu\text{m}$  at the ion position as shown in Fig. 6.1(a). The Raman beam R1 and R2 form  $45^\circ$  and  $135^\circ$  angles respectively with the z-axis, while R3 is counter propagating to R1. The polarizations of the R1 and R2 beams are linear and mutually orthogonal, and R3 beam polarization is parallel to that of R1 (see Fig. 6.1(a)). This configuration allows independent addressing of both axial and radial modes of motion.

For the experiments described in this chapter, a PID control loop is used to actively stabilize the radial trapping frequency (see Fig. 6.2). The pick-up coil is positioned outside the vacuum chamber and approximately 6 cm away from the trap to pick up rf signal from the trap. After frequency filtering with a band-pass filter (Mini Circuits, SXBP-29) and power amplification with a RF amplifier (Mini Circuits, ZHL-2-8), the pick-up signal is measured by a RF power detector. The output DC voltage is stabilized by a PID controller which controls the rf power sent into the trap with a variable attenuator (Mini Circuits, ZX73-2500-s+). The high-frequency noise in the PID output is filtered out by a homemade low-pass RC filter with the cutoff frequency of  $\sim 10$  Hz. For better performance, the temperatures of the variable attenuator, the helical resonator, the amplifier of the pick-up signal and the power detector are stabilized to the level of a few millikelvins. The systematic radial frequency drift after the rf power stabilization

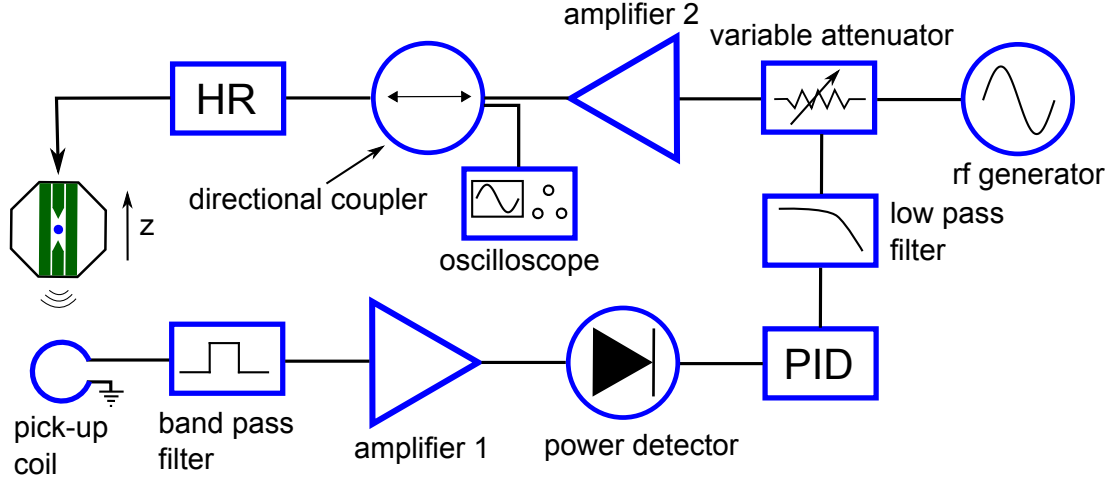


Figure 6.2: Schematic to stabilize the radial trapping frequencies. A pick-up coil with diameter of  $\sim 5$  cm is positioned  $\sim 6$  cm away from the trap. The pick-up signal goes through a band-pass filter and a RF amplifier before it is measured by a RF power detector. The output of the power detector is actively stabilized by a PID controller that controls the rf power sent into trap with a variable attenuator. The temperatures of the variable attenuator, the helical resonator, the amplifier of the pick-up signal and power detector are stabilized to the level of a few millikelvins.

is less than 200 Hz/hour. The axial trapping frequency is controlled by the DC voltages applied to the trap needles and has negligible systematic drift.

After the radial trapping frequencies are stabilized, we measure the coherence time of the radial phonon with the Ramsey-type experiment [119]. We create a superposition of the motional states  $|0\rangle + |1\rangle$  by a  $\pi/2$  pulse on the carrier transition followed by a  $\pi$  pulse on the red sideband. After some waiting time, the superposition of motional states is mapped back to the superposition of internal states by a  $\pi$  pulse on the red sideband followed by a  $\pi/2$  pulse on the carrier transition. The internal state of the ion can be detected with the standard fluorescence techniques. The Ramsey pattern can be obtained by varying the relative phase between these two  $\pi/2$  pulses on the carrier transition <sup>1</sup>. The

<sup>1</sup>The phases of the Raman pulses are determined by the phases of the rf signals sent to the

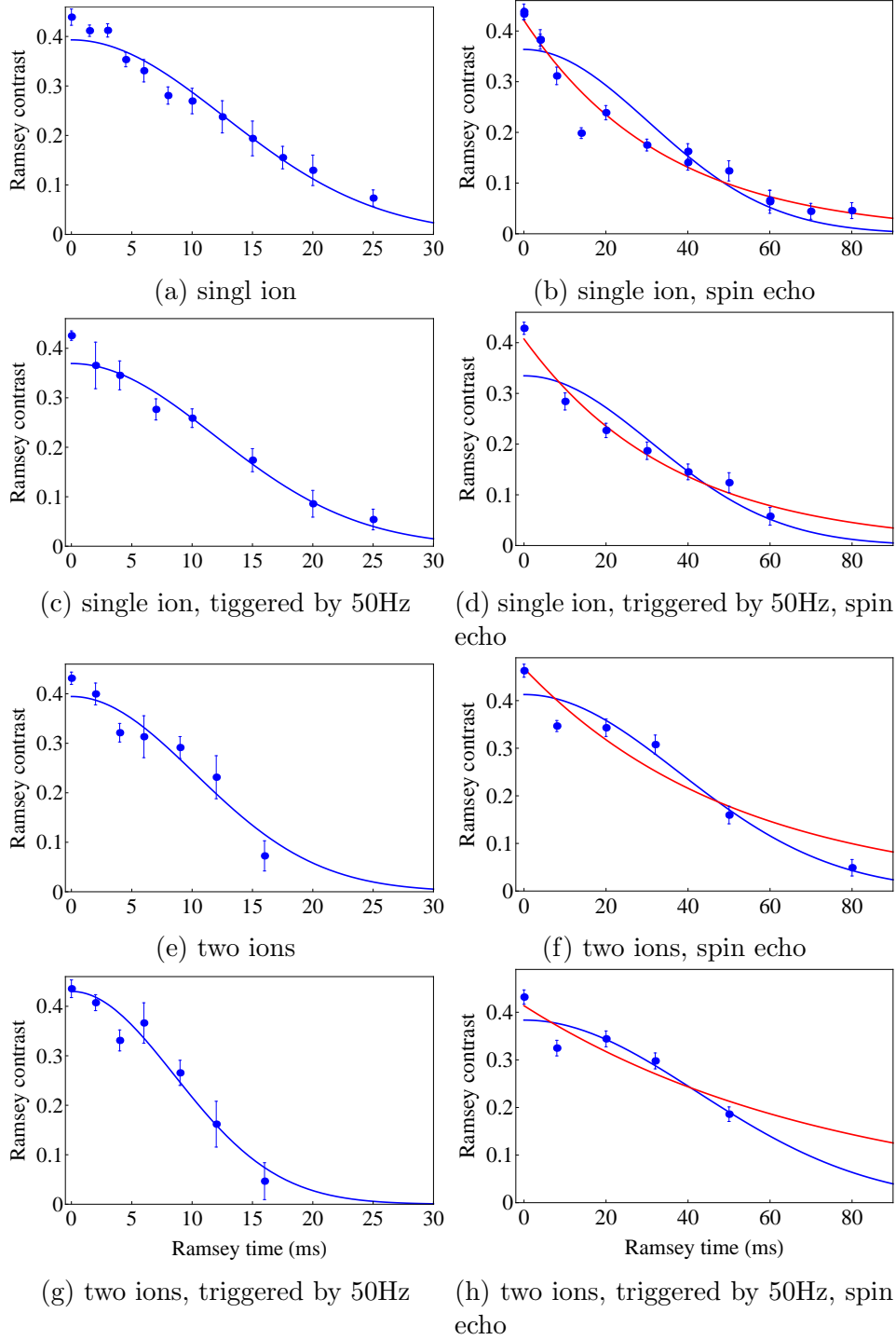


Figure 6.3: The coherence times of the phonons in the radial mode of single ion and the radial out-of-phase mode of two ions. The experimental data (blue dots) are fit with the Gaussian function (blue curves) and the exponential function (red curves).

coherence time of the phonon is extracted from the plot of the Ramsey contrast as a function of the waiting time during the Ramsey experiment.

We measure the coherence times of the phonons in the radial mode of a single ion and the radial out-of-phase mode of two ions with this method. In order to eliminate the influence due to the possible modulation of the radial trapping frequencies at the mains power supply frequency (50 Hz), we also try to trigger the experiment sequences with a signal from the mains. The results are shown in the left column of Fig.6.3. We fit the experimental data with the Gaussian function and extract the coherence times as listed in the Table 6.1. We can see that triggering the experiment sequences with the mains does not increase the coherence times of the phonons, indicating that modulation of the radial trapping frequencies at the frequency of the mains is not the main reason that causes the dephasing. This is consistent with the fact that the data is fitted well by the Gaussian function, which suggests that the noise spectrum has a Gaussian distribution.

In order to understand the dephasing mechanism better, the spin echo experiments are performed on the motional superposition states. The populations of states  $|0\rangle$  and  $|1\rangle$  are swapped in the middle of the Ramsey experiments described above by applying a  $\pi$  pulse on the carrier transition sandwiched between two red sideband  $\pi$  pulses. Similarly, the Ramsey contrasts are measured. The experimental data and the fits are shown in the right column of Fig.6.3. The Ramsey contrasts take around three times longer to decay. This implies that the radial trapping frequencies are relatively stable over the duration of a single experiment but fluctuate from experiment to experiment. We also note that the decay of the Ramsey contrasts in the case of single ion is better approximated by Raman AOMs.

coherence time (ms)		no spin echo	spin echo
single ion	no 50Hz trigger	12.6 (0.5)	34 (2)
	with 50Hz trigger	11.8 (0.6)	36 (3)
two ions	no 50Hz trigger	10.2 (0.9)	38 (4)
	with 50Hz trigger	8.5 (0.6)	42 (6)

Table 6.1: Coherence times of the radial phonons.

an exponential function than the Gaussian function while it is the other around in the case of two ions. The reason that causes this difference is still unknown.

## 6.4 Phonon evolution at resonance

Without the coupling term  $\hat{H}_c$ , or  $\Omega = 0$ , the Hamiltonian described by Eqn. 6.14 will simply characterize two independent harmonic oscillators with frequencies  $\omega_a$  and  $\omega_r$  respectively. We call the corresponding eigenstates the “bare states”. Fig. 6.4 shows the energy diagram of the bare states with  $\omega_a \sim 2\omega_r$ . We label the state with  $m$  axial phonons and  $n$  radial phonons as  $|m_a, n_r\rangle$ . All the states  $|m_a, n_r\rangle$  with  $2m + n$  equal to each other have similar energies. Moreover, they are degenerate when the resonance condition  $\omega_a = 2\omega_r$  is satisfied. It results in manifolds of degenerate states with degeneracy of  $\lfloor \frac{2m+n}{2} \rfloor$  for each state, where  $\lfloor \cdot \rfloor$  means floor function of a real number. We refer the degenerate manifold as the  $i$ -th manifold if it contains the state  $|0_a, i_r\rangle$ .

However, if the coupling term  $\hat{H}_c$  is included, these degeneracies are lifted. By scanning the detuning  $\delta = 2\omega_r - \omega_a$ , we will see an avoided crossing. This is experimentally verified as shown in Fig. 6.7 in the next section. The avoided crossing in every manifold of states enables us to perform a single-shot parity measurement which eventually leads to a simple way to directly measure the Wigner function of the radial motional mode. It also finds applications in cooling

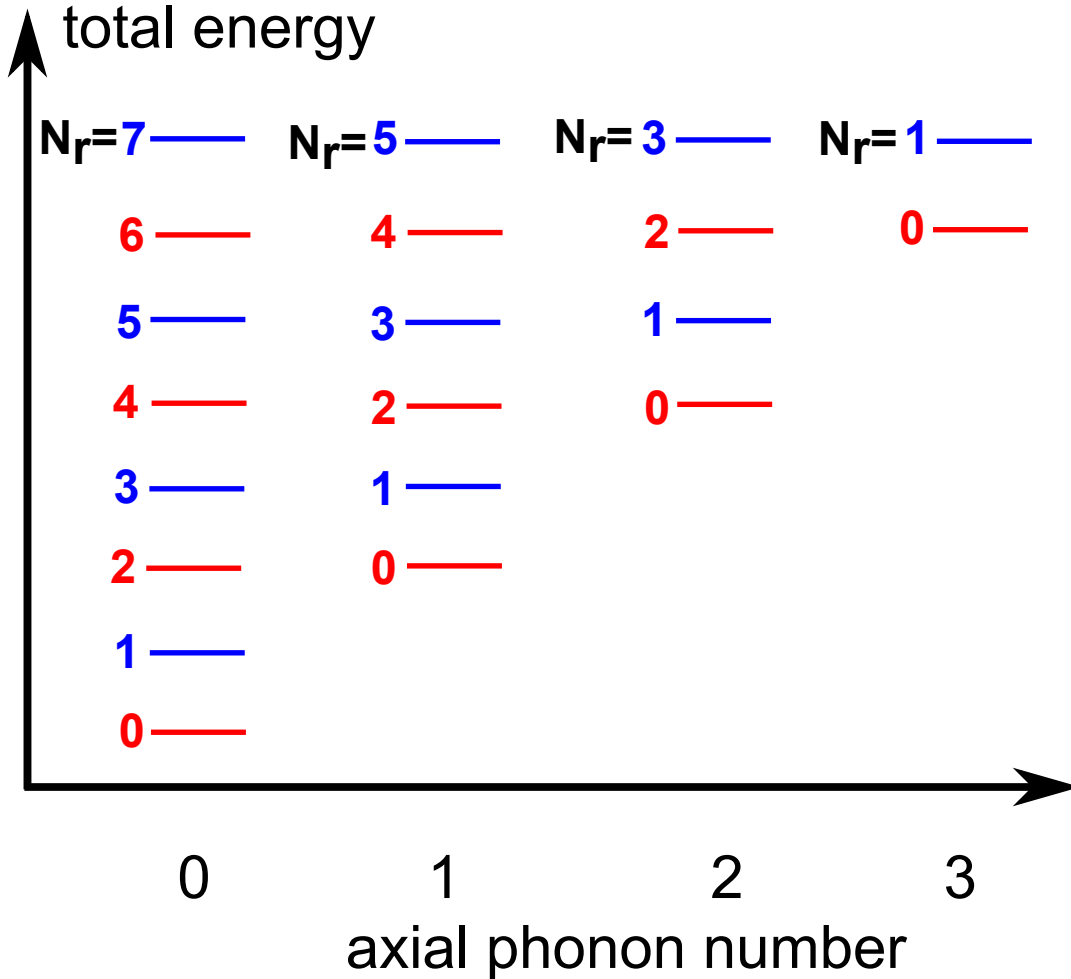


Figure 6.4: The energy diagram without considering the coupling term. The number at the horizontal axis represents the phonon number of the axial mode while the number displayed vertically is the phonon number of the radial mode. The states belonging to the  $i$ -th manifold with  $i$  the even number are represented by red lines, otherwise they are represented by blue lines.

of optically inaccessible mode. We will discuss these applications latter.

### 6.4.1 Phonon up and down conversion

It is also noted that the coupling term  $\hat{H}_c$  only couples the state with its neighboring states in the same manifold. Mathematically, it means  $\hat{H}_{cm,n;u,v}$  is nonzero

only when

$$\begin{aligned} u &= m \pm 1 , \\ 2m + n &= 2u + v , \end{aligned} \quad (6.16)$$

where  $\hat{H}_{cm,n;u,v} = \langle m_a, n_r | \hat{H}_c | u_a, v_r \rangle$  are the coupling matrix elements. Inserting the expression  $\hat{H}_c = \hbar\Omega/2 (\hat{a}^\dagger \hat{c} + \hat{a} \hat{c}^\dagger)$ , we obtain:

$$\begin{aligned} \langle m_a, n_r | \hat{H}_c | m + 1_a, n - 2_r \rangle &= \langle m + 1_a, n - 2_r | \hat{H}_c | m_a, n_r \rangle \\ &= \frac{\hbar\Omega}{2} \sqrt{(m + 1)(n - 1)n} , \end{aligned} \quad (6.17)$$

where  $m \geq 0$  and  $n \geq 2$ .

One special case is the coupling between  $|0_a, 2_r\rangle$  and  $|1_a, 0_r\rangle$  states. The matrix element of the Hamiltonian with respect to these states is

$$\langle 0_a, 2_r | \hat{H}_c | 1_a, 0_r \rangle = \frac{\hbar\Omega}{2} \sqrt{2} . \quad (6.18)$$

It characterizes the oscillation frequency of motional excitation between the axial and radial modes if we initially prepare the system in the state  $|0_a, 2_r\rangle$  or  $|1_a, 0_r\rangle$ .

To verify the nonlinearity of the coupling at single phonon level, we first cool all motional modes to their ground state, keeping the detuning  $\delta = 35$  kHz from resonance. From the motional ground state, we add either one or two phonons to the radial mode by applying either a single  $\pi$ -pulse on the blue sideband, or a sequence of  $\pi$ -pulses on the blue sideband, carrier and blue sideband again. We then change DC voltage applied to the rods of the trap, with the time constants of the low pass filters (LPFs) of 20  $\mu$ s as shown in Fig. 6.1(b), to bring the

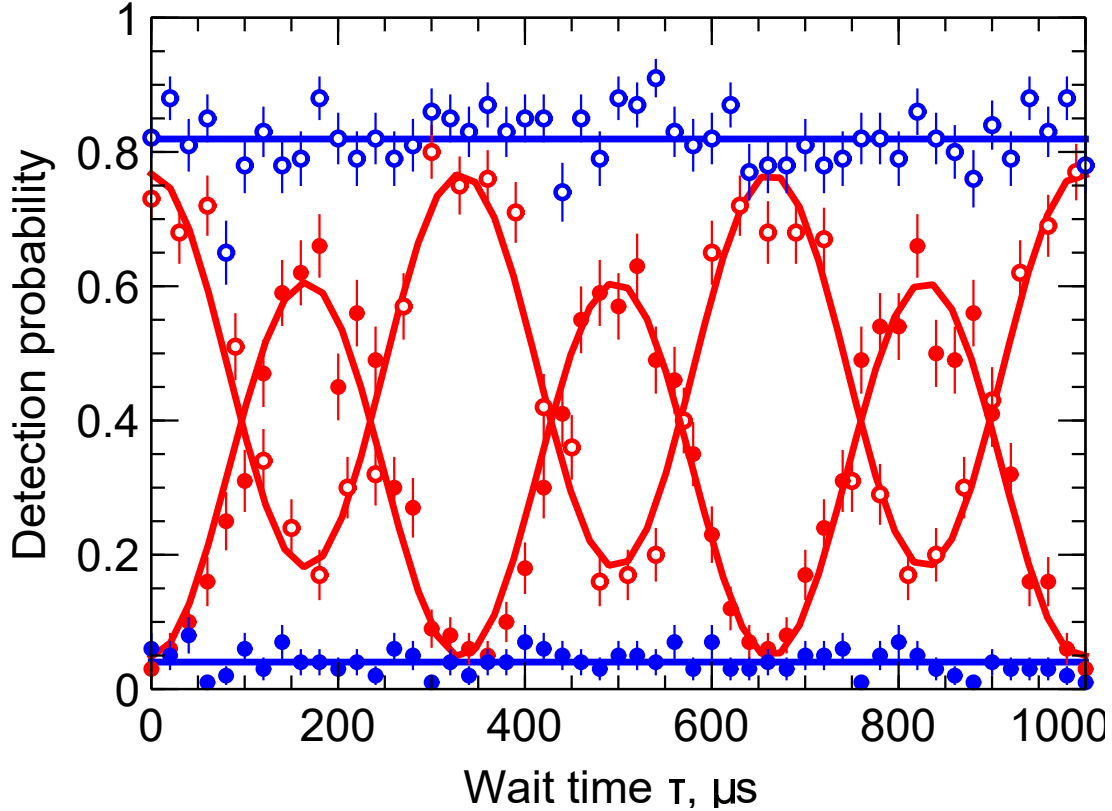


Figure 6.5: Phonon state evolution in the axial (solid dots) and radial (open circles) modes, where either one (blue) or two (red) phonons being added to the radial direction. The sinusoidal fit (red line) reveals the coupling rate of  $3.02 \pm 0.02$  kHz. The straight fit lines show that there is negligible coupling between the modes when only one radial phonon is present.

detuning  $\delta$  to zero. The rate of trapping frequency change is much smaller than the trapping frequency such that the adiabaticity condition is satisfied and we do not see any change in the motional states [107; 114]. The system evolves for some time  $\tau$  before we bring the detuning back to the initial value and check for the presence of phonons in the axial or radial mode. The results are presented on Fig. 6.5.

We observe the energy oscillations back and forth between the axial and radial modes only when the radial mode is initially prepared in the two-phonon

state. The measured oscillation frequency  $3.02 \pm 0.02$  kHz is compatible to the frequency  $\sqrt{2}\Omega/2\pi = 2.96$  kHz predicted by Eq. 6.15. The reduced visibility of the oscillation together with small deviation of the measured coupling strength from the theory can be attributed to the deviation from the resonance condition, which is compatible with the observed frequency drifts. This process is analogous to the process of up and down-conversion of photons in nonlinear crystals. However, unlike the optical case where number of pump photons required to produce one photon pair is usually large[69], the coupling strength here is high and the effect can be readily observed even for single phonon Fock states.

## 6.5 Adiabatic sweep

### 6.5.1 Adiabatic state evolution

As mentioned previously, the coupling between axial mode and radial mode lifts the degeneracy at the resonance. In a certain otherwise degenerate manifold of states, the coupling term mixes all the bare energy eigenstates and forms new energy eigenstates that are superposition of all the states in this manifold. It leads to the avoided crossing in the energy spectrum if we scan the detuning  $\delta$  across the resonance. We calculate the eigenenergy of total Hamiltonian described by Eqn. 6.14. The avoided crossing behavior for the 2nd, 3rd, 4th, 5th, 6th, 7th manifolds is shown in Fig. 6.6 (a)–(f).

In order to further quantify the coupling between different modes, we experimentally verify the avoided crossing in the 2nd manifold in the energy spectrum. We scan the detuning  $\delta$  across the resonance, by changing the radial mode frequency with the DC voltage offset while keeping the axial mode frequency fixed.

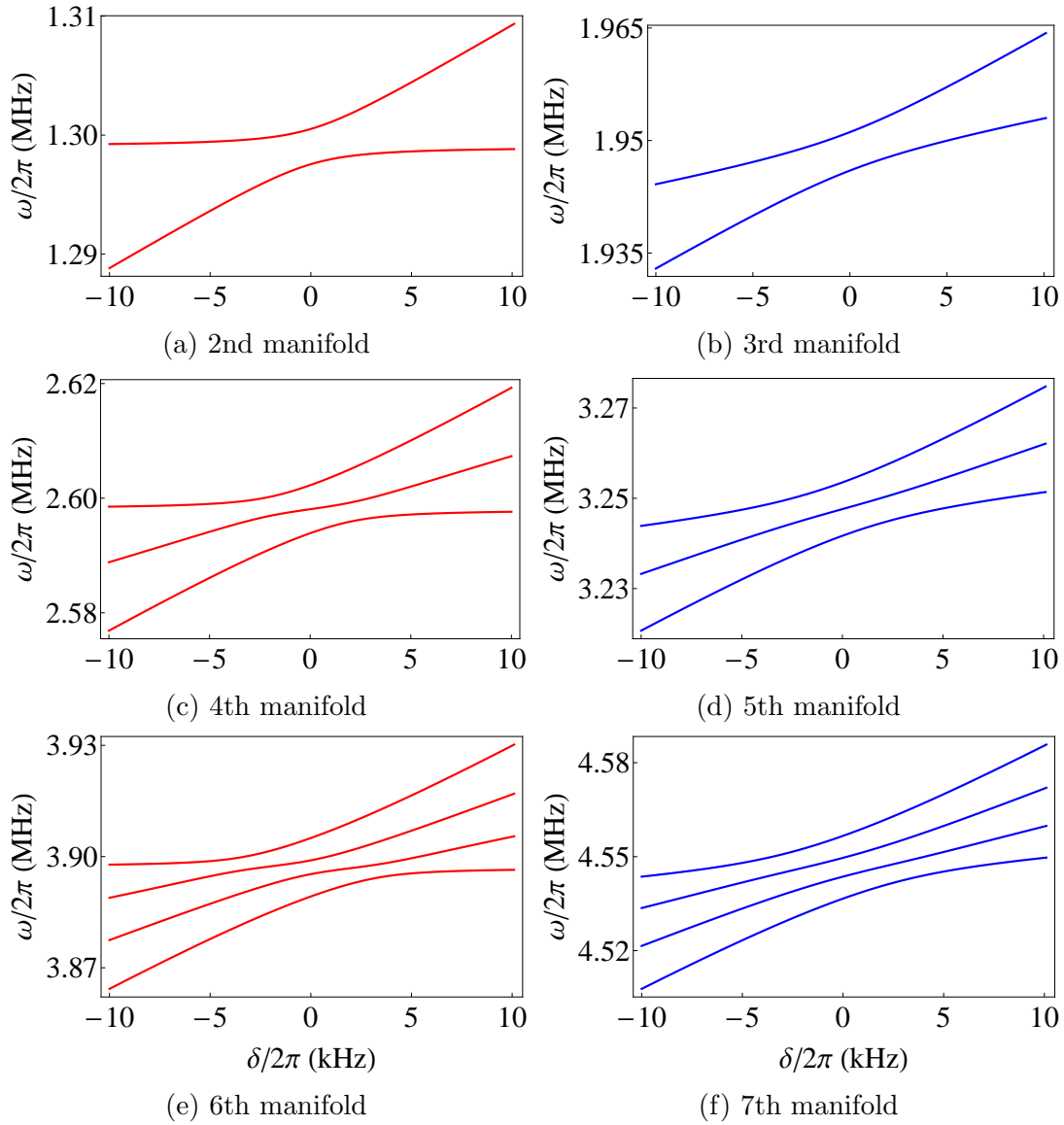


Figure 6.6: Avoided crossing for different manifolds of states. The lowest and highest energy eigenstates are particular interesting for the motional excitation swap as explained in the text.

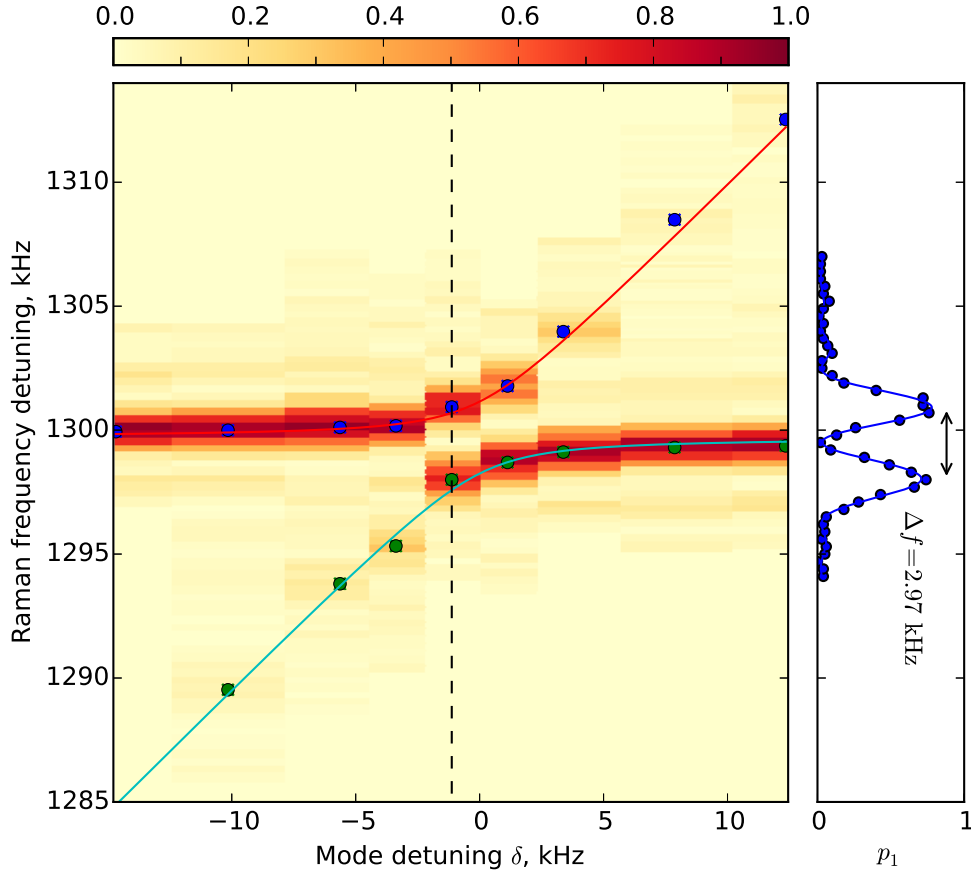


Figure 6.7: Avoided crossing of the axial mode, measured after sideband cooling. The left plot shows the probability  $p_1$  to find an ion in state  ${}^2S_{1/2} |F = 1, m = 0\rangle$  as a function of the detuning  $\delta = 2\omega_r - \omega_s$  from the resonance condition, and a Raman detuning  $\Delta$  from the  ${}^2S_{1/2} |F = 0, m = 0\rangle \rightarrow {}^2S_{1/2} |F = 1, m = 0\rangle$  carrier transition. We extract the coupling strength by measuring the mode splitting at resonance, as shown on the right plot. The measurement yields the splitting between modes to be  $2.97 \pm 0.03$  kHz.

We measure the mode spectrum for axial modes after sideband cooling. The results are shown in Fig. 6.7.

The lowest and highest energy eigenstates are particularly interesting for the adiabatic swap of the motional excitation. When the detuning is much bigger than the coupling strength, for  $2\omega_r < \omega_a$  ( $2\omega_r > \omega_a$ ), the lowest (highest) energy

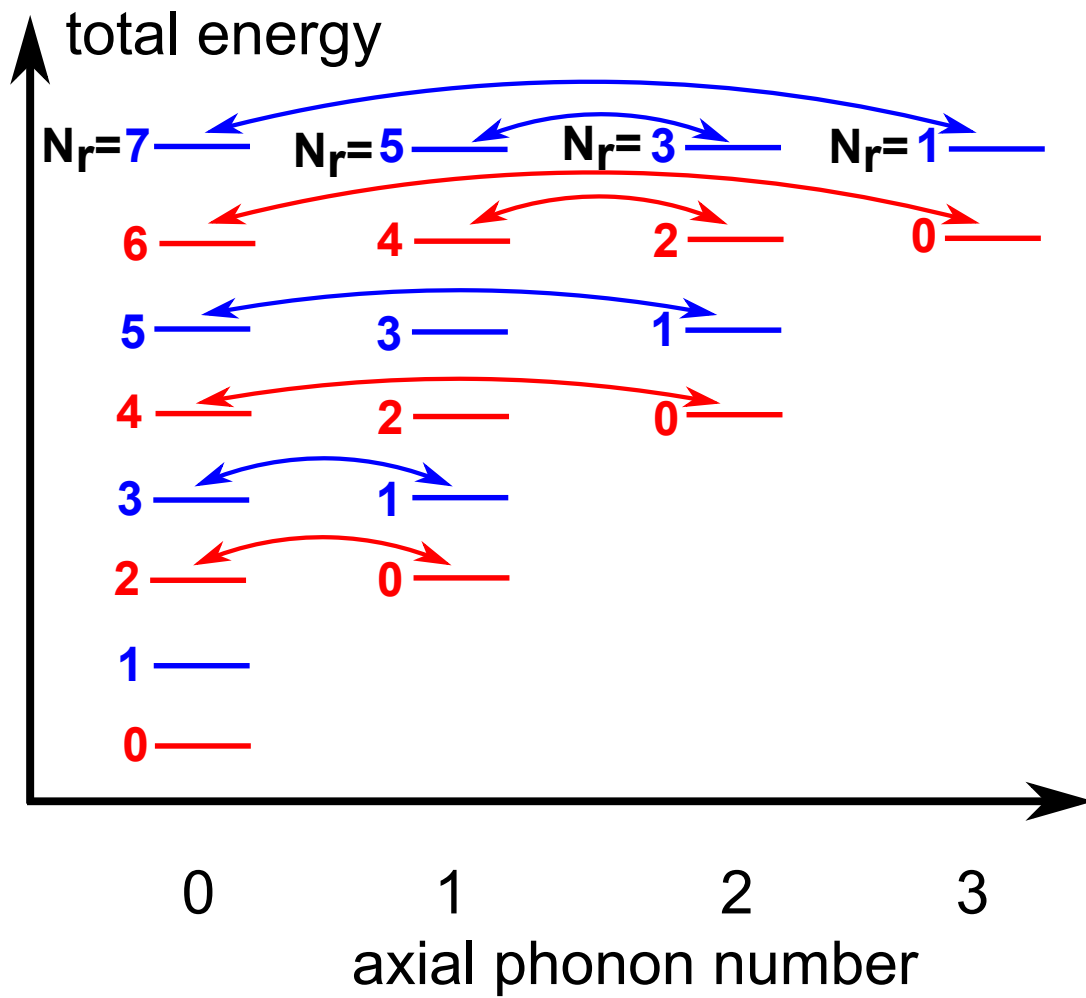


Figure 6.8: Adiabatic evolution of phonon states between the radial and axial modes

eigenstates are approximately the bare energy eigenstates with axial mode in vacuum state, while the highest (lowest) energy eigenstates are approximately the bare energy eigenstates with lowest possible radial mode excitation, i.e.  $n_r = 0$  and  $n_r = 1$  for  $2n$ -th and  $(2n+1)$ -th manifolds, respectively. Suppose the detuning  $\delta$  changes at a rate much slower than the coupling strength  $\Omega$ , i.e.

$$\dot{\delta} \ll \Omega . \quad (6.19)$$

The system remains in the energy eigenstate as it evolves, leading to the adiabatic evolution of phonon states between the radial and axial modes. For example, the lowest energy eigenstate for  $\omega_s > 2\omega_r$ , i.e.  $|n_r\rangle|0_a\rangle$ , will evolve into the lowest energy eigenstate for  $\omega_s < 2\omega_r$ . The latter eigenstate is  $|0_a\rangle|n/2_r\rangle$  for even  $n$  and  $|1_r\rangle|(n_r - 1)/2_a\rangle$  for odd  $n$ , which allows us to determine the parity of  $n$ .

This adiabatic sweep can find applications in the cooling of an optically inaccessible mode and a direct measurement of the Wigner function as shown below.

### 6.5.2 Cooling of optically inaccessible mode (OIM)

The control of ions' motional states is usually realized by coupling them to the ions' internal states with lasers. This coupling essentially comes from the projection of the momentum of the photons from the laser light along the direction of the ions' motion. In order to manipulate and detect the motional states of a certain mode, the direction of interest must be optically accessible. This requirement is one of the main concerns during the design of the trap, especially for the microtrap, surface trap and the cryogenic trap.

Cross-mode coupling offers a possible way to control the optically inaccessible mode (OIM) indirectly. This coupling bridges the gap between the lasers and

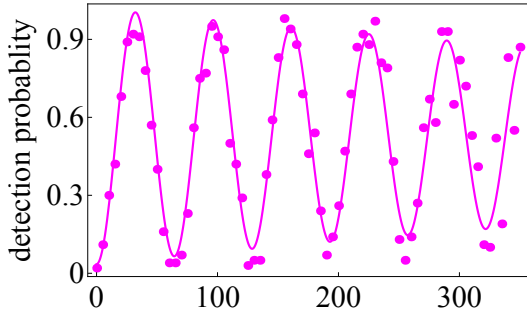
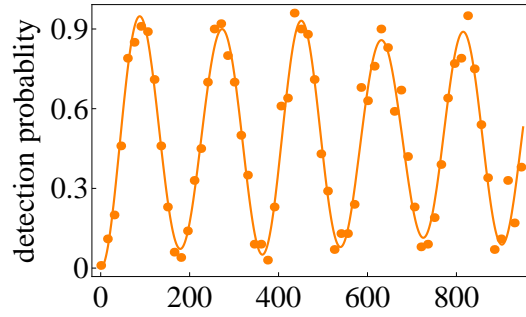
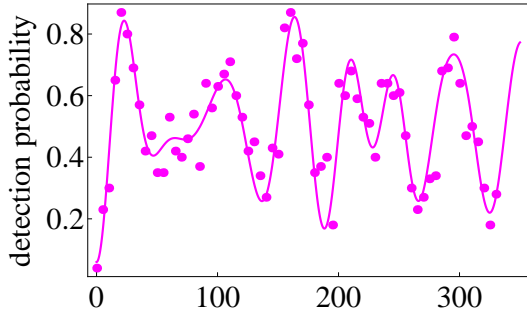
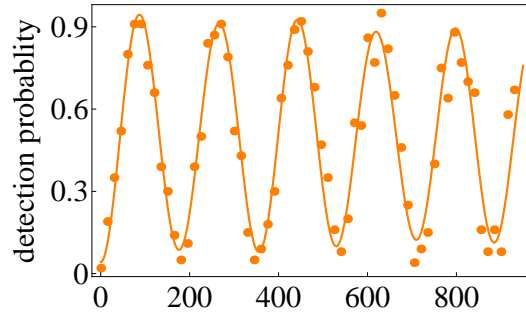
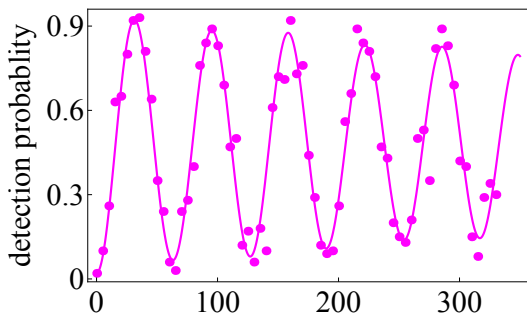
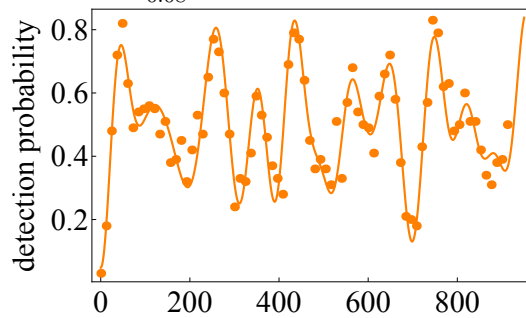
the OIM via a mode that can be coupled directly to the lasers. We note that the cross-mode coupling has been realized in a Paul trap [39] and a Penning trap [21] by applying an oscillating electric field with frequency equal to the frequency difference between two modes. Here we demonstrate the cooling of the axial out-of-phase mode close to ground state by making use of its coupling to radial out-of-phase mode.

As the first step, we try to demonstrate that all the motional excitation in the axial mode can be adiabatically transferred to the radial mode by a slow sweep of the radial trapping frequency, i.e. the detuning. It is done in the following steps:

- First, we cool down both modes to ground state at detuning of  $-35$  kHz.
- Second, we coherently excite the axial mode with an oscillating dipole force with frequency matching the axial trapping frequency. This force is generated by a running optical lattice [31].
- Third, we adiabatically sweep the detuning from  $-35$  kHz to  $35$  kHz by slowly changing the DC voltages applied to the rods of the trap, with LPFs' time constants of  $2$  ms as shown in Fig. 6.1(b).
- Fourth, the detuning is swept back from  $35$  kHz to  $-35$  kHz.

After each step, we extract the phonon distributions of both modes by probing the evolution of the internal state of the ion at the blue sidebands [95]. The results are shown in Fig. 6.9 with magenta and orange dots representing the axial and radial modes, respectively. We fit the (a), (b), (d), (e), (h) with a superposition of decaying sinusoidal functions and (c), (g) with Poisson distribution:

$$P_n = \frac{\bar{n}^n e^{-\bar{n}}}{n!} . \quad (6.20)$$

(a) sideband cooling,  $P_0 = 1.00^{+0.00}_{-0.04}$ (b) sideband cooling,  $P_0 = 0.94 \pm 0.06$ (c) coherent excitation of axial mode,  $\bar{n} = 0.94 \pm 0.08$ (d) coherent excitation of axial mode,  $P_0 = 0.96^{+0.04}_{-0.08}$ (e) adiabatic sweep,  $P_0 = 0.98^{+0.02}_{-0.03}$ (f) adiabatic sweep,  $2\bar{n} = 2.2 \pm 0.1$

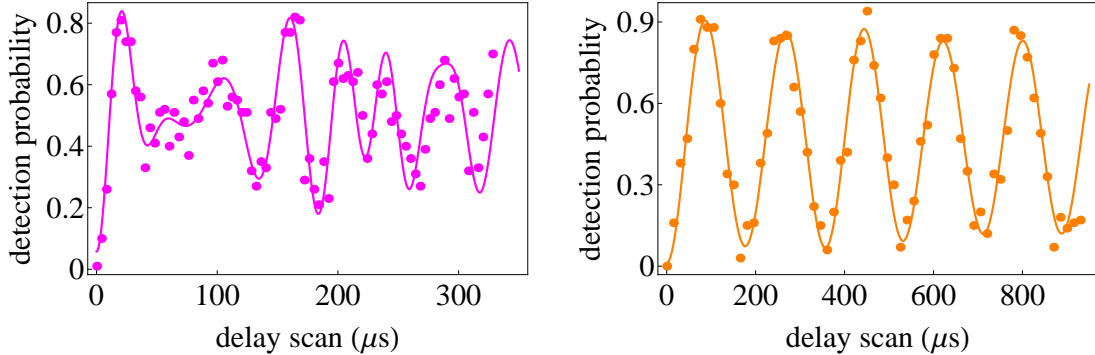
(g) adiabatic sweep back,  $\bar{n} = 1.19 \pm 0.09$ (h) adiabatic sweep back,  $P_0 = 0.95^{+0.05}_{-0.08}$ 

Figure 6.9: Blue-sideband evolutions of the axial (magenta) and radial (orange) motional modes after sideband cooling of all six modes (a, b), followed by coherent excitation of the axial mode (c, d), adiabatical scanning of the detuning from  $-35\text{kHz}$  to  $35\text{kHz}$  (e, f), and scanning of detuning back to  $-35\text{kHz}$ . Each data point represents an average of 100 measurements.

Since every phonon in the axial mode will be down-converted into two phonons in the radial mode after the third step, the phonon distribution of the radial mode will contain only the even number, i.e.

$$P_n = \begin{cases} \frac{\bar{n}^{\frac{n}{2}} e^{-\bar{n}}}{(\frac{n}{2})!}, & \text{if } n \text{ is even number;} \\ 0, & \text{if } n \text{ is odd number.} \end{cases} \quad (6.21)$$

We fit Fig. 6.9(f) with this distribution.

As expected, both motional modes are in ground state with very high probability after sideband cooling, as shown in Fig. 6.9(a, b). Fig. 6.9(c, d) shows that the axial mode evolves into a coherent state while the radial mode still remains in the vacuum state after coherently exciting the axial mode with the classical force. Motional excitation of the axial mode is completely transferred to the radial mode, leaving the axial mode in vacuum state, after adiabatically scanning the detuning across the resonance, as shown in Fig. 6.9(e, f). Scanning the ra-

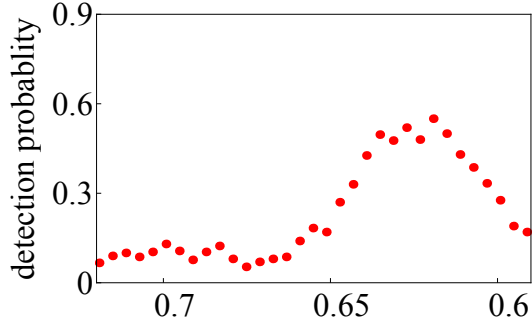
dial frequency back also brings the motional excitation back to the axial mode, as indicated by the highly occupied vacuum state in the radial mode as shown in Fig. 6.9(h) and the close fit of the distribution of the phonon number to the Poisson distribution in the axial mode as shown in Fig. 6.9(g). These facts confirm that the adiabaticity condition Eqn. 6.19 is very well satisfied.

We would like to point out that the coherence between the Fock state components has been lost after an adiabatic sweep of the detuning since the sweep itself takes around 9ms, which is comparable to the coherence time of the phonon in the radial mode.

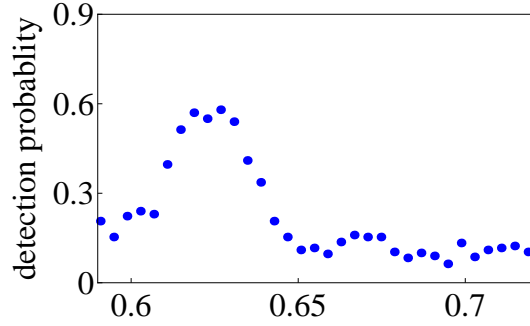
To demonstrate the indirect cooling of the axial mode, we do the followings:

- First, Doppler cool the ion crystal.
- Second, apply the Raman sideband cooling sequence to the radial mode at the detuning of  $-35$  kHz.
- Third, sweep the detuning from  $-35$  kHz to  $35$  kHz by slowly changing the DC voltages applied to the rods of the trap, with LPFs' time constants of  $2$  ms as shown in Fig. 6.1(b).
- Forth, apply the Raman sideband cooling sequence to the radial mode for the second time.
- Fifth, sweep the detuning back from  $35$  kHz to  $-35$  kHz.

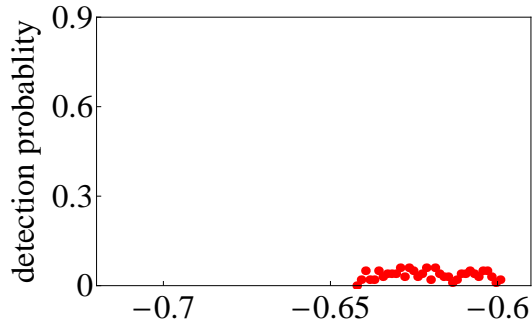
We scan the red and blue sidebands of both the axial and radial modes after each step. The results are show in Fig. 6.10 and Fig. 6.11 for radial sidebands and axial sidebands, respectively. As expected, both modes contain quite a few phonons after Doppler cooling (see Fig. 6.10(a, b) and Fig. 6.11(a, b)). We



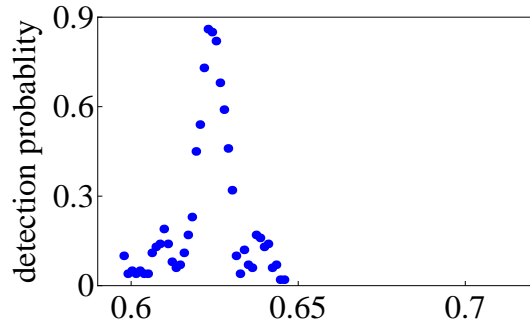
(a) Doppler cooling



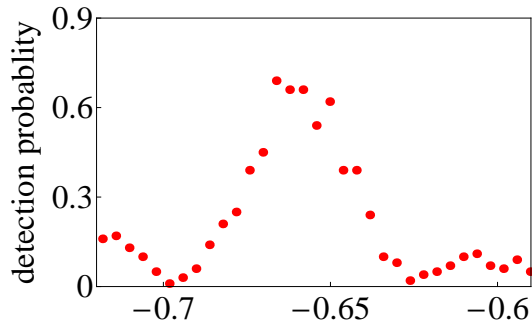
(b) Doppler cooling



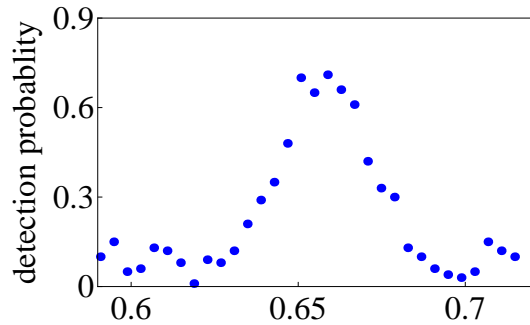
(c) radial sideband cooling



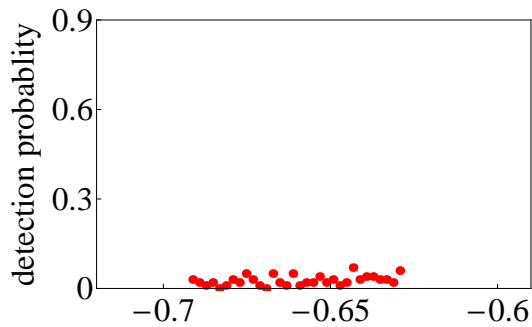
(d) radial sideband cooling



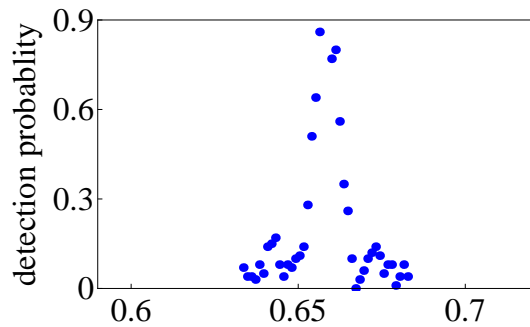
(e) sweep



(f) sweep



(g) second radial sideband cooling



(h) second radial sideband cooling

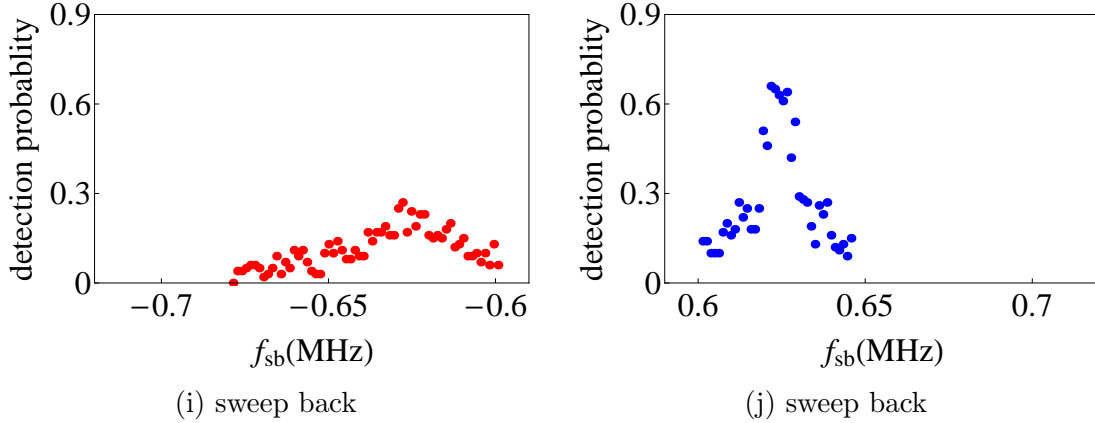
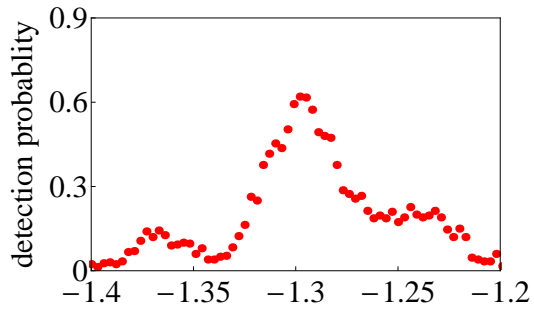


Figure 6.10: Radial red (red dot) and blue (blue dot) sidebands after Doppler cooling (a), (b); ground state cooling of radial mode (c), (d); adiabatic detuning sweep (e), (f); ground state cooling of radial mode again (g), (h); adiabatic detuning sweep back (i), (j).

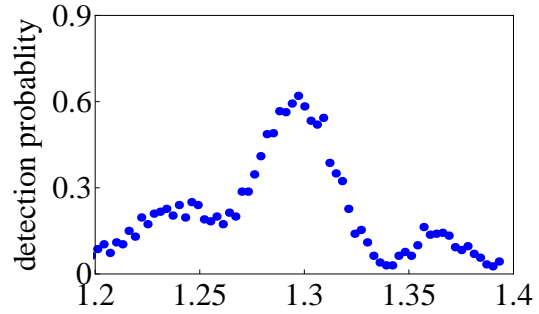
extract the phonon numbers to be  $n_a \sim 8$  and  $n_r \sim 16$  from the state evolutions at blue sidebands of both modes [95]. After the cooling steps stated above, the asymmetries of the red and blue sidebands as shown in Fig. 6.10(i, j) and Fig. 6.11(i, j) indicate the cooling of both modes. We estimate that the axial mode occupies the ground state with probability around 0.9. The radial mode occupies the ground state with lower probability. This is because the first radial sideband cooling sequence does not work well due to the coupling of radial mode with a “hot” axial mode, and the residual phonons together with the excitation of the axial mode owing to the scattering of photons during the optical pumping of the second radial sideband cooling sequence lead to a noticeable phonon occupation. For a better cooling of both modes, we can repeat the aforementioned steps.

### 6.5.3 Wigner function measurement

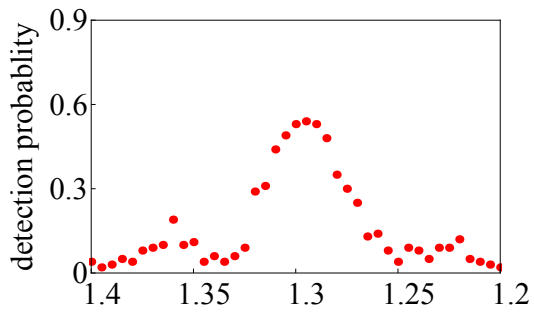
Classically, the state of a particle can be represented by a point in phase space with definite position and momentum. For an ensemble of particles, the proba-



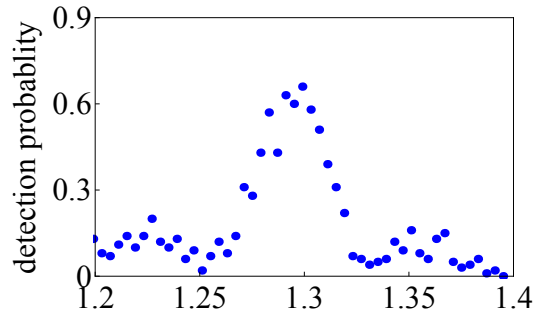
(a) Doppler cooling



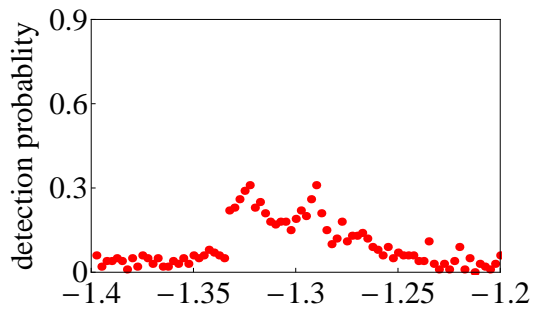
(b) Doppler cooling



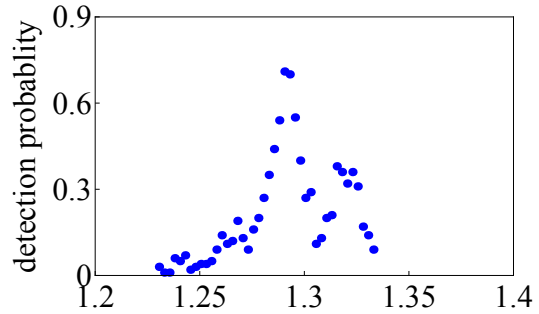
(c) radial sideband cooling



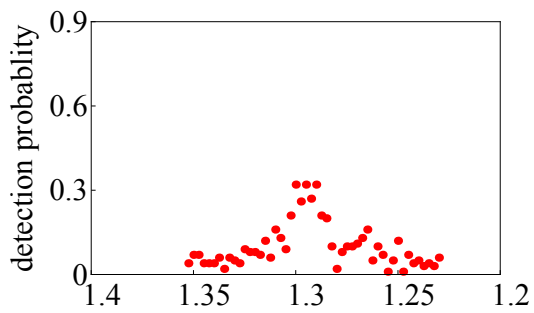
(d) radial sideband cooling



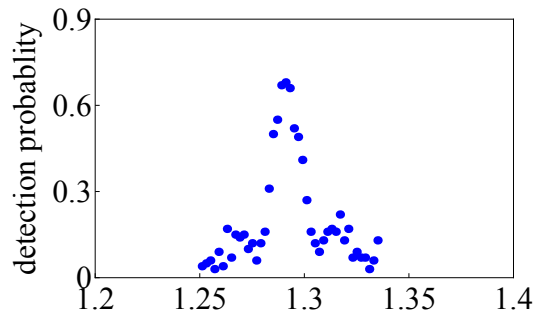
(e) sweep



(f) sweep



(g) second radial sideband cooling



(h) second radial sideband cooling

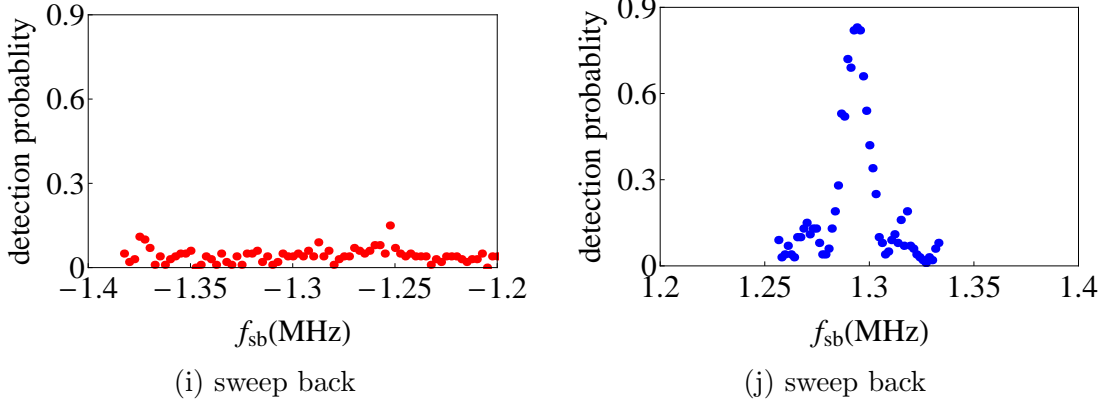


Figure 6.11: Axial red (red dot) and blue (blue dot) sidebands after Doppler cooling (a), (b); ground state cooling of radial mode (c), (d); adiabatic detuning sweep (e), (f); ground state cooling of radial mode again (g), (h); adiabatic detuning sweep back (i), (j).

bility of finding a particle at a certain point in the phase space is characterized by a probability distribution. Quantum mechanically, however, the position  $x$  and momentum  $p$  of a particle can not be well defined simultaneously. Thus, the real phase space probability distribution does not exist. Nevertheless, a quasiprobability distribution  $W(x, p)$  of state with density matrix  $\rho$  can be defined [149]:

$$W(x, p) = \frac{1}{\pi} \int_{-\infty}^{\infty} \langle x + \frac{u}{2} | \rho | x - \frac{u}{2} \rangle e^{-2ipu} du, \quad (6.22)$$

It is called Wigner function and it fully describes the quantum state of the system.

It was shown in [37; 90; 122] that the Wigner function corresponds to a directly measurable observable [8; 25; 74; 90; 140]

$$W(\alpha) = \frac{2}{\pi} \text{Tr}[D(-\alpha)\rho D(\alpha)\hat{P}],$$

where  $D(\alpha)$  is the displacement operator in phase space and  $\hat{P}$  is the parity

operator <sup>1</sup>. This formula suggests that the Wigner function at the point  $\alpha$  in phase space is equal to the expectation value of the parity operator in the state  $D(-\alpha)\rho D(\alpha)$ , which corresponds to a displacement of the state  $\rho$  by the amount  $-\alpha$  in phase space.

In our trapped-ion system, the displacement can be carried out by applying a force to the ion with controlled phase and duration. On the other hand, the direct parity measurement of the ion motional state is enabled by making use of the aforementioned nonlinear mode coupling. As described previously, when the detuning  $\delta$  is scanned across the resonance adiabatically, the lowest energy eigenstate for  $\omega_s > 2\omega_r$ , i.e.  $|n\rangle_r|0\rangle_a$ , will evolve into  $|0\rangle_r|n/2\rangle_r$  for even  $n$  and  $|1\rangle_r|(n_r - 1)/2\rangle_a$  for odd  $n$ . This means that the presence or absence of a phonon in the radial mode after the sweep provides information about the parity of the initial radial motional state. The phonon can be detected by mapping it onto the ion internal state and the expectation value of the parity operator can be extracted as  $\langle \hat{P} \rangle = (1 - 2p_1/\eta)$ , where  $p_1$  is the probability of finding the ion in the internal state  $|1\rangle$ , and  $\eta = 0.86$  is the overall phonon mapping efficiency in our setup. The value of the Wigner function can be obtained as  $W(\alpha) = 2\langle \hat{P} \rangle/\pi$ .

The Wigner function measurement protocol was tested on several quantum states including the vacuum state and coherent states (see Fig. 6.12), cat states (see Fig. 6.13) and Fock states (see Fig. 6.14). The measured Wigner functions are compared with the expected ones.

To prepare the coherent state shown in Fig.6.12(b, c), we start with all modes of the ion crystal cooled to the ground state of motion and the ion pumped to the  $|0\rangle \equiv {}^2S_{1/2} |F = 0, m_F = 0\rangle$  state. A microwave  $\pi$  pulse can transfer the ion to the  $|1\rangle \equiv {}^2S_{1/2} |F = 1, m_F = 1\rangle$  state. An optical lattice, formed by

---

<sup>1</sup>Its action on the Fock state  $|n\rangle$  is  $\hat{P}|n\rangle = (-1)^n|n\rangle$ .

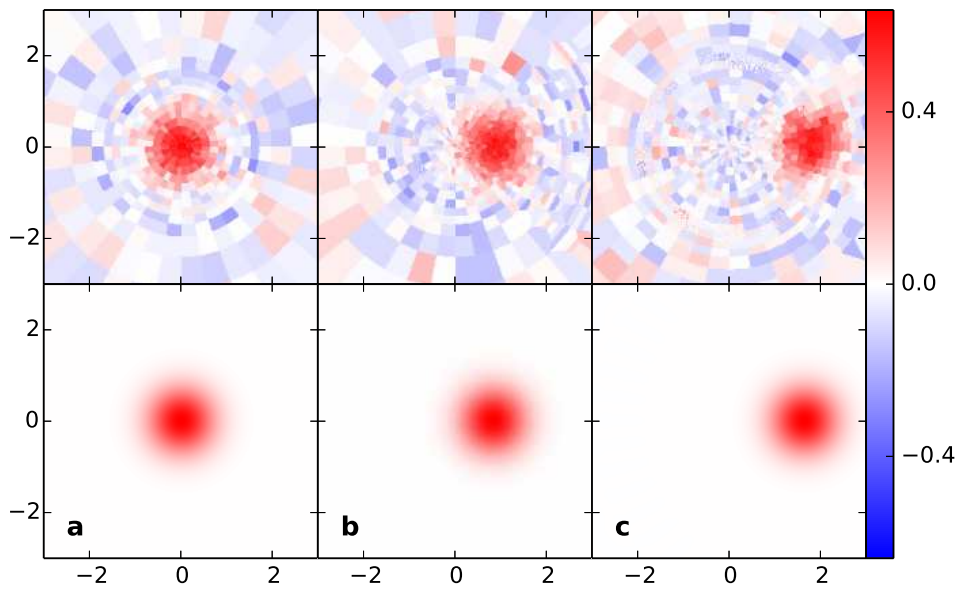


Figure 6.12: Wigner functions of the vacuum states (a) and the coherent states  $|\alpha\rangle$  with  $\alpha = 0.81$  (b) and  $1.63$  (c). The top row corresponds to the experimental data, while the bottom row shows calculated Wigner functions. Each data point represents an average of 100 experiments.

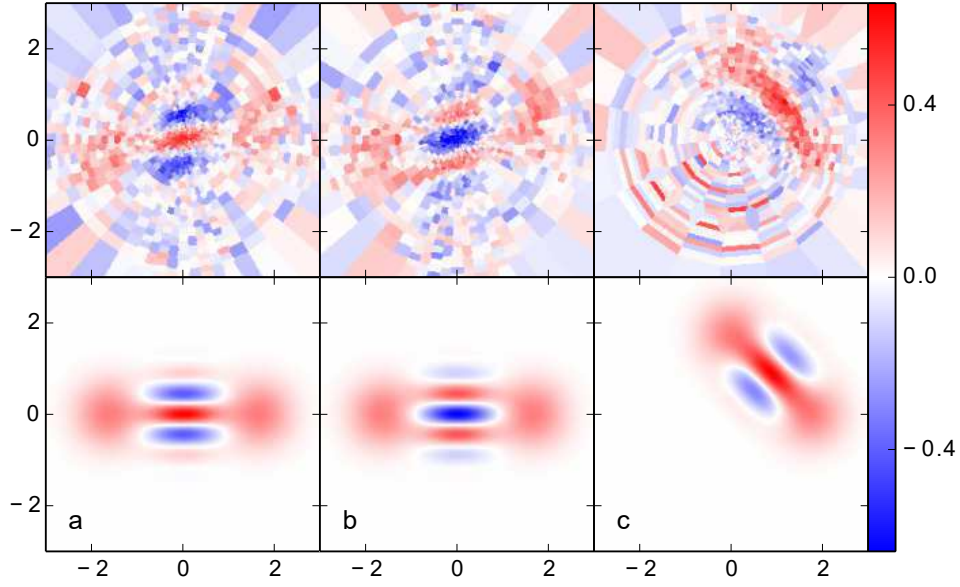


Figure 6.13: Wigner functions of the even Schrödinger cat state  $(|\alpha\rangle + |-\alpha\rangle)/\sqrt{2}$  (a), odd Schrödinger cat state  $(|\alpha\rangle - |-\alpha\rangle)/\sqrt{2}$  (b) and the Yurke-Stoler cat state  $(|\alpha\rangle - |i\alpha\rangle)/\sqrt{2}$  (c). The top row corresponds to the experimental data, while the bottom row shows calculated Wigner functions. Each data point represents an average of 50 experiments.

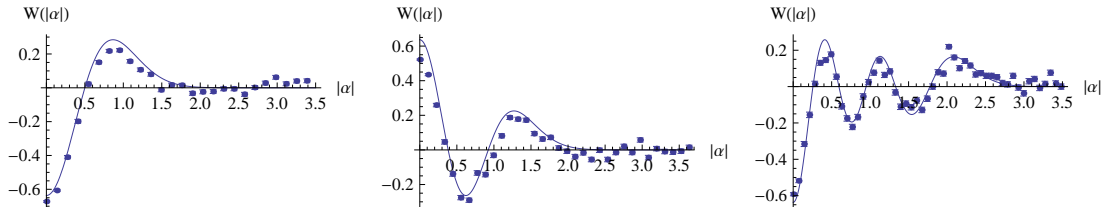


Figure 6.14: Wigner functions of the Fock states  $|n\rangle$  with  $n = 1, 2,$  and  $5$  phonons averaged over the phase of  $\alpha$ . The solid lines show the theoretical prediction  $W(|\alpha|) = 2(-1)^n e^{-2|\alpha|^2} L_n(4|\alpha|^2)/\pi$ ; the points are experimentally measured values. The error bars show  $1\sigma$  statistical uncertainty.

the  $R2$  and  $R3$  beams (see Fig. 6.1) with orthogonal polarization and running at the frequency  $\omega_r$ , applies a force for time  $\tau$  to coherently excite the ion in the  $|1\rangle$  state but does not change the motional state of the ion in the  $|0\rangle$  state. The displacement in phase space was calibrated by measuring the total number of phonons in the radial mode as a function of the pulse duration of coherent excitation.

To prepare the Schrödinger cat state shown in Fig. 6.13(a, b), we follow the method similar to [99]. We start with the ion in the state  $(|0\rangle + |1\rangle)|0_r\rangle/\sqrt{2}$  by applying a  $\pi/2$  microwave pulse. We then apply the force that only displaces the ion in the internal state  $|1\rangle$ . After that we swap the internal states of the ions and apply the force with the opposite phase to produce the  $(|0\rangle|\alpha\rangle + |1\rangle|-\alpha\rangle)/\sqrt{2}$  state. Finally we apply a  $\pm\pi/2$  pulse to the internal state of the ion to prepare the state  $|0\rangle(|\alpha\rangle \pm |-\alpha\rangle)/2 + |1\rangle(|\alpha\rangle \mp |-\alpha\rangle)/2$  and measure the internal state of the ion using the standard fluorescence technique. If the ion is found in the  $|0\rangle$  internal state, its motional state is projected to the cat state  $(|\alpha\rangle \pm |-\alpha\rangle)/\sqrt{2}$  and it is unchanged because the ion scatters no photons. We can also control the relative phase of the displacement forces and phases of the microwave pulses to prepare the cat states with full control of their phases [45]. As an example, we prepare the Yurke-Stoler cat state [160]  $(|\alpha\rangle + |\alpha e^{i3\pi/2}\rangle)/\sqrt{2}$  and measure its Wigner function (see Fig. 6.13(c)).

The Fock states shown in Fig. 6.14 were generated by a sequence of  $\pi$  pulses on blue sideband of  $|0\rangle \rightarrow {}^2S_{1/2} |F=1, m=0\rangle$  transition, followed by a  $\pi$  pulse on the carrier transition. To generate the  $n$ -phonon Fock state  $|n\rangle$ , this sequence was repeated  $n$  times.

## 6.6 Conclusion and outlook

We have demonstrated strong nonlinear coupling between motional states of a two-ion crystal described by a Hamiltonian similar to degenerate optical parametric down conversion. When combined with nearly deterministic phonon preparation and a readout readily available in the ion trap, this coupling allows us to measure the parity of the ion motional state and determine the Wigner function of the ion motion. The ground state cooling of an optically inaccessible mode is also demonstrated.

The nonlinear coupling between the modes is another tool that can be added to the rich toolbox of the ion trapping techniques for quantum information processing, and the techniques demonstrated here can be useful for the preparation of nonclassical states of motion, or quantum gates.

# Bibliography

- [1] A. André, D. DeMille, J. M. Doyle, M. D. Lukin, S. E. Maxwell, P. Rabl, R. J. Schoelkopf, and P. Zoller. A coherent all-electrical interface between polar molecules and mesoscopic superconducting resonators. *Nature Physics*, 2(9):636–642, 2006. [2](#)
- [2] N. W. Ashcroft and N. D. Mermin. *Solid State Physics*. Brooks Cole, Pacific Grove, CA, USA, 1976. [7](#)
- [3] C. Balzer, A. Braun, T. Hannemann, C. Paape, M. Ettl, W. Neuhauser, and C. Wunderlich. Electrodynamically trapped yb+ ions for quantum information processing. *Physical Review A*, 73(4):041407, 2006. [17](#), [18](#)
- [4] J. Bergquist and W. Itano. Linear trap for high-accuracy spectroscopy. *Journal of Modern Optics*, 39(2):233–242, 1992. [12](#)
- [5] D. Berkeland and M. Boshier. Destabilization of dark states and optical spectroscopy in zeeman-degenerate atomic systems. *Physical Review A*, 65(3):033413, 2002. [25](#), [74](#)
- [6] D. Berkeland, J. Miller, J. Bergquist, W. Itano, and D. Wineland. Minimization of ion micromotion in a paul trap. *Journal of Applied Physics*, 83(10):5025–5033, 1998. [12](#), [29](#)

- [7] A. Bermudez, M. Bruderer, and M. B. Plenio. Controlling and measuring quantum transport of heat in trapped-ion crystals. *Phys. Rev. Lett.*, 111:040601, Jul 2013. [97](#)
- [8] P. Bertet, A. Auffeves, P. Maioli, S. Osnaghi, T. Meunier, M. Brune, J. M. Raimond, and S. Haroche. Direct measurement of the wigner function of a one-photon fock state in a cavity. *Phys. Rev. Lett.*, 89:200402, Oct 2002. [124](#)
- [9] E. D. Black. An introduction to pound–drever–hall laser frequency stabilization. *American Journal of Physics*, 69(1):79–87, 2001. [28](#)
- [10] R. Blatt and C. F. Roos. Quantum simulations with trapped ions. *Nature Physics*, 8(4):277–284, Apr. 2012. [97](#)
- [11] H. Blinchikoff et al. Realization of a filter with helical components. *Component Parts, IRE Transactions on*, 8(3):99–110, 1961. [14](#)
- [12] B. B. Blinov, D. Leibfried, C. Monroe, and D. J. Wineland. *Quantum Inf. Proc.*, 3:45, 2004. [3](#)
- [13] K. R. Brown, C. Ospelkaus, Y. Colombe, A. C. Wilson, D. Leibfried, and D. J. Wineland. Coupled quantized mechanical oscillators. *Nature*, 471:196–199, 2011. [7](#)
- [14] Z. L. Cai and J. P. Francois. *J. Mol. Spec*, 197:12, 1999. [51](#)
- [15] W. Campbell, J. Mizrahi, Q. Quraishi, C. Senko, D. Hayes, D. Hucul, D. Matsukevich, P. Maunz, and C. Monroe. Ultrafast gates for single atomic qubits. *Physical review letters*, 105(9):090502, 2010. [39](#)

## BIBLIOGRAPHY

---

- [16] L. D. Carr, D. DeMille, R. V. Krems, and J. Ye. *New J. Phys*, 11:055049, 2009. [2](#)
- [17] C. Chin, V. V. Flambaum, and M. G. Kozlov. *New J. Phys*, 11:055048, 2009. [2](#)
- [18] C. Chou, D. Hume, J. Koelemeij, D. Wineland, and T. Rosenband. Frequency comparison of two high-accuracy  $al^+$  optical clocks. *Physical Review Letters*, 104(7):070802, 2010. [2](#), [30](#)
- [19] C. R. Clark, J. E. Goeders, Y. K. Dodia, C. R. Viteri, and K. R. Brown. *Phys. Rev. A*, 81:043428, 2010. [3](#)
- [20] C. Cohen-Tannoudji and D. Guéry-Odelin. *Advances in atomic physics*. World Scientific, Singapore, 2011. [32](#), [36](#)
- [21] E. A. Cornell, R. M. Weisskoff, K. R. Boyce, and D. E. Pritchard. Mode coupling in a penning trap:  $\pi$  pulses and a classical avoided crossing. *Phys. Rev. A*, 41:312–315, Jan 1990. [117](#)
- [22] L. A. Correa, J. P. Palao, D. Alonso, and G. Adesso. Quantum-enhanced absorption refrigerators. *Sci. Rep.*, 4, Feb. 2014. [7](#)
- [23] H. Dehmelt et al. Radiofrequency spectroscopy of stored ions i: Storage. *Adv. At. Mol. Phys*, 3:53, 1967. [10](#)
- [24] H. G. Dehmelt. *Bull. Am. Phys. Soc.*, 20:60, 1975. [3](#)
- [25] S. Deleglise, I. Dotsenko, C. Sayrin, J. Bernu, M. Brune, J.-M. Raimond, and S. Haroche. Reconstruction of non-classical cavity field states with snapshots of their decoherence. *Nature*, 455(7212):510–514, Sept. 2008. [124](#)

- [26] D. DeMille, S. B. Kahn, D. Murkphree, D. A. Rakhmlow, and M. G. Kozlov. *Phys. Rev. Lett*, 100:023003, 2008. [2](#)
- [27] D. DeMille, S. Sainis, J. Sage, T. Bergeman, S. Kotochigova, and E. Tiesinga. *Phys. Rev. Lett*, 100:043202, 2008. [2](#)
- [28] L. Deslauriers. *Cooling and Heating of the Quantum Motion of Trapped Cd<sup>+</sup> Ions*. PhD thesis, University of Michigan. [12](#)
- [29] L. Deslauriers, P. Haljan, P. Lee, K. Brickman, B. Blinov, M. Madsen, and C. Monroe. Zero-point cooling and low heating of trapped cd+ 111 ions. *Physical Review A*, 70(4):043408, 2004. [30](#)
- [30] F. Diedrich, J. Bergquist, W. M. Itano, and D. Wineland. Laser cooling to the zero-point energy of motion. *Physical Review Letters*, 62(4):403, 1989. [30](#)
- [31] S. Ding, H. Loh, R. Hablutzel, M. Gao, G. Maslennikov, and D. Matsukevich. Microwave control of trapped-ion motion assisted by a running optical lattice. *Phys. Rev. Lett.*, 113:073002, Aug 2014. [6](#), [30](#), [117](#)
- [32] S. Ding and D. Matsukevich. *New J. Phys.*, 14:023028, 2012. [5](#)
- [33] S. Ding and D. N. Matsukevich. *Bull. Am. Phys. Soc*, 56(No 5, L1.00015), 2011. [45](#)
- [34] S. Ding and D. N. Matsukevich. *New J. Phys.*, 14:023028, 2012. [97](#)
- [35] R. Drever, J. L. Hall, F. Kowalski, J. Hough, G. Ford, A. Munley, and H. Ward. Laser phase and frequency stabilization using an optical resonator. *Applied Physics B*, 31(2):97–105, 1983. [28](#)

- [36] M. Enderlein, T. Huber, C. Schneider, and T. Schaetz. Single ions trapped in a one-dimensional optical lattice. *Phys. Rev. Lett.*, 109:233004, 2012. [6, 97](#)
- [37] B.-G. Englert, N. Sterpi, and H. Walther. Parity states in the one-atom maser. *Optics Communications*, 100(56):526 – 535, 1993. [124](#)
- [38] L. Förster, M. Karski, J.-M. Choi, A. Steffen, W. Alt, D. Meschede, A. Widera, E. Montano, J. H. Lee, W. Rakreungdet, and P. S. Jessen. *Phys. Rev. Lett.*, 103:233001, 2009. [6](#)
- [39] D. J. Gorman, P. Schindler, S. Selvarajan, N. Daniilidis, and H. Häffner. Two-mode coupling in a single-ion oscillator via parametric resonance. *Phys. Rev. A*, 89:062332, Jun 2014. [117](#)
- [40] M. Gottselig, M. Quack, J. Stohner, and M. Willeke. *Int. J. Mass Spec*, 233:373, 2004. [2](#)
- [41] M. Guggemos, D. Heinrich, O. Herrera-Sancho, R. Blatt, and C. Roos. Sympathetic cooling and detection of a hot trapped ion by a cold one. *arXiv preprint arXiv:1507.07761*, 2015. [75](#)
- [42] G. R. Guthohrlein, M. Keller, K. Hayasaka, W. Lange, and H. Walther. A single ion as a nanoscopic probe of an optical field. *Nature*, 414(6859):49–51, Nov. 2001. [6](#)
- [43] M. Harlander, R. Lechner, M. Brownnutt, R. Blatt, and W. Hansel. Trapped-ion antennae for the transmission of quantum information. *Nature*, 471:200–203, 2011. [7](#)

- [44] S. Haroche. Nobel lecture: Controlling photons in a box and exploring the quantum to classical boundary. *Reviews of Modern Physics*, 85(3):1083, 2013. [1](#)
- [45] S. Haroche and J. M. Raimond. *Exploring the quantum*. Oxford Univ. Press, 2006. [128](#)
- [46] Y. Hashimoto, L. Matsuoka, H. Osaki, Y. Fukushima, and S. Hasegawa. Trapping laser ablated ca+ ions in linear paul trap. *Japanese journal of applied physics*, 45(9R):7108, 2006. [18](#), [22](#)
- [47] D. Hayes, D. N. Matsukevich, P. Maunz, D. Hucul, Q. Quraishi, S. Olmschenk, W. Campbell, J. Mizrahi, C. Senko, and C. Monroe. Entanglement of atomic qubits using an optical frequency comb. *Phys. Rev. Lett.*, 104:140501, Apr 2010. [5](#), [30](#), [39](#), [45](#), [47](#), [60](#), [85](#)
- [48] D. L. Hayes. *Remote and Local Entanglement of Ions using Photons and Phonons*. PhD thesis, University of Maryland. [14](#), [15](#)
- [49] C. Hempel, B. P. Lanyon, P. Jurcevic, R. Gerritsma, R. Blatt, and C. F. Roos. *Nat. Photonics*, 7:630, 2013. [4](#)
- [50] R. Hendricks, D. Grant, P. F. Herskind, A. Dantan, and M. Drewsen. An all-optical ion-loading technique for scalable microtrap architectures. *Applied Physics B*, 88(4):507–513, 2007. [18](#), [19](#)
- [51] G. Herzberg. *Molecular Spectra and Molecular Structure: I. Spectra of Diatomic Molecules*. Van Nostrand Reinhold Company, 1950. [58](#)
- [52] J. Hojbjerg, A. K. Hansen, P. S. Skyt, P. F. Staunum, and M. Drewsen. *New J. Phys.*, 11:055026, 2009. [65](#)

## BIBLIOGRAPHY

---

- [53] C. K. Hong, Z. Y. Ou, and L. Mandel. *Phys. Rev. Lett*, 59:2044, 1987. [47](#)
- [54] E. R. Hudson. *Phys. Rev. A*, 79:032716, 2009. [4](#)
- [55] E. R. Hudson, H. J. Lewandowski, B. C. Sawyer, and J. Ye. *Phys. Rev. Lett*, 96:143004, 2006. [2](#)
- [56] J. J. Hudson, D. M. Kara, I. J. Smallman, B. E. Sauer, M. R. Tarbutt, and E. A. Hinds. *Nature*, 473:493, 2011. [2](#)
- [57] D. B. Hume. *Two-Species Ion Arrays for Quantum Logic Spectroscopy and Entanglement Generation*. PhD thesis, University of Colorado. [70](#), [72](#)
- [58] D. B. Hume, C. W. Chou, D. R. Leibbrandt, M. J. Thorpe, D. J. Wineland, and T. Rosenband. Trapped-ion state detection through coherent motion. *Phys. Rev. Lett.*, 107:243902, Dec 2011. [6](#)
- [59] W. M. Itano and D. J. Wineland. Laser cooling of ions stored in harmonic and penning traps. *Phys. Rev. A*, 25:35–54, Jan 1982. [24](#), [25](#)
- [60] J. D. Jackson and J. D. Jackson. *Classical electrodynamics*, volume 3. Wiley New York etc., 1999. [10](#)
- [61] D. F. V. James and J. Jerke. *Can. J. Phys.*, 85:625, 2007. [87](#)
- [62] M. Johanning, A. Braun, N. Timoney, V. Elman, W. Neuhauser, and C. Wunderlich. Individual addressing of trapped ions and coupling of motional and spin states using rf radiation. *Phys. Rev. Lett.*, 102:073004, Feb 2009. [6](#)

- [63] L. Karpa, A. Bylinskii, D. Gangloff, M. Cetina, and V. Vuletić. Suppression of ion transport due to long-lived subwavelength localization by an optical lattice. *Phys. Rev. Lett.*, 111:163002, Oct 2013. [6](#), [97](#)
- [64] A. Khromova, C. Piltz, B. Scharfenberger, T. F. Gloger, M. Johanning, A. F. Varón, and C. Wunderlich. *Phys. Rev. Lett.*, 108:220502, 2012. [6](#), [30](#), [97](#)
- [65] K. Kim, M.-S. Chang, R. Islam, S. Korenblit, L.-M. Duan, and C. Monroe. *Phys. Rev. Lett.*, 103:120502, 2009. [97](#)
- [66] N. Kjærgaard, L. Hornekær, A. Thommesen, Z. Videsen, and M. Drewsen. Isotope selective loading of an ion trap using resonance-enhanced two-photon ionization. *Applied Physics B*, 71(2):207–210, 2000. [17](#)
- [67] J. C. J. Koelemeij, B. Roth, A. Wicht, I. Ernsting, and S. Schiller. *Phys. Rev. Lett.*, 98:173002, 2007. [3](#)
- [68] P. G. Kwiat, K. Mattle, H. Weinfurter, A. Zeilinger, A. V. Sergienko, and Y. Shih. New high-intensity source of polarization-entangled photon pairs. *Phys. Rev. Lett.*, 75:4337–4341, Dec 1995. [7](#)
- [69] N. K. Langford, S. Ramelow, R. Prevedel, W. J. Munro, G. J. Milburn, and A. Zeilinger. Efficient quantum computing using coherent photon conversion. *Nature*, 478(7369):360–363, Oct. 2011. [7](#), [112](#)
- [70] C. Lazarou, M. Keller, and B. M. Garraway. *Phys. Rev. A*, 81:013418, 2010. [4](#)
- [71] F. Lecocq, I. M. Pop, I. Matei, E. Dumur, A. K. Feofanov, C. Naud, W. Guichard, and O. Buisson. Coherent frequency conversion in a su-

- perconducting artificial atom with two internal degrees of freedom. *Phys. Rev. Lett.*, 108:107001, Mar 2012. [7](#)
- [72] D. Leibfried. *New J. Phys.*, 14:023029, 2012. [97](#)
- [73] D. Leibfried, R. Blatt, C. Monroe, and D. Wineland. *Rev. Mod. Phys.*, 75:281, 2003. [2](#), [5](#), [11](#), [20](#), [23](#), [30](#), [31](#), [34](#), [37](#), [39](#)
- [74] D. Leibfried, D. M. Meekhof, B. E. King, C. Monroe, W. M. Itano, and D. J. Wineland. Experimental determination of the motional quantum state of a trapped atom. *Phys. Rev. Lett.*, 77:4281–4285, Nov 1996. [124](#)
- [75] D. R. Leibbrandt, R. J. Clark, J. Labaziewicz, P. Antohi, W. Bakr, K. R. Brown, and I. L. Chuang. Laser ablation loading of a surface-electrode ion trap. *Physical Review A*, 76(5):055403, 2007. [18](#), [22](#)
- [76] D. R. Leibbrandt, J. Labaziewicz, V. Vuletić, and I. L. Chuang. Cavity sideband cooling of a single trapped ion. *Physical review letters*, 103(10):103001, 2009. [30](#)
- [77] V. Letchumanan, G. Wilpers, M. Brownnutt, P. Gill, and A. Sinclair. Zero-point cooling and heating-rate measurements of a single  $\text{Sr}^{+88}$  ion. *Physical Review A*, 75(6):063425, 2007. [30](#)
- [78] P. D. Lett, W. D. Phillips, S. Rolston, C. E. Tanner, R. Watts, and C. Westbrook. Optical molasses. *JOSA B*, 6(11):2084–2107, 1989. [24](#)
- [79] B. L. Lev, A. Vukics, E. R. Hudson, B. C. Sawyer, P. Domokos, H. Ritsch, and J. Ye. Prospects for the cavity-assisted laser cooling of molecules. *Physical Review A*, 77(2):023402, 2008. [4](#)

## BIBLIOGRAPHY

---

- [80] A. Levy and R. Kosloff. Quantum absorption refrigerator. *Phys. Rev. Lett.*, 108:070604, Feb 2012. [7](#)
- [81] X. Li, T. A. Corcovilos, Y. Wang, and D. S. Weiss. *Phys. Rev. Lett.*, 108:103001, 2012. [6](#)
- [82] C.-Y. Lien, C. M. Seck, Y.-W. Lin, J. H. Nguyen, D. A. Tabor, and B. C. Odom. Broadband optical cooling of molecular rotors from room temperature to the ground state. *Nature communications*, 5, 2014. [4](#), [53](#)
- [83] C.-Y. Lien, S. R. Williams, and B. Odom. Optical pulse-shaping for internal cooling of molecules. *Physical Chemistry Chemical Physics*, 13(42):18825–18829, 2011. [4](#), [51](#)
- [84] Y. Lin, J. Gaebler, T. Tan, R. Bowler, J. Jost, D. Leibfried, and D. Wineland. Sympathetic electromagnetically-induced-transparency laser cooling of motional modes in an ion chain. *Physical review letters*, 110(15):153002, 2013. [30](#)
- [85] Y.-W. Lin, S. Williams, and B. C. Odom. *Phys. Rev. A*, 87:011402(R), 2013. [3](#)
- [86] R. B. Linnet, I. D. Leroux, M. Marciante, A. Dantan, and M. Drewsen. Pinning an ion with an intracavity optical lattice. *Phys. Rev. Lett.*, 109:233005, 2012. [6](#), [97](#)
- [87] H.-Y. Lo, D. Kienzler, L. de Clercq, M. Marinelli, V. Negnevitsky, B. C. Keitch, and J. P. Home. Spin-motion entanglement and state diagnosis with squeezed oscillator wavepackets. *Nature*, 521(7552):336–339, 2015. [5](#)

## BIBLIOGRAPHY

---

- [88] H. Loh, S. Ding, R. Hablutzel, G. Maslennikov, and D. Matsukevich. Zeeman-splitting-assisted quantum-logic spectroscopy of trapped ions. *Physical Review A*, 90(6):061402, 2014. [5](#)
- [89] W. H. Louisell. *Coupled Mode and Parametric Electronics*. John Wiley, New York, 1960. [7](#)
- [90] L. G. Lutterbach and L. Davidovich. Method for direct measurement of the wigner function in cavity qed and ion traps. *Phys. Rev. Lett.*, 78:2547–2550, Mar 1997. [124](#)
- [91] W. Macalpine and R. Schildknecht. Coaxial resonators with helical inner conductor. *Proceedings of the IRE*, 47(12):2099–2105, 1959. [14](#)
- [92] L. Mandel and E. Wolf. *Optical Coherence and Quantum Optics*. Cambridge University Press, Cambridge, U.K., 1995. [7](#), [99](#)
- [93] C. Marquet, F. Schmidt-Kaler, and D. James. Phononphonon interactions due to non-linear effects in a linear ion trap. *Applied Physics B*, 76(3):199–208, 2003. [7](#), [99](#)
- [94] J. J. McLoughlin, A. H. Nizamani, J. D. Siverns, R. C. Sterling, M. D. Hughes, B. Lekitsch, B. Stein, S. Weidt, and W. K. Hensinger. Versatile ytterbium ion trap experiment for operation of scalable ion-trap chips with motional heating and transition-frequency measurements. *Physical Review A*, 83(1):013406, 2011. [26](#)
- [95] D. M. Meekhof, C. Monroe, B. E. King, W. M. Itano, and D. J. Wineland. Generation of nonclassical motional states of a trapped atom. *Phys. Rev. Lett.*, 76:1796–1799, Mar 1996. [5](#), [30](#), [90](#), [117](#), [122](#)

- [96] F. Mintert and C. Wunderlich. *Phys. Rev. Lett.*, 87:257904, 2001. [6](#)
- [97] J. Mizrahi, B. Neyenhuis, K. Johnson, W. Campbell, C. Senko, D. Hayes, and C. Monroe. Quantum control of qubits and atomic motion using ultra-fast laser pulses. *Applied Physics B*, 114(1-2):45–61, 2014. [39](#)
- [98] C. Monroe, D. M. Meekhof, B. E. King, S. R. Jefferts, W. M. Itano, D. J. Wineland, and P. Gould. *Phys. Rev. Lett.*, 75:4011, 1995. [30](#), [37](#), [46](#)
- [99] C. Monroe, D. M. Meekhof, B. E. King, and D. J. Wineland. A schrödinger cat superposition state of an atom. *Science*, 272(5265):1131–1136, 1996. [128](#)
- [100] G. Morigi, J. Eschner, and C. H. Keitel. Ground state laser cooling using electromagnetically induced transparency. *Physical review letters*, 85(21):4458, 2000. [30](#)
- [101] G. Morigi, P. W. H. Pinsky, M. Kowalewski, and R. de Vivie-Riedle. *Phys. Rev. Lett.*, 99:073001, 2007. [4](#)
- [102] J. Mur-Petit, J. J. García-Ripoll, J. Pérez-Ríos, J. Campos-Martínez, M. I. Hernández, and S. Willitsch. *Phys. Rev. A*, 85:022308, 2012. [4](#)
- [103] W. Neuhauser, M. Hohenstatt, P. Toschek, and H. Dehmelt. Optical-sideband cooling of visible atom cloud confined in parabolic well. *Phys. Rev. Lett.*, 41:233–236, Jul 1978. [1](#), [22](#)
- [104] J. H. V. Nguyen and B. Odom. *Phys. Rev. A*, 83:053404, 2011. [4](#), [51](#)
- [105] K.-K. Ni, H. Loh, M. Grau, K. Cossel, J. Ye, and E. A. Cornell. *J. Mol Spectrosc.*, 300:12, 2014. [65](#)

## BIBLIOGRAPHY

---

- [106] X. Nie, C. F. Roos, and D. James. Theory of cross phase modulation for the vibrational modes of trapped ions. *Physics Letters A*, 373(4):422 – 425, 2009. [7](#), [99](#)
- [107] A. Noguchi, Y. Shikano, K. Toyoda, and S. Urabe. Aharonov–bohm effect in the tunnelling of a quantum rotor in a linear paul trap. *Nature communications*, 5, 2014. [103](#), [111](#)
- [108] S. Olmschenk, K. C. Younge, D. L. Moehring, D. N. Matsukevich, P. Maunz, and C. Monroe. *Phys. Rev. A*, 76:052314, 2007. [17](#), [28](#), [59](#), [60](#), [61](#), [63](#)
- [109] S. M. Olmschenk. *Quantum Teleportation Between Distant Matter Qubits*. PhD thesis, University of Michigan. [14](#), [15](#)
- [110] C. Ospelkaus, C. E. Langer, J. M. Amini, K. R. Brown, D. Leibfried, and D. J. Wineland. *Phys. Rev. Lett.*, 101:090502, 2008. [6](#)
- [111] C. Ospelkaus, U. Warring, Y. Colombe, K. R. Brown, J. M. Amini, D. Leibfried, and D. J. Wineland. *Nature*, 476:181, 2011. [6](#), [30](#)
- [112] W. Paul. Electromagnetic traps for charged and neutral particles. *Reviews of modern physics*, 62(3):531, 1990. [1](#), [10](#), [20](#)
- [113] E. Peik, J. Abel, T. Becker, J. Von Zanthier, and H. Walther. Sideband cooling of ions in radio-frequency traps. *Physical Review A*, 60(1):439, 1999. [30](#)
- [114] G. Poulsen and M. Drewsen. Adiabatic cooling of a single trapped ion. *arXiv preprint arXiv:1210.4309*, 2012. [103](#), [111](#)

- [115] T. Pruttivarasin, M. Ramm, I. Talukdar, A. Kreuter, and H. Häffner. Trapped ions in optical lattices for probing oscillator chain models. *New J. Phys.*, 13:075012, 2011. [97](#)
- [116] W. G. Rellergert, S. T. Sullivan, S. J. Schowalter, S. Kotochigova, K. Chen, and E. R. Hudson. Evidence for sympathetic vibrational cooling of translationally cold molecules. *Nature*, 495(7442):490–494, 2013. [4](#), [65](#)
- [117] C. Roos, D. Leibfried, A. Mundt, F. Schmidt-Kaler, J. Eschner, and R. Blatt. Experimental demonstration of ground state laser cooling with electromagnetically induced transparency. *Physical review letters*, 85(26):5547, 2000. [30](#)
- [118] C. Roos, T. Zeiger, H. Rohde, H. Nägerl, J. Eschner, D. Leibfried, F. Schmidt-Kaler, and R. Blatt. Quantum state engineering on an optical transition and decoherence in a paul trap. *Physical Review Letters*, 83(23):4713, 1999. [30](#)
- [119] C. F. Roos, T. Monz, K. Kim, M. Riebe, H. Häffner, D. F. V. James, and R. Blatt. Nonlinear coupling of continuous variables at the single quantum level. *Phys. Rev. A*, 77:040302, Apr 2008. [7](#), [105](#)
- [120] T. Rosenband, D. Hume, P. Schmidt, C. Chou, A. Bruschi, L. Lorini, W. Oskay, R. Drullinger, T. Fortier, J. Stalnaker, et al. Frequency ratio of  $al^+$  and  $hg^+$  single-ion optical clocks; metrology at the 17th decimal place. *Science*, 319(5871):1808–1812, 2008. [45](#), [48](#), [54](#)
- [121] B. Roth, J. C. J. Koelemeij, H. Daerr, and S. Schiller. *Phys. Rev. A*, 74:040501, 2006. [65](#)

## BIBLIOGRAPHY

---

- [122] A. Royer. Wigner function as the expectation value of a parity operator. *Phys. Rev. A*, 15:449–450, Feb 1977. [124](#)
- [123] B. E. Saleh, M. C. Teich, and B. E. Saleh. *Fundamentals of photonics*, volume 22. Wiley New York, 2007. [18](#)
- [124] S. Schlemmer, T. Kuhn, E. Lescop, and D. Gerlich. *Int. J. Mass. Spectrosc.*, 185:589, 1999. [65](#)
- [125] P. Schmidt, T. Rosenband, J. Koelemeij, D. Hume, W. Itano, J. Bergquist, and D. Wineland. Spectroscopy of atomic and molecular ions using quantum logic. *Non-Neutral Plasma Physics VI*, 862:305–312, 2006. [3](#), [4](#), [45](#)
- [126] P. O. Schmidt, T. Rosenband, C. Langer, W. M. Itano, J. C. Bergquist, and D. J. Wineland. *Science*, 309:749, 2005. [3](#), [45](#), [48](#), [54](#), [55](#)
- [127] T. Schneider, B. Roth, H. Duncker, I. Ernsting, and S. Schiller. *Nature Physics*, 6:275, 2010. [4](#), [53](#)
- [128] T. J. Scholl, R. Cameron, S. D. Rosner, and R. A. Holt. *Can. J. Phys.*, 73:101, 1995. [59](#)
- [129] E. Schrödinger. Are there quantum jumps? part i. *The British Journal for the Philosophy of science*, 3(10):109–123, 1952. [1](#)
- [130] C. M. Seck, E. G. Hohenstein, C.-Y. Lien, P. R. Stollenwerk, and B. C. Odom. *J. Mol Spectrosc.*, 300:108, 2014. [65](#)
- [131] D. M. Segal and C. Wunderlich. Cooling techniques for trapped ions, 2014. [37](#)

## BIBLIOGRAPHY

---

- [132] E. A. Shapiro, A. Pe'er, J. Ye, and M. Shapiro. *Phys. Rev. Lett*, 101:023601, 2008. [45](#)
- [133] A. Shelkownikov, R. J. Butcher, C. Chardonnet, and A. Amy-Klein. *Phys. Rev. Lett*, 100:150801, 2008. [2](#)
- [134] M. Shi, P. F. Herskind, M. Drewsen, and I. L. Chuang. *New J. Phys.*, 15:113019, 2013. [4](#), [97](#)
- [135] W. M. Siebert. *Circuits, signals, and systems*, volume 2. MIT press, 1986. [20](#)
- [136] M. Singh, H. Bredohl, R. Fr, and I. Dubois. *J. Phys. B*, 6:2656, 1973. [51](#)
- [137] P. F. Staannum, K. Hojbjerg, P. S. Skyt, A. K. Hansen, and M. Drewsen. *Nature Physics*, 6:271, 2010. [4](#), [53](#)
- [138] M. C. Stowe, M. J. Thorpe, A. Pe'er, J. Ye, J. E. Stalnaker, V. Gerginov, and S. A. Diddams. *Advances in Atomic, Molecular and Optical Physics*, 55:1, 2008. [48](#)
- [139] R. P. Stutz and E. A. Cornell. *Bull. Am. Soc. Phys*, 89:76, 2004. [2](#)
- [140] L. Sun, A. Petrenko, Z. Leghtas, B. Vlastakis, G. Kirchmair, K. M. Sliwa, A. Narla, M. Hatridge, S. Shankar, J. Blumoff, L. Frunzio, M. Mirrahimi, M. H. Devoret, and R. J. Schoelkopf. Tracking photon jumps with repeated quantum non-demolition parity measurements. *Nature*, 511(7510):444–448, July 2014. [124](#)
- [141] X. Tong, A. H. Winney, and S. Willitsch. *Phys. Rev. Lett*, 105:143001, 2010. [4](#), [65](#)

## BIBLIOGRAPHY

---

- [142] D. Van Heijnsbergen, T. D. Jaeger, G. von Helden, G. Meijer, and M. A. Duncan. *Chem. Phys. Lett*, 364:345, 2002. [3](#)
- [143] M. Viteau, A. Chotia, M. Allegrini, N. Bouloufa, O. Dulieu, D. Comparat, and P. Pillet. Optical pumping and vibrational cooling of molecules. *Science*, 321(5886):232–234, 2008. [4](#), [51](#)
- [144] I. S. Vogelius, L. B. Madsen, and M. Drewsen. *J. Phys. B: At. Mol. Opt. Phys*, 39:S1267, 2006. [4](#)
- [145] I. S. Vogelius, L. B. Madsen, and M. Drewsen. *J. Phys. B: At. Mol. Opt. Phys. B*, 39:S1259, 2006. [4](#)
- [146] V. Vuletić and S. Chu. Laser cooling of atoms, ions, or molecules by coherent scattering. *Physical Review Letters*, 84(17):3787, 2000. [30](#), [37](#)
- [147] Y. Wan, F. Gebert, J. B. Wübbena, N. Scharnhorst, S. Amairi, I. D. Leroux, B. Hemmerling, N. Lörch, K. Hammerer, and P. O. Schmidt. *Nat. Commun.*, 5:3096, 2014. [3](#), [64](#)
- [148] S. Weidt, J. Randall, S. C. Webster, E. D. Standing, A. Rodriguez, A. E. Webb, B. Lekitsch, and W. K. Hensinger. Ground-state cooling of a trapped ion using long-wavelength radiation. *Phys. Rev. Lett.*, 115:013002, Jun 2015. [30](#)
- [149] E. Wigner. On the quantum correction for thermodynamic equilibrium. *Phys. Rev.*, 40:749–759, Jun 1932. [124](#)
- [150] S. Willitsch, M. T. Bell, A. D. Gingell, and T. P. Softley. *Phys. Chem. Chem. Phys*, 10:7200, 2008. [2](#)

- [151] D. Wineland, C. Monroe, W. Itano, B. King, D. Leibfried, D. Meekhof, C. Myatt, and C. Wood. Experimental primer on the trapped ion quantum computer. *spectroscopy*, 7:8, 1998. [10](#)
- [152] D. J. Wineland. Nobel lecture: Superposition, entanglement, and raising schrödingers cat. *Reviews of Modern Physics*, 85(3):1103, 2013. [1](#)
- [153] D. J. Wineland, M. Barrett, J. Britton, J. Chiaverini, B. DeMarco, W. Itano, B. Jelenković, C. Langer, D. Leibfried, V. Meyer, et al. Quantum information processing with trapped ions. *Philosophical Transactions of the Royal Society of London A: Mathematical, Physical and Engineering Sciences*, 361(1808):1349–1361, 2003. [41](#)
- [154] D. J. Wineland, R. E. Drullinger, and F. L. Walls. Radiation-pressure cooling of bound resonant absorbers. *Phys. Rev. Lett.*, 40:1639–1642, Jun 1978. [1](#), [22](#)
- [155] D. J. Wineland and W. M. Itano. Laser cooling of atoms. *Physical Review A*, 20(4):1521, 1979. [23](#), [32](#), [36](#), [37](#)
- [156] D. J. Wineland and W. M. Itano. Laser cooling. *Physics Today*, 40:34–40, 1987. [24](#), [32](#), [36](#)
- [157] D. J. Wineland, C. Monroe, W. M. Itano, D. Leibfried, B. E. King, and D. M. Meekhof. *J. Res. Natl. Inst. Stand. Technol.*, 103:259, 1998. [47](#), [88](#)
- [158] L.-A. Wu, H. J. Kimble, J. L. Hall, and H. Wu. Generation of squeezed states by parametric down conversion. *Phys. Rev. Lett.*, 57:2520–2523, Nov 1986. [7](#)

## BIBLIOGRAPHY

---

- [159] J. B. Wübbena, S. Amairi, O. Mandel, and P. O. Schmidt. Sympathetic cooling of mixed-species two-ion crystals for precision spectroscopy. *Physical Review A*, 85(4):043412, 2012. [24](#), [25](#), [70](#), [72](#)
- [160] B. Yurke and D. Stoler. Generating quantum mechanical superpositions of macroscopically distinguishable states via amplitude dispersion. *Physical review letters*, 57(1):13, 1986. [128](#)
- [161] T. Zelevinsky, S. Kotochigova, and J. Ye. *Phys. Rev. Lett*, 100:043201, 2008. [2](#)
- [162] K. Zimmermann, M. Okhapkin, O. Herrera-Sancho, and E. Peik. Laser ablation loading of a radiofrequency ion trap. *Applied Physics B*, 107(4):883–889, 2012. [18](#), [22](#)